



Co-Simulation of the Lumbar Intervertebral
Discs through Finite Element Method and
Multibody System Dynamics

Ivo Miguel Monteiro da Silva

Universidade do Minho
Escola de Engenharia





Universidade do Minho
Escola de Engenharia

Ivo Miguel Monteiro da Silva

Co-Simulation of the Lumbar Intervertebral
Discs through Finite Element Method and
Multibody System Dynamics

Dissertação de Mestrado
Ciclo de Estudos Integrados Conducentes ao
Grau de Mestre em Engenharia Biomédica

Trabalho efetuado sob a orientação do
Professor Doutor José Carlos Pimenta Claro
Doutor André Paulo Galvão de Castro

Declaração

Nome: Ivo Miguel Monteiro da Silva

Endereço eletrónico: ivommsilva@hotmail.com

Telefone: 00351 914 131 291

Número de Identificação: 14011887

Título da Dissertação: Co-Simulation of the Lumbar Intervertebral Discs through Finite Element Method and Multibody System Dynamics

Ano de Conclusão: 2014

Orientador: Professor José Carlos Pimenta Claro

Designação do Mestrado: Ciclo de Estudos Integrados Conducentes ao Grau de Mestre em Engenharia Biomédica

Área de Especialização: Biomateriais, Reabilitação e Biomecânica

Escola: Engenharia

Departamento: Engenharia Mecânica

DE ACORDO COM A LEGISLAÇÃO EM VIGOR, NÃO É PERMITIDA A REPRODUÇÃO DE QUALQUER PARTE DESTA TESE/TRABALHO.

Guimarães, ____/____/____

Assinatura: _____

Acknowledgments

This section is addressed to acknowledge all those who gave their contribute to this work and were always available for me.

Firstly, I would like to acknowledge my supervisors, Professor José Carlos Pimenta Claro and Doctor André Castro for their guidance and support, and for being available to help during the development of the present work.

I would also like to gratefully acknowledge the support of the European Project: “NP Mimetic – Biomimetic Nano-Fiber Based Nucleus Pulposus Regeneration for the Treatment of Degenerative Disc Disease”, founded by the European Commission under FP7 (grant EU246351/CT2M-MSc10).

My acknowledgment to all my colleagues of CT2M (University of Minho) for the excellent team environment provided and for always being available to help.

A special thanks to my family and friends for encouraging and motivating me throughout this journey.

Finally, I want to thank Patricia for her unconditional support, patience and affection.

Abstract

Co-Simulation of the Lumbar Intervertebral Discs through Finite Element Method and Multibody Systems Dynamics

Degenerative disc disease is the most common cause of low back pain, affecting about 70-85% of the general population at some time in life. This evidence became the motivation for this work, whose purpose is to analyze the geometric sensibility of a finite element model of the lumbar intervertebral disc, and to optimize a three-dimensional multibody lumbar spine model.

Throughout the years, the development of mathematical spine models using finite element and multibody system formulations have evolved greatly. Nowadays, human spine models are able to reproduce with accuracy the biomechanical response of the different anatomical features of the spine.

At an initial stage, a lumbar partial motion segment model and respective finite element formulation are briefly described. The model is composed by two partial vertebrae connected by an intervertebral disc. A geometric sensibility analysis of the model is performed by varying its wedge angle and average height, and simulating the models under different types of incremental loads, using a home-developed finite element solver. From this analysis, different mechanical aspects of the intervertebral disc's behavior are obtained, such as volume and pressure variations of both *nucleus pulposus* and *annulus fibrosus*, quantity and grade of annulus' fibers stretching, and range of angular motion. The respective results prove that both wedge angle and average height variations have significant influence on the intervertebral discs' behavior under loading.

Thereafter, a general concept of multibody system is defined, and a description of a multibody lumbar spine model is presented. The model is composed by six rigid bodies, representing the lumbar vertebrae and the sacrum, and fifty spring/damper sets, modeling the intervertebral discs and lumbar ligaments. Based on the angles of the different lumbar levels, the model is optimized by implementing the results of the previous geometric sensibility analysis. The model is validated using experimental data found in the literature, revealing identical behavior during lateral flexion and axial rotation. Subsequently, the application of the model is performed by applying different

types of loads and analyze their distribution along the lumbar spine levels. The results indicate that the last two lumbar levels are more susceptible to mechanical stresses, being the tendency to degeneration of these discs probably related to this fact.

Resumo

Co-Simulação dos Discos Intervertebrais Lombares através do Método de Elementos Finitos e da Dinâmica de Sistemas Multi-corpo

A doença degenerativa dos discos intervertebrais é a causa mais comum de dor lombar, afetando cerca de 70-85% de toda a população em alguma altura durante a vida. Esta evidência tornou-se a motivação para a realização deste trabalho, cujo objetivo é analisar a sensibilidade geométrica de um modelo de elementos finitos de um disco intervertebral lombar, e otimizar um modelo multi-corpo tridimensional da coluna lombar.

Ao longo dos anos, o desenvolvimento de modelos matemáticos da coluna usando formulações de elementos finitos e sistemas multi-corpo tem evoluído bastante. Atualmente, os modelos da coluna humana são capazes de reproduzir com precisão as respostas biomecânicas dos diferentes componentes anatómicos da coluna.

Numa fase inicial, é sucintamente descrito um modelo de um segmento móvel lombar parcial e a respetiva formulação de elementos finitos. O modelo é composto por duas vértebras parciais conectadas por um disco intervertebral. Uma análise da sensibilidade geométrica do modelo é realizada através da variação do seu ângulo e da sua altura média, e, recorrendo a um programa de elementos finitos desenvolvido internamente, os modelos foram simulados com a aplicação de diferentes tipos de cargas. Desta análise, os diferentes aspetos mecânicos do comportamento do disco são obtidos, como a variação de volume e pressão do anel fibroso e do núcleo pulposo, bem como a quantidade e grau de alongamento das fibras do anel, e a amplitude de movimento. Os respetivos resultados provam que a variação do ângulo e da altura média têm influência considerável no comportamento dos discos intervertebrais quando sujeitos a cargas.

Após isso, é definido o conceito geral de sistema multi-corpo, e é apresentada uma descrição do modelo multi-corpo da coluna lombar. O modelo é composto por seis corpos rígidos, representando as vértebras lombares e o sacro, e cinquenta conjuntos mola/amortecedor, modelando os discos intervertebrais e os ligamentos lombares. Com base nos ângulos dos diferentes níveis lombares, o modelo é otimizado através da implementação dos resultados da análise da sensibilidade geométrica, obtidos anteriormente. O modelo é validado usando

resultados experimentais encontrados na literatura, revelando comportamento idêntico na flexão lateral e rotação axial. Subsequentemente, a aplicação do modelo é realizada através da aplicação de diferentes tipos de cargas e analisando a sua distribuição ao longo dos níveis da coluna lombar. Os resultados indicam que os últimos níveis lombares são mais suscetíveis a esforços mecânicos, podendo estar a tendência para a degeneração destes discos relacionada com este fato.

Index

Acknowledgments.....	iii
Abstract.....	v
Resumo.....	vii
List of Abbreviations and Acronyms.....	xiii
List of Figures.....	xv
List of Tables.....	xxi
CHAPTER 1 - Introduction.....	1
1.1. Motivation and Scope.....	1
1.2. Literature Review.....	2
1.2.1. Multibody Systems Dynamics approaches.....	3
1.2.2. Finite Element Method approaches.....	8
1.3. Objectives.....	18
1.4. Structure of the thesis.....	18
CHAPTER 2 - Spine characterization.....	19
2.1 Spinal Anatomy.....	19
2.1.1. The vertebrae.....	20
2.1.1.1. Lumbar vertebrae.....	22
2.1.1.2. Sacrum.....	23
2.1.1.3. Coccyx.....	23
2.1.2. Facet joints.....	23
2.1.3. Intervertebral disc.....	24
2.1.3.1. Nucleus Pulposus.....	25
2.1.3.2. Annulus Fibrosus.....	25
2.1.3.3. Cartilaginous Endplate.....	25

2.1.4. Ligaments	26
2.1.4.1. Anterior Longitudinal Ligament.....	27
2.1.4.2. Posterior Longitudinal Ligament	27
2.1.4.3. Ligamentum Flavum	28
2.1.4.4. Interspinous Ligament	28
2.1.4.5. Supraspinous Ligament	28
2.1.4.6. Intertransverse Ligament	28
2.1.4.7. Capsular Ligament.....	28
2.2 Spinal movements.....	29
2.3 Spinal disorders	30
2.3.1. Disc Degenerative Disease	32
2.3.2. Solutions for Degenerated Discs.....	33
CHAPTER 3 - Finite Element Modeling.....	35
3.1. Mechanical Modeling.....	35
3.2. Finite Element Model	35
3.3. Geometric Sensibility Study of the FE model.....	37
3.3.1. Wedge Angle Variation	37
3.3.2. Average Height Variation	38
3.3.3. Simulation Settings	39
3.3.4. Simulation Results	41
3.3.4.1. Wedge Angle Variation	41
3.3.4.1. Average Height Variation	52
CHAPTER 4 - Multibody Dynamic Modeling	63
4.1. Multibody System Formulation	63
4.2. 3D Multibody Spine Model	64

4.2.1. Description of the model	65
4.2.1.1. Intervertebral Discs modeling	67
4.2.2. Comparison of FEM and MBS results	72
4.2.3. Validation of the model	78
4.2.4. Application of the model.....	89
CHAPTER 5 - Conclusions.....	95
APPENDIX A – Range of motion of the lumbar vertebrae	105

List of Abbreviations and Acronyms

3D: Three-Dimensional

AF: Annulus Fibrosus

ALL: Anterior Longitudinal Ligament

AR: Axial Rotation

CEP: Cartilaginous Endplate

Ex-Fx: Extension-flexion

FE: Finite Element

FEM: Finite Element Method

ISL: Interspinous Ligament

IVD: Intervertebral Disc

LF: Ligamentum Flavum

LFx: Lateral Flexion

PLL: Posterior Longitudinal Ligament

MBS: Multibody System

MS: Motion segment

NP: Nucleus Pulposus

Rx: Reaction force on X-axis

Ry: Reaction force on Y-axis

Rz: Reaction force on Z-axis

SSL: Supraspinous Ligament

VB: Vertebral Body

VEP: Vertebral Endplate

List of Figures

Figure 1.1 - Modeling components from the work of Broman <i>et al.</i> (Adapted from [23]).	9
Figure 1.2 - Schematic representation of the models by Stokes <i>et al.</i> : (a) Stiffness model; (b) Static model (Adapted from [24]).	9
Figure 1.3 - Partial representation of De Jager's model (Adapted from [25]).	10
Figure 1.4 - Human spine MBS model developed by Waters <i>et al.</i> (Adapted from [26]).	11
Figure 1.5 - Three-dimensional MBS model of the human spine developed by Ishikawa <i>et al.</i> : (a) General view; (b) Detailed representation of the IVDs and ligaments (Adapted from [27]).	11
Figure 1.6 - Lumbar spine MBS model developed by Esat (Adapted from [17]).	12
Figure 1.7 - Sequential representation of the lateral impact of Ferreira's model: (a) lateral view; (b) frontal view (Adapted from [28]).	12
Figure 1.8 - Three-dimensional model of the lumbar spine developed by Juchem (Adapted from [29]).	13
Figure 1.9 - Hybrid model developed by Monteiro: (a) three-dimensional MS; (b) FE mesh of the fixation plate and screws (Adapted from [30]).	14
Figure 1.10 - Cristophy's three-dimensional musculoskeletal model with 238 muscles, 13 rigid bodies and 5 intervertebral joints: (a) neutral posture; (b) 50° flexion (Adapted from [31]).	14
Figure 1.11 - Representation of the lumbosacral spine model developed by Abouhossein (Adapted from [32]).	15
Figure 1.12 - Lumbar spine MBS model of Galibarov <i>et al.</i> highlighting: (a) the lumbar ligaments (red segments); (b) the IVDs (red spherical joints) (Adapter from [33]).	16
Figure 1.13 - Lumbar MBS model developed by Han <i>et al.</i> with emphasis to (a) muscle segments, and (b) ligaments (Adapted from [34]).	16
Figure 1.14 - Musculoskeletal spine model developed by Huynh <i>et al.</i> : (a) frontal view; (b) lateral view (Adapted from [35]).	17
Figure 1.15 - FE mesh of the L2-L3 MS model of Wang <i>et al.</i> highlighting its different structures (Adapter from [53]).	4
Figure 1.16 - FE model a lumbar IVD proposed by Ferguson <i>et al.</i> The different colors of the three-dimensional mesh represent the distinct components of the IVD (Adapted from [57]).	5
Figure 1.17 - FE model of a L4-L5 MS proposed by Natarajan <i>et al.</i> (Adapted from [58]).	5

Figure 1.18 - FE mesh of one quarter of an IVD proposed by Schroeder <i>et al.</i> (Adapted from [59]).....	6
Figure 1.19 - Three-dimensional FE mesh of a lumbar IVD developed by Strange <i>et al.</i> (Adapted from [60]).	6
Figure 1.20 - Huang's FE mesh of (a) the lumbar MS, (b) a healthy disc, (c) a mildly herniated disc, (d) a severely herniated disc, (e) a mildly herniated disc with NP removal, and (f) a severely herniated disc with NP removal. (Adapted from [61]).....	7
Figure 1.21 - Anterior-posterior cut of the FE mesh of a lumbar MS developed by Castro (Adapted from [62]).	7
Figure 2.1 - Left lateral and posterior view of the human spine's anatomy, with a lumbar MS highlighted (Adapted from [64]).	20
Figure 2.2 - Superior, posterior and lateral view of a typical vertebra (Adapted from [16]).	21
Figure 2.3 - Vertebra divided by functional parts: (a) Vertebral body, (b) Pedicle, (c) Posterior elements (Adapted from [68]).	22
Figure 2.4 - IVD's anatomy: (a) a MS's structural organization; (b) IVD's detailed structures and dimensions (Adapted from [69]).....	24
Figure 2.5 - Components of the IVD (Adapted from [72]).	26
Figure 2.6 - Hierarchical organization of the ligament, components and respective dimensions (Adapted from [73]).	26
Figure 2.7 - Ligaments of a MS (Adapted from [28]).	27
Figure 2.8 - Spinal movements and its anatomical planes and axes. (a) The four principal movements of the human spine: lateral flexion, rotation, flexion and extension; (b) Principal axes and planes of the human body (Adapted from [75]).....	29
Figure 2.9 - Schematic representation of the 6 DOF of a MS (Adapted from [76]).....	30
Figure 2.10 - Macroscopic disc changes due to DDD: (a) grade I; (b) grade II; (c) grade III; (d) grade IV; (e) grade V (Adapted from [77]).	31
Figure 2.11 - Compression loading of (a) a normal non-degenerated and (b) degenerated disc. (c) Outer annulus layers have a large tension stress along the fibers and also in the tangential peripheral direction. The inner annulus fibers have stresses of smaller magnitude. (d) Annulus fibers show outer layers which are subjected to increased amount of tensile stress. The inner fibers have a high compressive stress (Adapted from [70]).	32

Figure 3.1 - FE mesh: (a) a perspective view; (b) sagittal cut of the FE mesh evidencing the different structures.	36
Figure 3.2 - Sagittal cut of the FE model with: (a) -2°; (b) 0°; (c) 5°; (d) 7°; (e) 11°; and (f) 20°.	38
Figure 3.3 - Loading profile of the applied moment.	40
Figure 3.4 - Loading profile of the whole simulation.	40
Figure 3.5 - NP pressure variation during extension.	41
Figure 3.6 - NP pressure variation during flexion.	42
Figure 3.7 - AF pressure variation during extension.	43
Figure 3.8 - AF pressure variation during flexion.	43
Figure 3.9 - NP and AF volume variation during extension.	44
Figure 3.10 - NP and AF volume variation during flexion.	44
Figure 3.11 - AF fiber stretch during extension: (a) at 10s - end of pre-conditioning period; (b) 12s - end of loading period.	45
Figure 3.12 - AF fiber stretch during flexion: (a) at 10s - end of pre-conditioning period; (b) 12s - end of loading period.	45
Figure 3.13 - Angular range of extension-flexion movement.	46
Figure 3.14 - NP pressure variation during lateral flexion.	46
Figure 3.15 - AF pressure variation during lateral flexion.	47
Figure 3.16 - NP and AF volume variation during lateral flexion.	47
Figure 3.17 - AF fiber stretch during lateral flexion: (a) at 10s - end of pre-conditioning period; (b) at 12s - end of loading period.	48
Figure 3.18 - Angular range of bilateral flexion movement.	48
Figure 3.19 - NP pressure variation during axial rotation.	49
Figure 3.20 - AF pressure variation during axial rotation.	49
Figure 3.21 - NP and AF volume variation during axial rotation.	50
Figure 3.22 - AF fiber stretch during axial rotation: (a) at 10s - end of pre-conditioning period; (b) at 12s - end of loading period.	51
Figure 3.23 - Angular range of axial rotation movement.	51
Figure 3.24 - NP pressure variation during extension.	52
Figure 3.25 - NP pressure variation during flexion.	53

Figure 3.26 - AF pressure variation during extension.....	53
Figure 3.27 - AF pressure variation during flexion.	54
Figure 3.28 - NP and AF volume variation during extension.	54
Figure 3.29 - NP and AF volume variation during flexion.	55
Figure 3.30 - AF fiber stretch during extension: (a) at 10s - end of pre-conditioning period; (b) at 12s - end of loading period.	55
Figure 3.31 - AF fiber stretch during flexion: (a) at 10s - end of pre-conditioning period; (b) at 12s - end of loading period.	56
Figure 3.32 - Angular range of extension-flexion movement.....	56
Figure 3.33 - NP pressure variation during lateral flexion.	57
Figure 3.34 - AF pressure variation during lateral flexion.	57
Figure 3.35 - NP and AF volume variation during lateral flexion.....	58
Figure 3.36 - AF fiber stretch during lateral flexion: (a) at 10s - end of pre-conditioning period; (b) at 12s - end of loading period.	58
Figure 3.37 - Angular range of bilateral flexion movement.....	59
Figure 3.38 - NP pressure variation during axial rotation.....	60
Figure 3.39 - AF pressure variation during axial rotation.....	60
Figure 3.40 - NP and AF volume variation during axial rotation.....	61
Figure 3.41 - AF fiber stretch during axial rotation: (a) at 10s - end of pre-conditioning period; (b) at 12s - end of loading period.	61
Figure 3.42 - Angular range of axial rotation movement.....	62
Figure 4.1 - Schematic representation of a general MBS (Adapted from [89]).....	63
Figure 4.2 - Original model with the referential system highlighted.	65
Figure 4.3 - Schematic representation of the IVD modeling.	66
Figure 4.4 - Extension-flexion FEM results.....	68
Figure 4.5 - Lateral flexion FEM results.....	68
Figure 4.6 - Axial rotation FEM results.	69
Figure 4.7 - Segmentation and linearization of the L2-L3 Ex-Fx FEM result.	70
Figure 4.8 - Three-dimensional MBS model of the lumbar spine: (a) anterior view; (b) left lateral view; (c) posterior view.....	71
Figure 4.9 - Incremental moment applied.....	72

Figure 4.10 - Extension-flexion FEM and MBS simulation results of L1-L2.....	73
Figure 4.11 - Extension-flexion FEM and MBS simulation results of L2-L3.....	73
Figure 4.12 - Extension-flexion FEM and MBS simulation results of L3-L4.....	74
Figure 4.13 - Extension-flexion FEM and MBS simulation results of L4-L5.....	74
Figure 4.14 - Extension-flexion FEM and MBS simulation results of L5-S1.	75
Figure 4.15 - Lateral flexion FEM and MBS simulation results of L1-L2.	75
Figure 4.16 - Lateral flexion FEM and MBS simulation results of L2-L3.	76
Figure 4.17 - Lateral flexion FEM and MBS simulation results of L3-L4.	76
Figure 4.18 - Lateral flexion FEM and MBS simulation results of L4-L5.	77
Figure 4.19 - Lateral flexion FEM and MBS simulation results of L5-S1.	77
Figure 4.20 - Axial rotation FEM and MBS simulation results of all modeled IVDs.	78
Figure 4.21 - Comparison between experimental and simulation results of L1-L2 during Ex-Fx..	79
Figure 4.22 - Comparison between experimental and simulation results of L2-L3 during Ex-Fx..	80
Figure 4.23 - Comparison between experimental and simulation results of L3-L4 during Ex-Fx..	80
Figure 4.24 - Comparison between experimental and simulation results of L4-L5 during Ex-Fx..	81
Figure 4.25 - Comparison between experimental and simulation results of L5-S1 during Ex-Fx.	81
Figure 4.26 - Total range of motion during Ex-Fx of both experimental and simulation results. ...	82
Figure 4.27 - Comparison between experimental and simulation results of L1-L2 during LFx.	83
Figure 4.28 - Comparison between experimental and simulation results of L2-L3 during LFx.	83
Figure 4.29 - Comparison between experimental and simulation results of L3-L4 during LFx.	84
Figure 4.30 - Comparison between experimental and simulation results of L4-L5 during LFx.	84
Figure 4.31 - Comparison between experimental and simulation results of L5-S1 during LFx.	85
Figure 4.32 - Total range of motion during LFx of both experimental and simulation results.	86
Figure 4.33 - Comparison between experimental and simulation results of L1-L2 during AR.	87
Figure 4.34 - Comparison between experimental and simulation results of L2-L3 during AR.	87
Figure 4.35 - Comparison between experimental and simulation results of L3-L4 during AR.	88
Figure 4.36 - Comparison between experimental and simulation results of L4-L5 during AR.	88
Figure 4.37 - Comparison between experimental and simulation results of L5-S1 during AR.	89
Figure 4.38 - Measured reaction forces (X-axis) when different loads are applied in X-axis.	90
Figure 4.39 - Measured reaction forces (Z-axis) when different loads are applied in X-axis.....	91
Figure 4.40 - Measured reaction forces (Y-axis) when different loads are applied in Y-axis.....	92

Figure 4.41 - Measured reaction forces (Z-axis) when different loads are applied in Y-axis..... 92

Figure 4.42 - Measured reaction forces (X-axis) when different loads are applied in Z-axis..... 93

Figure 4.43 - Measured reaction forces (Z-axis) when different loads are applied in Z-axis..... 93

List of Tables

Table 3.1 - Material properties of the model components.	36
Table 3.2 - Settings of the AF's fibers.	37
Table 3.3 - Inputted scale factors and resulting IVD heights.	39
Table 4.1 - World position, orientation and mass of the vertebrae (Adapted from [87]).	65
Table 4.2 - World position, orientation and thickness of all IVDs (Adapted from [87]).	66
Table 4.3 - Wedge angle of the different MBS lumbar levels and corresponding FEM model's angle.	67
Table 4.4 - Segmentation parameters for L2-L3 Ex-Fx movement.	71

CHAPTER 1

Introduction

1.1. Motivation and Scope

Chronic diseases have been frequently reported as the most common cause of mortality, with 63% of deaths worldwide. Since 2012, about half of all adults (117 million people) have one or more chronic health conditions. It is estimated that one of four adults has two or more chronic health conditions [1]. Seven of the top 10 causes of death in 2010 were chronic diseases, such as heart disease, stroke, cancer, chronic respiratory diseases or diabetes, among others. In the USA, the national health care system invests about 75% of their money in the treatment of chronic diseases. The principal consequences of these persistent conditions are lifelong disability, compromised quality of life, and burgeoning health care costs [2].

Among the wide range of chronic pathologies, chronic rheumatic conditions are a subgroup of diseases which include approximately 200 pathologies and syndromes that affect directly the musculoskeletal system, being progressively symptomatically and usually associated with acute pain. Musculoskeletal conditions are leading causes of morbidity and disability, giving rise to enormous healthcare costs and loss of work. Rheumatoid arthritis, osteoarthritis, osteoporosis, severe limb trauma and spinal disorders are the chronic rheumatic pathologies with more impact on the society [3].

Being the main cause for incapacity, spinal disorders include trauma, mechanical injury, spinal cord injury, inflammation, infection and tumor. About 80-85% of back pain episodes have unknown cause [4]. Spinal disorders are highly associated with rachialgia or back pain in the vertebral column. Low back pain (LBP) is the most common type of rachialgia, and it is considered a symptom rather than a disorder [5]. About 70-85% of the general population have LBP at some time in life. The annual prevalence of back pain ranges from 15% to 45% [6].

In the USA, low back pain is the most common cause of activity limitation in people younger than 45 years; the second most frequent reason for visits to the physician; the fifth-ranking cause

of admission to hospital; and the third most common cause of surgical procedures [7-9]. The data from western countries are similar. In the UK, LBP is the largest single cause of absence from work, and it is responsible for approximately 12.5% of all sick days [10]. Similarly, in Sweden, 11-19% of all 1987's annual sickness absence days were taken by people with a back pain diagnosis. About 13.5% of all reported sick days in Sweden happened due to back pain episodes. Overall, approximately 8% of the insured Swedish population were listed as sick with a diagnosis of back pain at some time during 1987 [11].

Lumbar disc disease has been identified as the most common cause of LBP [12]. This evidence became the motivation for this work, whose purpose is to study the biomechanical behavior of the lumbar IVDs in a healthy situation, which may posteriorly serve as a basis to study situations of degeneration and possible solutions for these disorders.

1.2. Literature Review

Throughout the years, the scientific community have been developing and optimizing mathematical models for biological simulation. Numerical modeling is an advantageous approach because it is non-invasive, low cost and it can reproduce the most complex aspects of the biological processes. In addition, numerical modeling can reproduce situations which would be hardly reproduced through other approaches. With the arise of high-speed computers, such models can become powerful tools to understand, prevent and help treat several health conditions or injuries [13,14].

Several models regarding specific spine components (articular facets, intervertebral discs (IVDs), ligaments, among others), motion segments (MSs), spinal regions or even the whole spine, are described in the literature. In such models, the most used computational methodologies are the finite element method (FEM) and multibody system (MBS) dynamics, being the finite element (FE) approach more frequently used in biomechanical studies of the human spine, due to a better and more complex representation of the spine components [15]. On the one hand, MBSs consist of rigid bodies linked through kinematic joints and elements applying forces. On the other hand, FE systems are able of producing highly detailed models by dividing the entities into smaller elements, connecting those by nodes, and producing the realistic material behavior by employing

governing equations into a FE algorithm. MBS models are less complex, requiring less computational power and simpler validation requirements, in comparison with FE models [16,17].

1.2.1. Finite Element Method approaches

The first spine models using FE approach were very simple in terms of geometry and material properties [18]. In 1974, Belytschko *et al.* developed a model with two vertebral bodies (VBs) and an IVD (with no internal morphology defined) with linear material properties [19]. In the coming years, researchers started to define the internal structures, and in 1977, Carter proposed a vertebral model with both trabecular and cortical bone [20]. Further advances concerned the implementation of the remaining spinal components, such as, articular facets (and the contact between them), ligaments and muscles [21,22].

With the advance on medical imaging techniques and reconstruction algorithms, the accuracy of the model's geometry increased, being obtained from computed tomography (CT) or magnetic resonance imaging (MRI) [23]. With the arise of more accurate experimental data and constitutive equations, the materials properties became more complex, enhancing the understanding on the mechanical response of the different spine components [24].

Due to its complex biomechanical behavior, the IVD is the most critical component on FE modeling of the spine [25]. The evolution of FE modeling of the IVD concerned not only its material properties, but also its geometry ranging from two-dimensional to patient-specific three-dimensional models obtained by medical imaging reconstruction [26,27].

In early models, the IVD components consisted of only one phase with a simple linear elastic representation [28]. Such models presented inaccurate results, as the nonlinear behavior of the disc under loading was not considered [29].

In 1999, Kumaresan *et al.* provided a FE model with an improved representation of the annulus geometry and material properties, considering the existence of concentric laminae of collagen fibers [30]. Posteriorly, similar models were developed with collagen fibers modeled as tension-only elements [31] or rebar elements with a fixed inclination [32].

The following FE models started to incorporate radially dependent inclination and stiffness for the collagen fibers as described by Schmidt *et al.*, and the material properties used for these elements were linear elastic or viscoelastic [33].

In several studies, the nucleus pulposus (NP) was modeled as an incompressible hydrostatic material [32,34]. Wang *et al.* presented, in 1997, a three-dimensional model of a lumbar IVD concerning both nucleus and annulus (with its collagen network) material properties [35]. The FE mesh of the model highlighting the different structures is presented in Figure 1.15.

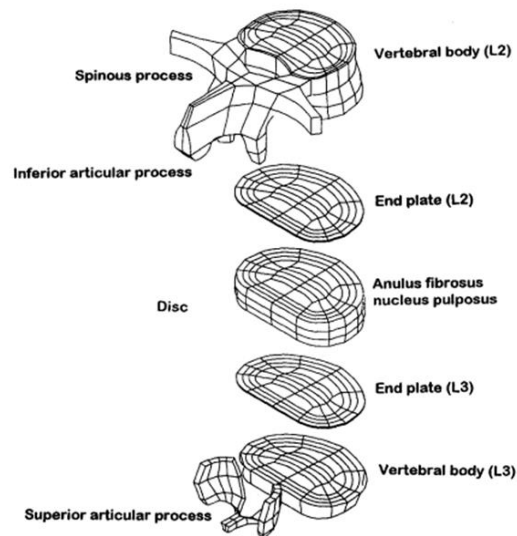


Figure 1.1 - FE mesh of the L2-L3 MS model of Wang *et al.* highlighting its different structures (Adapter from [35]).

The work of Simon *et al.*, in 1985, described the introduction of biphasic formulation in the mechanical properties of the IVD. This FE formulation considers two phases, one liquid and one solid [36]. This model was later improved with the incorporation of swelling pressure and osmotic pressure by Laible *et al.* and Simon *et al.* [37,38].

In 2004, Ferguson *et al.* proposed coupled poroelastic and mass transport FE models to predict the influence of load-induced fluid flow on mass transport within the disc. Their aim was the determination of the fluid flow patterns within the IVD resulting from the average diurnal spinal loading and the analysis of the relative contribution of diffusion and convection to solute transport in the IVD [39]. Figure 1.16 shows the FE mesh, emphasizing the different structures.

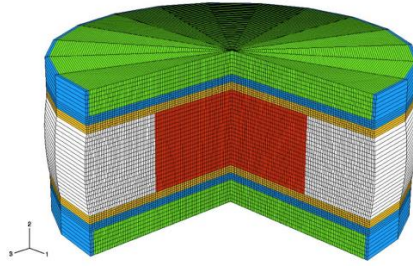


Figure 1.2 - FE model a lumbar IVD proposed by Ferguson *et al.* The different colors of the three-dimensional mesh represent the distinct components of the IVD (Adapted from [39])

Natarajan *et al.* developed, in 2007, a poroelastic FE model of the IVD (Figure 1.17) incorporating the swelling pressure and the effect of strain on the IVD permeability. The model was simulated in order to predict the failure initiation and progression in a lumbar disc due to repeated loading [40].

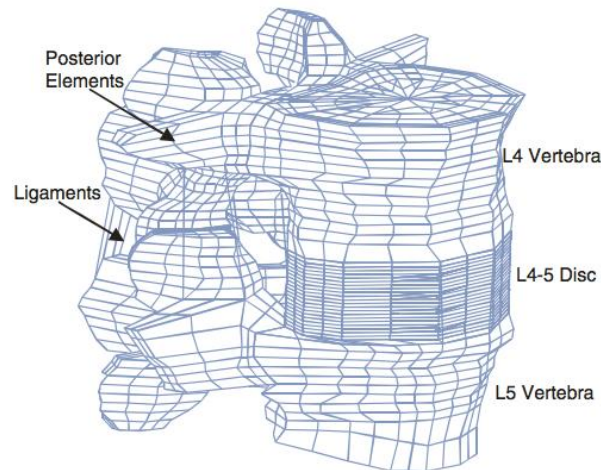


Figure 1.3 - FE model of a L4-L5 MS proposed by Natarajan *et al.* (Adapted from [40]).

In 2007, Schroeder *et al.* proposed an osmoporoviscoelasticity formulation to model the material properties of the IVD. Such formulation considers the IVD's microstructure (composition) to model the material properties, including the contribution of the elastic nonfibrillar solid matrix, the viscoelastic collagen fibers and the osmotically pre-stressed permeable extrafibrillar fluid [41]. Figure 1.18 depicts the IVD's FE mesh.

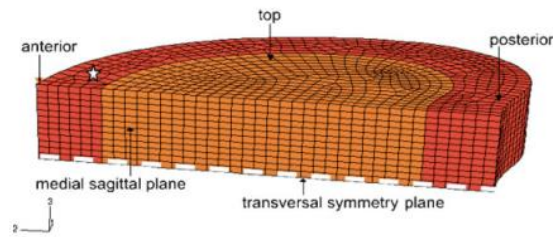


Figure 1.4 - FE mesh of one quarter of an IVD proposed by Schroeder *et al.* (Adapted from [41]).

The work of Strange *et al.*, in 2010, described a three-dimensional FE model of the L4-L5 IVD (Figure 1.19), where the NP was modeled as a hyperelastic solid and the AF as a matrix of homogenous ground substance reinforced by rebar elements. The model was used to verify if an elastomeric implant for a nucleotomized IVD approximates the nucleus properties under compressive loading [42].

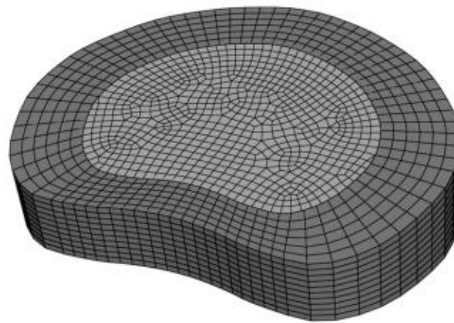


Figure 1.5 - Three-dimensional FE mesh of a lumbar IVD developed by Strange *et al.* (Adapted from [42]).

Huang *et al.* proposed, in 2014, a three-dimensional FEM model of a lumbar (L4-L5) MS (Figure 1.20) to simulate the biomechanical behavior of herniated discs. The model's geometry was obtained from high-resolution computed tomography (CT). Both NP and AF were modeled as isotropic, incompressible and hyperelastic materials. Quadrilateral shell elements were used to model the CEPs. In addition, the vertebrae comprised both cortical and cancellous bone, and seven spinal ligaments were implemented with linear behavior. The model was simulated in several herniation stages, with NP removal and NP replacement. Results reveal the feasibility of this model for studies concerning the mechanical characterization of NP removal and the mechanical stability of NP removal [43].

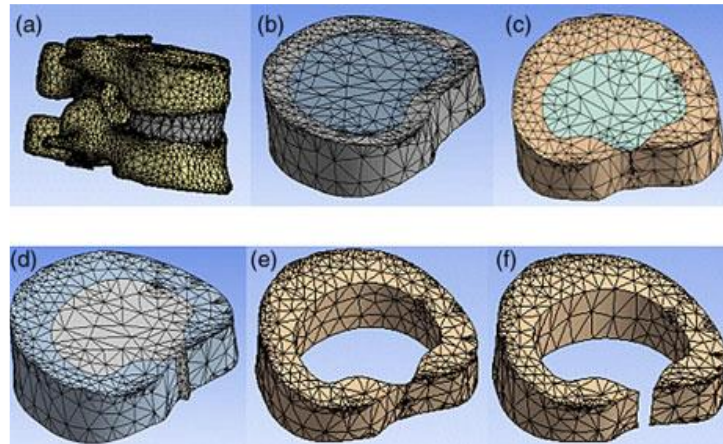


Figure 1.6 - Huang's FE mesh of (a) the lumbar MS, (b) a healthy disc, (c) a mildly herniated disc, (d) a severely herniated disc, (e) a mildly herniated disc with NP removal, and (f) a severely herniated disc with NP removal. (Adapted from [43]).

In 2013, Castro developed a MS FE model that included an IVD with a novel osmo-hyper-poro-visco-elastic formulation reinforced by anisotropic AF fibers. The model was implemented within a custom FE solver under several loading profiles, being validated with both experimental and numerical data. The simulation's main outcomes concerned displacement, pressure, volume variation and fiber stretch of the lumbar IVD. This model proved to be a reliable tool for understanding and reproducing the IVD's biomechanics [44,45].

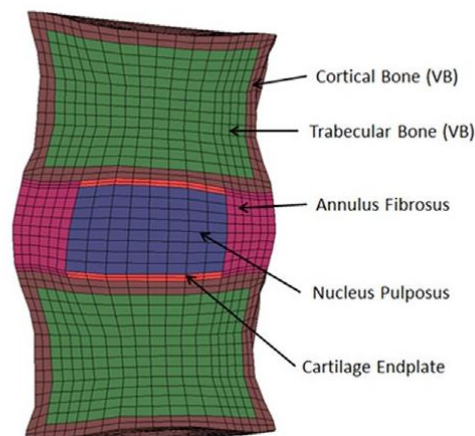


Figure 1.7 - Anterior-posterior cut of the FE mesh of a lumbar MS developed by Castro (Adapted from [44]).

The IVD FE models may be used to simulate normal and irregular situations (disc degeneration) experienced by the disc, being powerful tools to understand the mechanical behavior of this structure, and providing a significant contribute to help the prevention and treatment of disorders associated to the IVD.

1.2.2. Multibody System Dynamics approaches

The development of spine models, using both MBS and FEM formulations, has evolved greatly since 1957, when Latham described an analytical model of the spine, aiming to study pilot ejections [46]. The MBS first spine models were unsophisticated, consisting of a small number of rigid bodies linked by simple mechanical joints. Such models provided a first approach to the complex mechanical response to impact of the whole spine [47].

In 1981, Merrill developed a model with ten rigid bodies, representing the head, cervical and thoracic vertebrae that were connected by massless springs and hysteretic elements. Seven pairs of muscles were also modeled as linear elements [48], being the number of muscles later increased to twenty eight [49].

Two years after, in 1983, Williams and Belytschko developed a three-dimensional human cervical spine model for impact simulation. Rigid bodies modelled the head and cervical vertebrae, which were interconnected by deformable elements representing the IVDs, facet joints, ligaments and muscles. The most relevant novelty presented in this model was the pentahedral continuum element which represented the facet joint, allowing both lateral and frontal plane motion [17].

Based on the work of Merrill *et al.* [48,49], Deng *et al.* defined a computational model for predicting sagittal-plane motion of the human head-neck during impact. The model was validated against frontal and lateral acceleration impacts results, from physical spine models and from volunteers. It was composed by human cervical and thoracical vertebrae, assumed as rigid bodies interconnected by intervertebral joints, an also fifteen pairs of muscles, represented as linear elements. Nonetheless, the individual contributions other structures involved in a intervertebral joint, such as ligaments, were not implemented [50].

In 1996, Broman *et al.* developed a numerical model of the lumbar spine (Figure 1.1), pelvis and buttocks to study the influence of vibrations from the seat to the third lumbar vertebra (L3), of individuals in sitting posture. The skeletal system was defined as rigid and soft tissues were modeled as linear components [51].

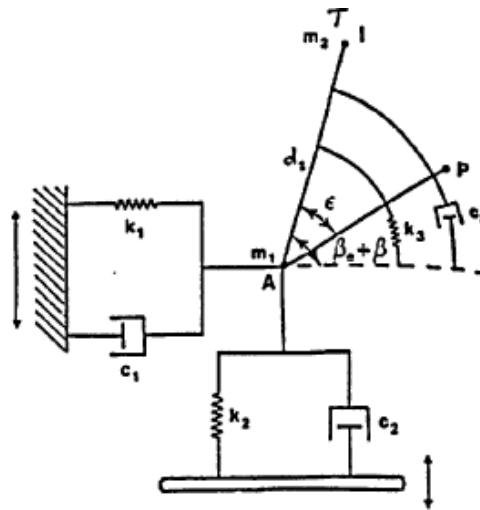


Figure 1.8 - Modeling components from the work of Broman *et al.* (Adapted from [51]).

The study of Stokes *et al.*, in 1999, described the development of a rigid model (Figure 1.2) to study muscles and spinal forces. This model consisted of five lumbar vertebrae, twelve thoracic vertebrae, the sacrum and sixty-six muscles. Two models with the same geometry and different properties were created: (i) the stiffness model, with the vertebrae modeled as beams with predetermined stiffness properties, and (ii) the static model, with the vertebrae were interconnected by ball-and-socket joints. Both models were subjected to flexion, extension, lateral bending and axial torque [52].

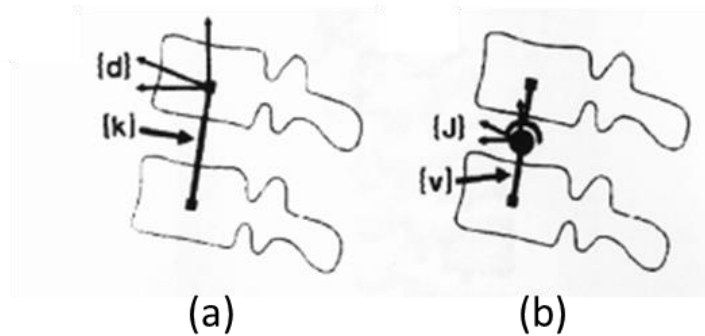


Figure 1.9 - Schematic representation of the models by Stokes *et al.*: (a) Stiffness model; (b) Static model (Adapted from [52]).

In 2000, De Jager improved the work of Deng *et al.* [50] with the implementation of active muscle behavior and by lumping the behavior of all soft tissues into the intervertebral joints. Their model was developed in three stages: (i) a global head-neck model was built with rigid head and vertebrae, linked through three-dimensional nonlinear viscoelastic elements that lumped the IVD's

characteristics, ligaments and facet joints; (ii) detailed segments of the cervical spine were proposed, with three-dimensional elements for the IVD, nonlinear viscoelastic elements for the ligaments, and frictionless contacts in the facet joints; (iii) Hill-type muscles were included in the model [53]. Figure 1.3 depicts the schematic representation of De Jager's global model with local coordinate system.

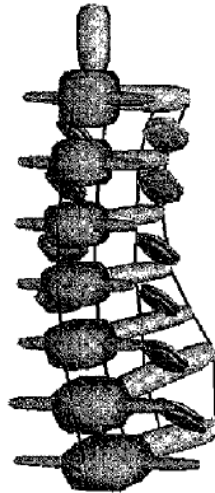


Figure 1.10 - Partial representation of De Jager's model (Adapted from [53]).

After several tests, calibration with data from human volunteers, De Jager concluded that the active muscle behavior was essential to describe the system's response to impact and that his model was computationally efficient [53].

Waters *et al.* developed, in 2003, a MBS model for the assessment of low back disorders due to occupational exposure to jarring and jolting from operation of heavy mobile equipment. Firstly, the model comprised seventeen rigid bodies, which was later replaced by a simpler approach. The model consisted of four rigid bodies representing head/neck and upper, middle and lower torso, linked by spring-damper sets. It was used to simulate spinal motion [54]. A schematic representation of such model is presented in Figure 1.4.

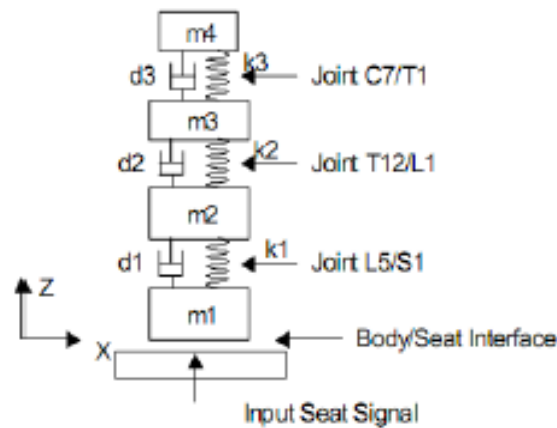


Figure 1.11 - Human spine MBS model developed by Waters *et al.* (Adapted from [54]).

A study of Ishikawa *et al.* described, in 2005, a musculoskeletal dynamic spine model (Figure 1.5) that was able to perform functional electrical stimulation, spine motion simulation and stress distribution analysis. The skeletal geometry was built from computed tomography (CT) data from one healthy volunteer. Afterwards, muscles were added to the model using Nastran® software, and IVDs and ligaments were modeled as spring-damper sets. Dynamic simulation was performed using Nastran® [55].

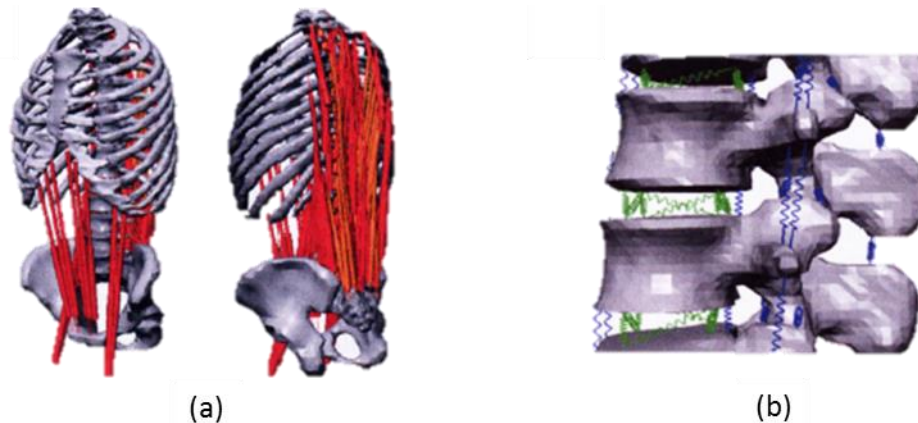


Figure 1.12 - Three-dimensional MBS model of the human spine developed by Ishikawa *et al.*: (a) General view; (b) Detailed representation of the IVDs and ligaments (Adapted from [55]).

In 2006, Esat developed a hybrid model of the whole spine with active-passive muscles and geometric nonlinearities. This model comprised a MBS used for dynamic analysis of impact situations, and a FE analysis to study the causes of spinal injuries. CT imaging data was used to build the model's geometry. The vertebrae were modeled as rigid bodies, linked by linear

viscoelastic IVD elements, nonlinear viscoelastic ligaments and contractile muscle elements with both passive and active behavior. Contact forces were disregarded in this model [17]. Figure 1.6 depicts the lumbar region of Esat's MBS model.

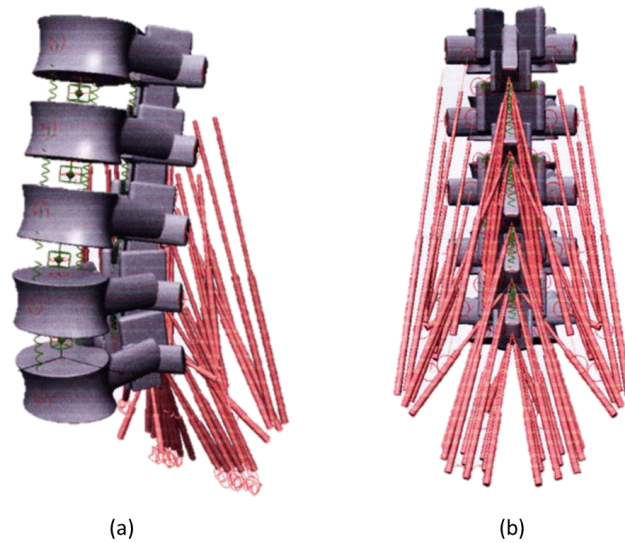


Figure 1.13 - Lumbar spine MBS model developed by Esat (Adapted from [17]).

Ferreira established, in 2008, a three-dimensional cervical MBS spine model with seven rigid bodies (head, seven cervical vertebrae and the first thoracic vertebra), linked by six bushing elements with six DOF each (playing the role of the IVD) and constrained by nonlinear viscoelastic elements simulating the spinal ligaments. Contacts between spinous processes and facet joints were implemented as sphere-plane nonlinear contact forces, following the Kelvin-Voigt formulation. The model aims to simulate the traumatic and degenerative disorders, such as rheumatoid arthritis [56]. In Figure 1.7 are presented the sagittal and frontal views of the model during an impact situation.

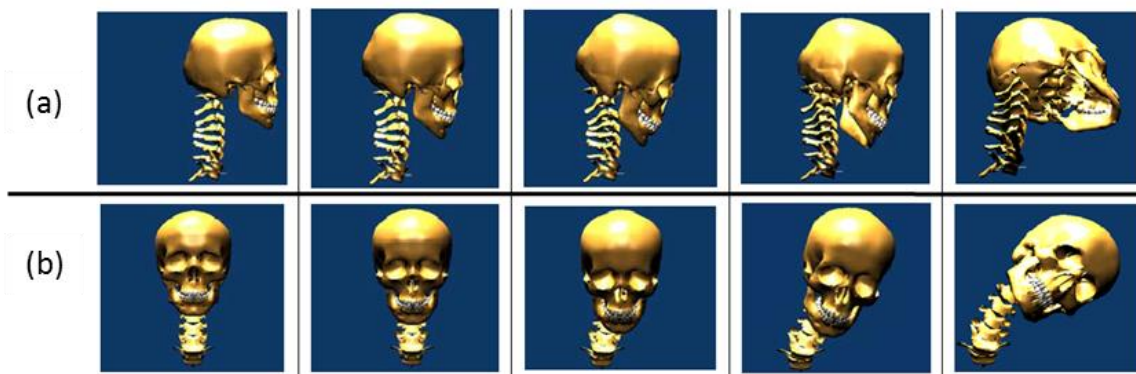


Figure 1.14 - Sequential representation of the lateral impact of Ferreira's model: (a) lateral view; (b) frontal view (Adapted from [56]).

The work developed by Juchem, in 2009, comprised a three-dimensional computational model of the lumbar spine (Figure 1.8) for mechanical stress determination. Five rigid bodies modeled the last four lumbar vertebrae and the sacrum. Geometry data was obtained through CT measurements. MBS formulation was applied and the IVDs were modeled as elastic elements. The effect of ligaments and facet joints were also implemented. The model was simulated with an applied load of 395 N at the top of the second lumbar vertebra mimicking the upper body's weight. Thus, the reaction forces and torques of each IVD, and the reaction forces of ligaments were calculated [57].



Figure 1.15 - Three-dimensional model of the lumbar spine developed by Juchem (Adapted from [57]).

Monteiro, in 2009, proposed a hybrid model (Figure 1.9) of the cervical and lumbar spine model, using both FEM and MBS. His model aimed the analysis of the intersomatic, or vertebral fusion of one or more spine levels. MBS formulation was used to model vertebrae as rigid bodies, IVDs as linear viscoelastic bushing elements, ligaments as nonlinear elastic springs, and spinal contacts according to the nonlinear Kelvin-Voigt contact model. Muscles were disregarded from the model. FEM modeling was applied to the four IVDs with greater incidence of degeneration, and to the fixation plate (used for intersomatic fusion). A 1.5 Nm torque was applied to the first lumbar vertebra (L1) for 400 ms, while the sacrum (S1) was fixed. A 500 N load submitted to the upper surface of L1 was used to simulate the upper body weight. The model confirmed its capacity of predicting accurately axial rotation and extension movements [58].

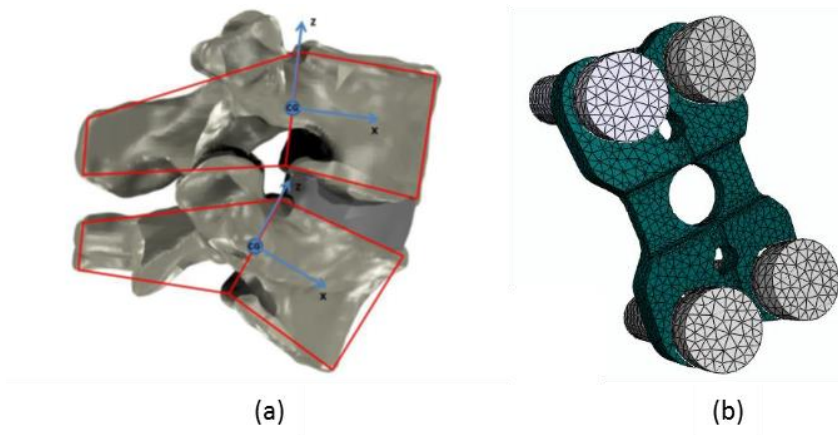


Figure 1.16 – Lumbar hybrid model developed by Monteiro: (a) three-dimensional MS; (b) FE mesh of the fixation plate and screws (Adapted from [58]).

In 2010, Christophy developed an open-source musculoskeletal model of the human lumbar spine, focusing on the effect of muscles during spinal motion. The 6 DOF intervertebral joints and the muscles are governed by the Hill-type and Thelen's muscle models. The model was simulated in flexion-extension movement focusing on the L5-S1 joint. Results revealed different behaviors of two groups of muscles: (i) the primary flexor muscles generated significant larger moments (approximately 60 Nm) than the (ii) stabilizer muscles (approximately 10 Nm). Despite the results, the lack of ligaments and contact between facet joints limits the accuracy of the model [59]. Figure 1.10 depicts two different configurations of the model (neutral and in 50° flexion) where muscles, rigid bodies and intervertebral joints are evidenced.

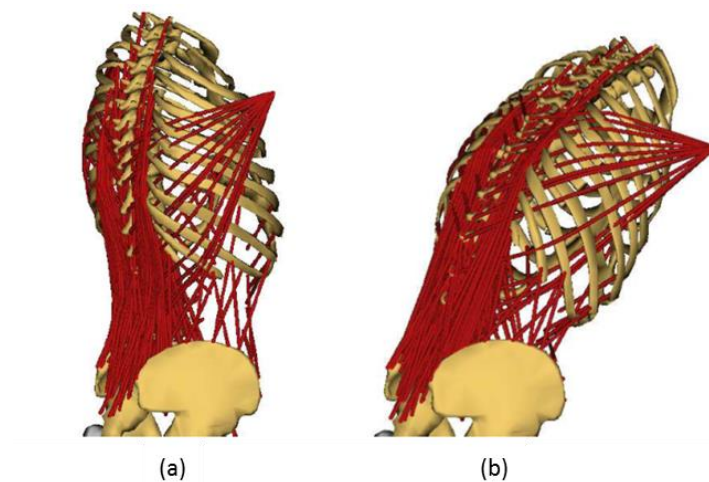


Figure 1.17 - Cristophy's three-dimensional musculoskeletal model with 238 muscles, 13 rigid bodies and 5 intervertebral joints: (a) neutral posture; (b) 50° flexion (Adapted from [59]).

On the study of Abouhossein *et al.*, in 2010, a three-dimensional MBS lumbar spine model (Figure 1.11) was proposed. The model aimed the determination of load sharing between the passive elements of the lumbar spine. It consisted of six rigid bodies for the five lumbar vertebrae and the sacrum, six DOF nonlinear flexible for the IVDs, tension-only force elements for ligaments, and Kelvin-Voigt contact forces between facet joints. Muscles were not implemented in the model. To validate the model, *in vitro* data was used to compare the response of pure torque loading of kinematic and facet joint forces [60].

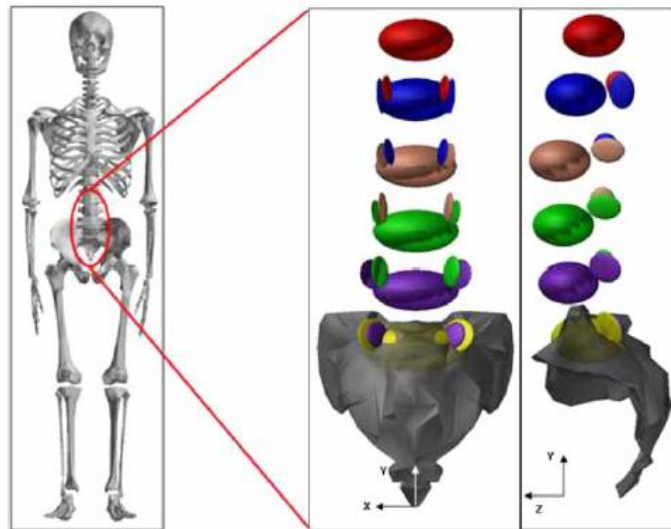


Figure 1.18 - Representation of the lumbosacral spine model developed by Abouhossein (Adapted from [60]).

Galibarov *et al.* described, in 2011, a computational model to investigate the muscular and external forces effects on the lumbar spine's curvature. The model was implemented in Anybody Modeling System® software, where IVDs and ligaments were modeled as spherical joints and nonlinear springs, respectively. Figure 1.12 represents the three-dimensional MBS model, highlighting both ligament and IVD elements [61].

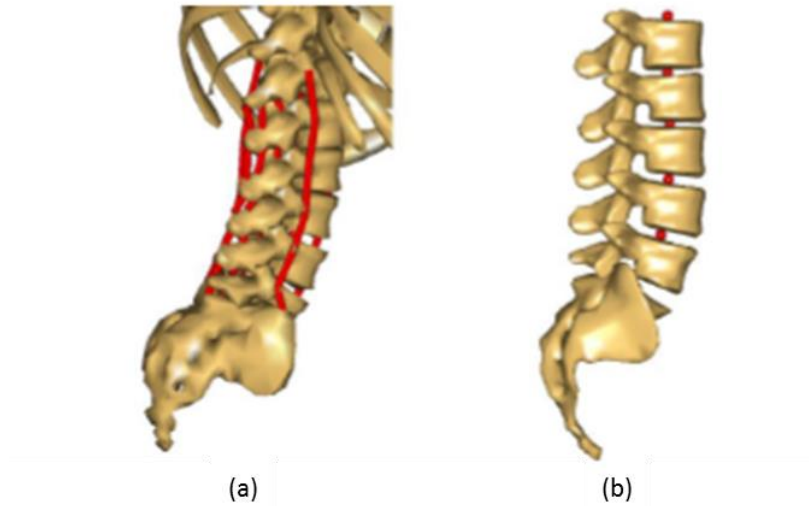


Figure 1.19 - Lumbar spine MBS model of Galibarov *et al.* highlighting: (a) the lumbar ligaments (red segments); (b) the IVDs (red spherical joints) (Adapter from [61]).

In 2012, Han *et al.* developed a thoracolumbar spine model (Figure 1.13) for muscle force prediction. The bones of the model consisted of the skull, arms, legs, pelvis and spine. Cervical and thoracic spine were modeled as single elements. The lumbar region comprised the five rigid bodies linked by rigid spherical joints for the IVDs. Muscles were modeled as single force components. The model's response was validated based on literature data [62].

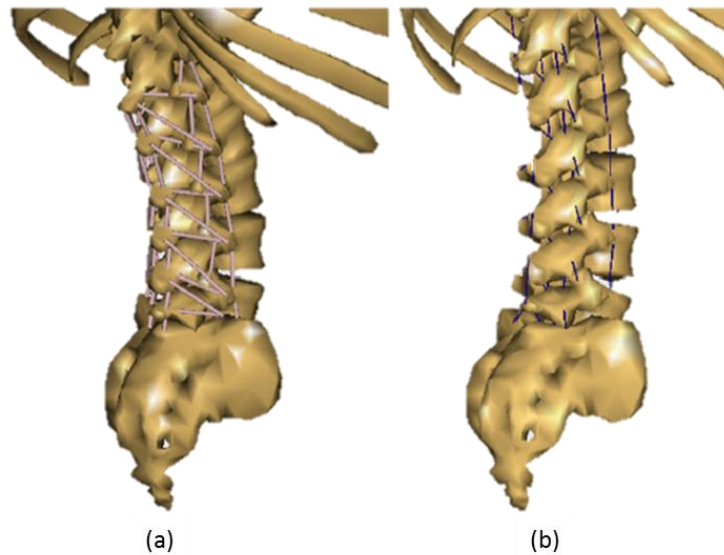


Figure 1.20 - Lumbar MBS model developed by Han *et al.* with emphasis to (a) muscle segments, and (b) ligaments (Adapted from [62]).

More recently, Huynh *et al.* proposed a bio-fidelity discretized musculoskeletal MBS spine model (Figure 1.14) for assessing the biomechanical behavior between healthy spines and spinal arthroplasty or arthrodesis. This model was generated in LifeMOD® software, and comprised several torsional spring forces representing the IVDs. Back ligaments and muscles were added from the software's default library, and their mechanical properties were optimized using literature data. Simulations were performed for different postures and different loading conditions. The model was validated with both experimental data and *in vivo* measurements, proving to be a reliable tool to study spinal disorders [63].

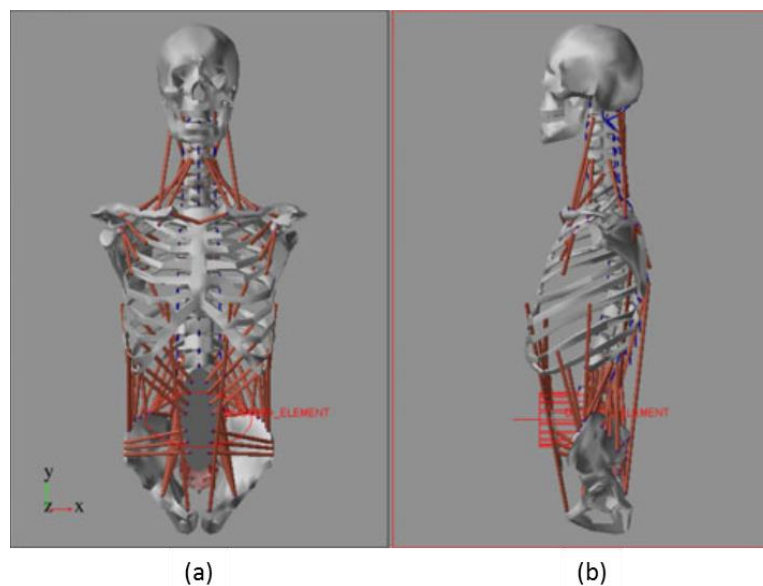


Figure 1.21 - Musculoskeletal spine model developed by Huynh *et al.*: (a) frontal view; (b) lateral view (Adapted from [63]).

Since the first biomechanical spine studies, MBS models evolved significantly, not only in terms of number and type of elements modeled, but also in their complex geometry. This evolution has allowed a more accurate reproduction of the several anatomical elements (muscles, ligaments, facet joints, among others) involved in the biomechanical response of the human spine. The implementation of these different structures in the current models increases their complexity, but allows for a more realistic understanding of the spinal functioning by considering their physiological role in the biomechanics of the spine.

1.3. Objectives

The main goals for the present work are comprised in two phases: first, (i) a geometric sensibility study of the lumbar IVD through FE analysis, and second, (ii) the optimization and validation of a three-dimensional lumbar spine MBS model by implementing the previous FE results.

This research was performed within the co-operative European project “NP Mimetic – Biomimetic Nano Fibre-Based Nucleus Pulposus Regeneration for the treatment of Degenerative Disc Disease” (ref. NMP-2009-SMALL-3 CP-FP 246351).

1.4. Structure of the thesis

The present dissertation contains 5 chapters.

Chapter 1 presents the motivation of this work, a literature review on both FE and MBS modeling approaches of the human spine, and the main objectives of the present work.

Chapter 2 focuses on the spine characterization, giving an anatomophysiological description of the spinal components and the associated disorders.

Chapter 3 contains a brief description of the FE formulation and the IVD model. The IVD’s geometric sensibility analysis is also presented in this chapter.

Chapter 4 starts with the definition of MBS system, and then, a description of the lumbar model is presented. Posteriorly, the mechanical response of both FEM and MBS models are compared. Subsequently, the MBS model is validated using experimental data from the literature, and, finally the application of the model is presented.

Finally, the main conclusions and proposals for future work are enunciated in the Chapter 5.

This dissertation ends with a full list of references consulted during the work development.

As appendix, a table regarding the published range of motion of the lumbar vertebrae is presented.

CHAPTER 2

Spine characterization

2.1 Spinal Anatomy

The human spine or vertebral column is an anatomical structure located in torso's posterior region, being extent from the base of the skull until the pelvis. It is responsible for the spinal cord and spinal nerves protection; body weight support; it has an important role in posture and locomotion; it allows the attachment of ribs, pelvis and back muscles; and it provides body flexibility [64]. Thirty-three vertebrae divided in five different regions constitute this structure:

- Cervical region, composed by seven cervical vertebrae (C1-C7) and its IVDs. Their small VBs, partially bifid spinous processes and a transverse foramen in each transverse process, through which the vertebral arteries extend toward the head, characterize these vertebrae. Only cervical vertebrae have transverse foramina;
- Thoracic region, composed by twelve thoracic vertebrae (T1-T12) and its IVDs. Long and thin spinous processes inferiorly directed and relatively long processes are distinct characteristics of these vertebrae;
- Lumbar region, composed by five lumbar vertebrae (L1-L5) and its IVDs. Large and thick bodies, as well as heavy and rectangular transverse and spinous processes characterize lumbar vertebrae;
- Sacral region, composed by five sacral vertebrae fused into a single bone called sacrum;
- Coccygeal region, composed by four fused vertebrae, the coccyx, also called tailbone. The coccygeal vertebrae are greatly reduced in size relative to the other vertebrae [64].

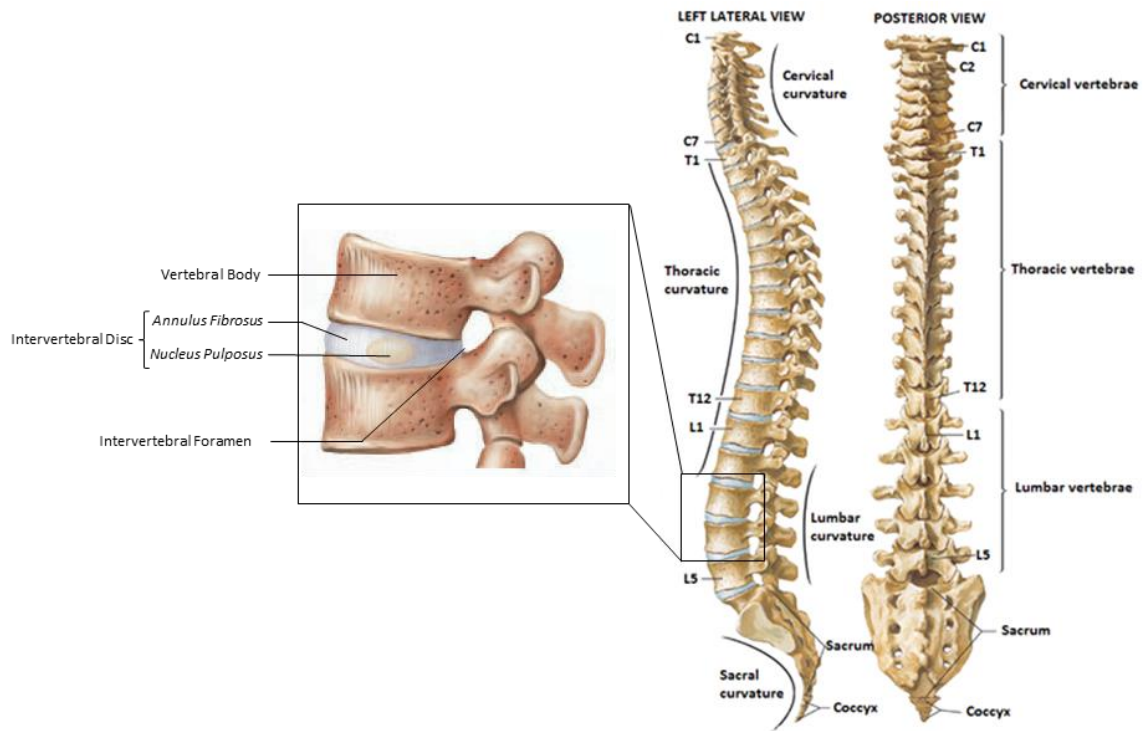


Figure 2.1 - Left lateral and posterior view of the human spine's anatomy, with a lumbar MS highlighted (Adapted from [64]).

The five regions of the human spine have four major curvatures in the sagittal plane (Figure 2.1). These natural curvatures are anatomically named as lordosis (convex anteriorly) and kyphosis (concave anteriorly). Lordosis is present in the spine's cervical and lumbar regions, while kyphosis is present in the thoracic, sacral and coccygeal region. These curvatures exist due to the non-homogeneous thickness of the IVDs. In the case of lordosis, the IVDs are thicker anteriorly than posteriorly. The opposite happens in the case of kyphosis, where the IVDs are thicker posteriorly than anteriorly [65]. In addition, these curvatures enhance the body weight support function of the spine [64]. IVDs (which connects two adjacent vertebrae allowing relative motion), as well as ligaments, muscles, articulations, neural and vascular networks are other anatomical elements that compose the human spine.

The smallest functional unit of the human spine is the motion segment (MS) (Figure 2.1). Two vertebrae connected by an IVD compose each one of these load-sharing units [66].

2.1.1. The vertebrae

The general structure of a vertebra consists of a VB, an arch and various processes (Figure 2.2). The vertebral arch projects posteriorly from the body and it is divided into left and right halves.

Each half has two parts, the pedicle, which is attached to the body, and the lamina, joining the lamina from the opposite half of the vertebral arch. The vertebral arch and the posterior part of the body surround a large opening called the vertebral foramen. The foramina of adjacent vertebrae combine to form the vertebral canal, where the spinal cord is contained. The vertebral arches and bodies protect the spinal cord [64].

Being the largest part of the vertebra, the body is a disc-shaped element with flat surfaces directed superiorly and inferiorly which is essential for loading support. It forms the anterior wall of the vertebral foramen. The IVDs are located between bodies [16].

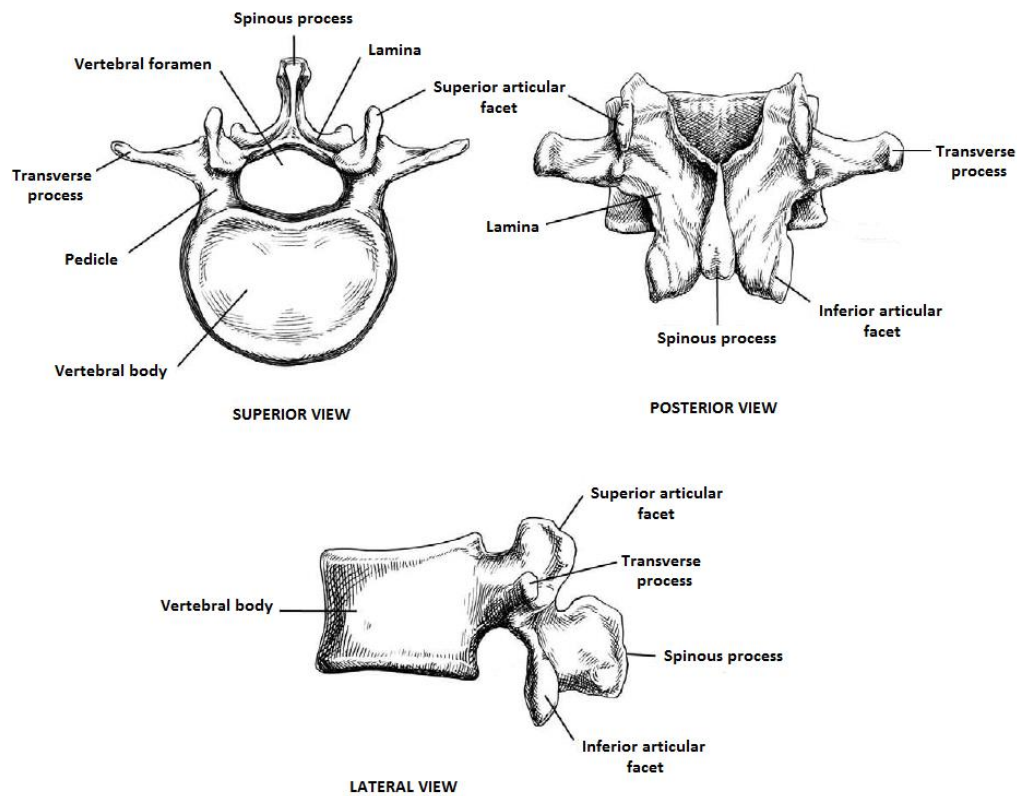


Figure 2.2 - Superior, posterior and lateral view of a typical vertebra (Adapted from [16]).

The transverse processes extend laterally from each side the arch between the lamina and the pedicle. It serves as an attachment place for muscles and ligaments. The spinous processes are projected posteriorly at the point where two laminae join. It is also a site for muscle attachment, strengthening the vertebral column and enhancing movement ability. The spinous processes can be seen and felt as a series of lumps down the midline of the back. The laminae are the posterior parts of the arch and form the posterior wall of the vertebral foramen. The pedicles are the feet of the arch with one on each side of it forming the lateral walls of the vertebral foramen. The articular

processes are superior and inferior projections containing articular facets where vertebrae articulate with each other. The intervertebral foramina are lateral openings between two adjacent vertebrae through which spinal nerves exit the vertebral canal [64].

2.1.1.1. Lumbar vertebrae

As previously mentioned, vertebral characteristics are dependent of their spinal location. As described in Figure 2.3, lumbar vertebrae may be divided into three functional components: VB, pedicles and posterior elements. Each of these components has a unique role contributing to the integrated function of the whole vertebra [67].

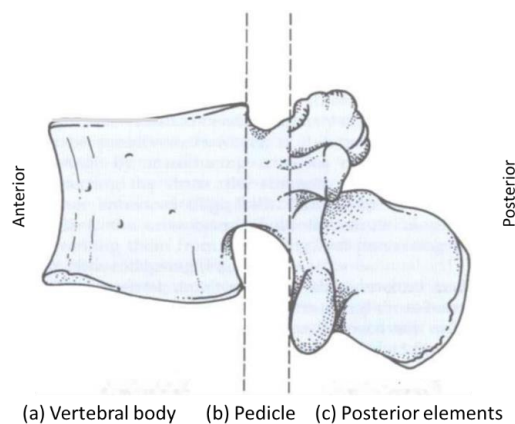


Figure 2.3 – Lumbar vertebra divided by functional parts: (a) Vertebral body, (b) Pedicle, (c) Posterior elements (Adapted from [67]).

The main function of the VB is weight-bearing and its geometrical structure is designed (internally and externally) for that purpose. The lumbar region is subjected to approximately 80% of the compressive loads acting of the human spine. The VB's superior and inferior flat surfaces are dedicated to supporting longitudinally applied loads. While the external design promote a better load support with large and thick bodies, the internal design enhances its response to dynamic loads. With a shell of cortical bone surrounding a cancellous core, the internal architecture is organized for the same load-bearing function. The cancellous core has a grid-like design of vertical and transverse trabeculae which not only enhances the weight bearing purpose of the VB, but also allows the existence of a vascular network [67].

The posterior elements of a vertebra are the laminae, the articular and the spinous processes. Collectively, they form a very irregular mass of bone, with various bars of bone projecting in different

directions. This happens because the various posterior elements are specially adapted to receive the different forces that act on the vertebra [67].

The pedicles are parts of the lumbar vertebrae, which normally are simply named and no specific function is assigned to them. However, they are the only connection between the VBs and the posterior elements. The bodies are designed for weight-bearing but they cannot resist sliding or twisting movements, while the posterior elements are adapted to be submitted to different forces. Thus, all forces sustained by any of the posterior elements are ultimately channeled towards the pedicles, which transmit the benefit of the forces to the VBs [67].

2.1.1.2. Sacrum

The sacrum consists of five vertebrae fused into a single bone. The transverse processes of the sacral vertebrae fuse to form the alae, which join the sacrum to the pelvic bones. The spinous processes of the first four sacral vertebrae are partially fused forming projections, called median sacral crest, along the dorsal surface of the sacrum. The spinous process of the fifth vertebra does not form, thereby leaving a sacral hiatus at the inferior end of the sacrum, which is often the site of anesthetic injections. The intervertebral foramina are divided into dorsal and ventral foramina, called the sacral foramina, which are lateral to the midline. The anterior edge of the first vertebra's body bulges to form the sacral promontory, a landmark that separates the abdominal cavity from the pelvic cavity [64].

2.1.1.3. Coccyx

The coccyx or tailbone, is the most inferior portion of the vertebral column and usually consists of three to five fused vertebrae that form a triangle, with the apex directed inferiorly. The coccygeal vertebrae are smaller when compared to the other vertebrae and they have neither vertebral foramina nor well-developed processes [64].

2.1.2. Facet joints

The facet joints are formed by the articulation of a vertebra's superior articular process and the inferior articular process of the vertebra directly above it. It is a synovial joint covered by hyaline cartilage. A synovial membrane bridges the margins of the cartilage of the two facets in each joint.

The friction between surfaces and the surface wear are decreased by hyaline cartilage and the lubrication of the synovial fluid, respectively. The ligamentum flavum and the posterior longitudinal ligament reinforce the joint capsule which surrounds the synovial membrane.

The lumbar spine articular facets have an ovoid shape, becoming oval from the first to the fifth lumbar vertebra. This joint is oriented perpendicularly to the transverse plane. Shape and orientation variations of the lumbar facet joints limit the movement of this region, specifically in the axial plane [67].

2.1.3. Intervertebral disc

The IVD is an anatomical element that connects two adjacent VBs. It consists of a highly inhomogeneous porous structure with solid and fluid materials [68]. Its complex structure is constituted by a central gel-like core, the nucleus pulposus (NP), which is laterally surrounded by a fiber-layered structure, the annulus fibrosus (AF). Cartilaginous endplates (CEPs) and vertebral endplates (VEPs) vertically limit the IVD. Figure 2.4 depicts the IVD's anatomical organization.

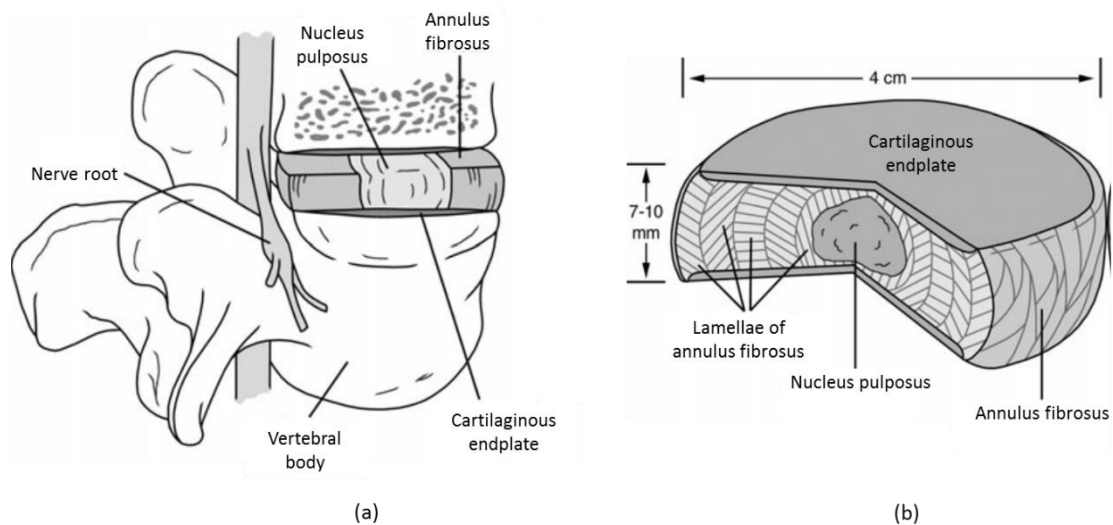


Figure 2.4 - IVD's anatomy: (a) a MS's structural organization; (b) IVD's detailed structures and dimensions (Adapted from [68]).

Lumbar IVDs are the thickest of all vertebral column, varying from 7 to 10 mm in height and from 35 to 55 mm in diameter (axial plane). Contrarily to other anatomical structures, the IVDs do not have blood supply, depending on mechanical means of water absorption for the nutrition process [69].

Beside its function of linking the adjacent vertebrae, the IVD provides flexibility, elasticity and compressibility to the spine, and it allows load transmission [69].

2.1.3.1. Nucleus Pulposus

The NP is the inner part of the IVD that consists of a gelatinous core made of collagen fibers (randomly arranged) and elastin fibers (radially arranged) embedded in a highly hydrated aggrecan-containing gel. Two major regions characterize the NP: a solidified porous center and a peripheral gel-like region. The mainly isotropic, almost incompressible and osmo-poro-visco-hyperelastic properties, as well as the biochemical composition and the spatial confinement between the AF and the CEP are the reasons for the particular mechanical behavior of the NP. Being neither exclusively a solid nor a fluid, the NP is considered a biphasic tissue [44,69].

2.1.3.2. Annulus Fibrosus

The AF is the peripheral part of the IVD, forming a ring around the NP, and consisting on a series of 15 to 20 concentric lamellae of collagen fibers arranged in a highly ordered pattern. Trace amounts of elastin fibers and proteoglycans can also be found in its biochemical composition.

In this structure, two sets of fibers cross obliquely to each other at about ± 30 degrees in relation to the disc. The annulus peripheral layers are denser, more resistant to tensile forces and reinforced by the posterior and anterior longitudinal ligaments. The annular cells are fibroblast-like, elongated and generally aligned with the oriented collagen fiber arrays in the extracellular matrix. As one moves from the outer region into the NP, the cells become more oval, the collagen fibers lose density and organization, and the proteoglycan concentration increases. Functionally, the AF is capable of intradiscal pressure containment and intervertebral motion guidance [44,69].

2.1.3.3. Cartilaginous Endplate

The CEP is a thin horizontal layer (usually less than 1 mm thick) of hyaline cartilage. The collagen fibers within the CEP are oriented horizontal and parallel to the VBs. The CEP behaves as a mechanical barrier between the pressurized NP and the vertebral bone, as well as a pathway for nutrient transport into the disc from adjacent blood vessels. CEPs are distinct from the adjacent VEPs, which are composed of cortical bone [67,70].

Figure 2.5 depicts a sagittal cut of a real IVD, where its structures are highlighted.

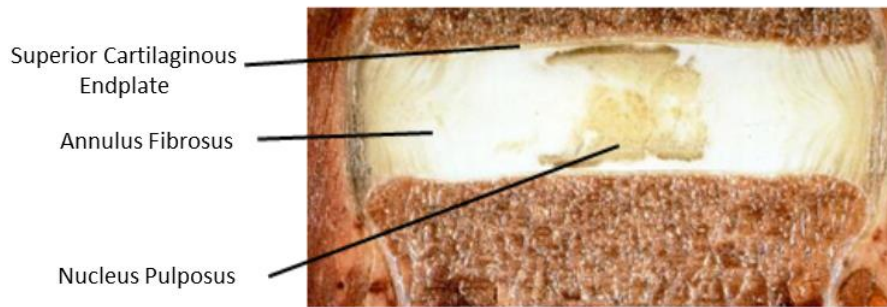


Figure 2.5 - Components of the IVD (Adapted from [71]).

2.1.4. Ligaments

Ligaments are anatomical elements with a complex architectural hierarchy that link two or more bones. Structurally, they are composed by bands of connective tissue with an high water content (55-65%). The remaining dry matter (35-45% of the total weight) is divided in 70-80% type I collagen, 10-15% of elastin and 1-3% of proteoglycans [72]. The hierarchical organization of the ligament is depicted in Figure 2.6.

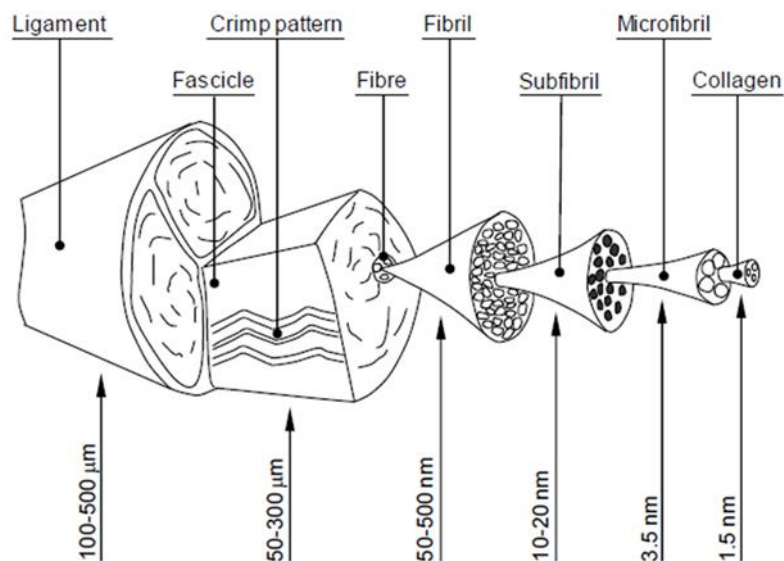


Figure 2.6 - Hierarchical organization of the ligament, components and respective dimensions (Adapted from [72]).

The major function of ligaments is the connection between bones, contributing to structural stability's maintenance. In addition, they enable protection of the neural structures, physiologic

motion range and spine protection against excessive movements. Mainly, the ligament nomenclature depends on its location [73].

At the lumbar level, each MS has seven ligaments: the anterior longitudinal ligament (ALL), the posterior longitudinal ligament (PLL), the ligamentum flavum (LF), the interspinous ligament (ISL), the supraspinous ligament (SSL), the intertransverse ligaments (TTL) and the capsular ligaments (CL) [67]. All these structures can be observed in Figure 2.7.

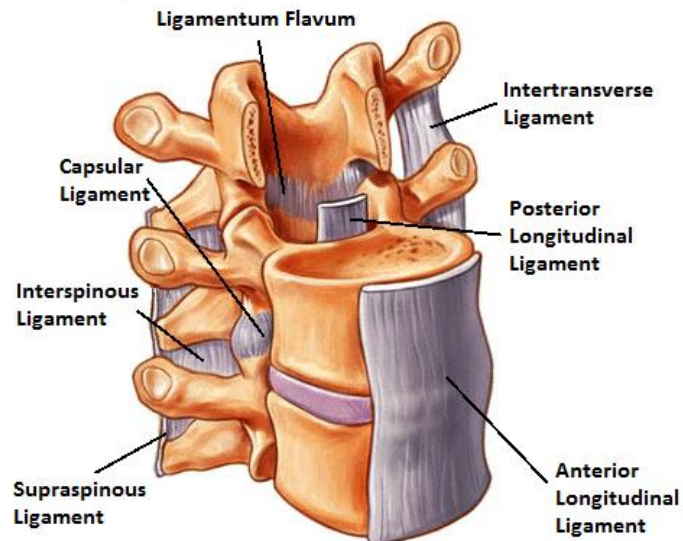


Figure 2.7 - Ligaments of a MS (Adapted from [56]).

2.1.4.1. Anterior Longitudinal Ligament

The anterior longitudinal ligament (ALL) is described as a long band which covers the anterior surfaces of the VBs and IVDs. Although well developed in the lumbar region, this ligament is extended from the cervical region to the sacrum, covering the anterior surface of the whole human spine. Structurally, this ligament consists of several sets of collagen fibers. Some short fibers extend through each interbody joint, covering the IVDs and attaching to the margins of the VBs [67].

2.1.4.2. Posterior Longitudinal Ligament

Similarly to the ALL, the posterior longitudinal ligament (PLL) is represented throughout the vertebral column. In the lumbar region, it forms a narrow band over the back of the VBs but expands laterally over the back of the IVDs to give it a saw-toothed appearance. Its fibers mesh with the AF to attach to the posterior margins of the VBs [67].

2.1.4.3. Ligamentum Flavum

The ligamentum flavum (LF) is a short but thick ligament that joins the laminae of consecutive vertebrae. At each intersegmental level, the LF is a paired structure, being represented symmetrically on both left and right sides. On each side, the upper attachment of the ligament is to the lower half of the anterior surface of the lamina and the inferior surface of the pedicle. Histologically, the ligamentum flavum consists of 80% elastin and 20% collagen [67].

2.1.4.4. Interspinous Ligament

The interspinous ligaments (ISLs) connect adjacent spinous processes. The collagen fibers of these ligaments are arranged in a particular manner, with three parts being identified: ventral, middle and posterior part. These ligaments consist essentially of collagen fibers, but elastin fibers appear with the increasing density of the ventral part towards its junction with the ligamentum flavum [67].

2.1.4.5. Supraspinous Ligament

The supraspinous ligament (SSL) is located in the midline. It runs posteriorly to the posterior edges of the spinous processes, to which it is attached, and bridges the interspinous spaces. The SSL collagen fibers become denser from the superficial to the deepest layers [67].

2.1.4.6. Intertransverse Ligament

The intertransverse ligaments (TTLs) have a complex structure that can be interpreted in many ways. They consist on sheets of connective tissue extending from the upper border of one transverse process to the lower border of the transverse process above. Unlike other ligaments, they lack a distinct border medially or laterally, and their collagen fibers are not as densely packed, nor as regularly oriented as the fibers of other ligaments [67].

2.1.4.7. Capsular Ligament

In general, a capsular ligament (CL) is a part of the articular capsule that surrounds a synovial joint. In the vertebral column, the capsular ligaments are attached to the articular margins of the

articular processes. The fibers are oriented perpendicular to the facet joint and they are stronger in the thoracic and lumbar region than in the cervical region [67].

2.2 Spinal movements

Mechanically, the human spine's behavior can be interpreted as the sum of all individual functional units. Therefore, a single MS has the same type of movements as the whole vertebral column. As described in Figure 2.8, the spine's mobility is provided in its majority by four movements, extension and flexion (anterior and posterior bending in the sagittal plane), lateral flexion (lateral bending in the coronal plane) and axial rotation (around the vertical axis). The extensibility of the ligaments and muscles, and the vertebrae's anatomy provide the degree of movement [74].

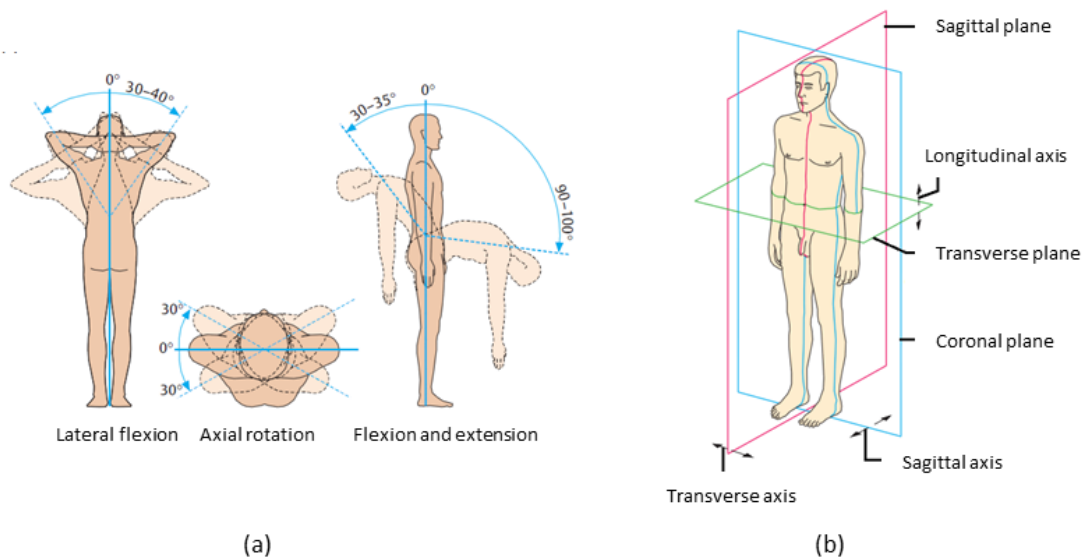


Figure 2.8 - Spinal movements and its anatomical planes and axes. (a) The four principal movements of the human spine: lateral flexion, rotation, flexion and extension; (b) Principal axes and planes of the human body (Adapted from [74]).

The range of movement of the lumbar spine has been studied in different ways. It has been measured in cadavers and in living subjects using either clinical measurements or measurements taken from radiographs. Studies of cadavers have as major disadvantage the post-mortem changes of the structures and the fact that cadavers are usually studied with the back muscles dissected, so the measurements obtained may not accurately reflect the mobility possible in living subjects. However, cadaveric studies have the advantage that motion can be directly and precisely measured

and correlated with pathological changes determined by subsequent dissection or histological studies. Clinical approaches have the advantage to examine living subjects. Although, they are limited by the accuracy of the instruments used and the reliability of identifying bony landmarks by palpation [67].

Each MS of the human spine present six degrees-of-freedom (DOF), three in translation (in each plane: sagittal, coronal and transverse) and three in rotation (around each major axis) (Figure 2.9). In appendix A are described and characterized the limits and ranges of motion of each level of the lumbar spine.

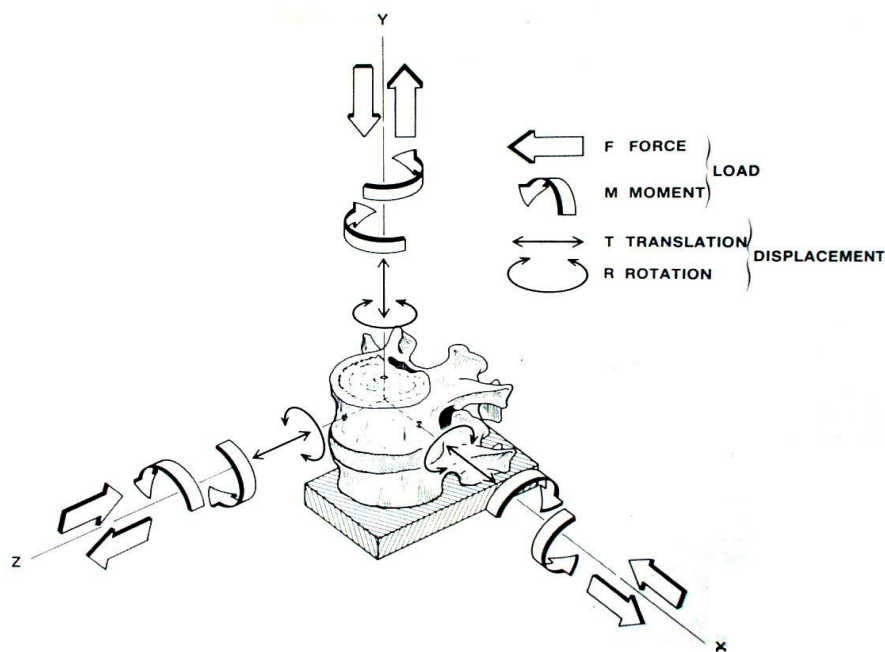


Figure 2.9 - Schematic representation of the 6 DOF of a MS (Adapted from [75]).

2.3 Spinal disorders

Spinal disorders are a wide variety of diseases which affect the various spinal structures. Two major groups distinguish these disorders: the specific and the non-specific disorders. The first group contains 10-15% of all reported spinal disorders, including all those which are directly related to their source, such as congenital, developmental, traumatic, infectious, tumorous, metabolic and degenerative. The non-specific spinal pain is included in the second group, which involves 85-90% of the reported cases [76].

Spinal disorders represent over 50% of the causes for physical incapacity in labor age and are one of the main causes for absence for work. Being generally painful, the most common diseases which affect the human spine are:

- Disc herniation – It can be described as the leakage of the NP through a hole in the wall of the AF. This leakage presses the local nerve root causing pain. The hole in the AF is generally caused by mechanical stress or ageing.
- Degenerative disc disease (DDD) – It is characterized by the gradual deterioration of the disc causing loss of its functions. Generally, it is continuously developed with normal ageing or with continuous activities that compresses the IVD. Normally, it starts with a small injury in the AF, causing damage in the NP and loss of its water content. Further damage causes disc malfunctioning and disc narrowing. In extreme cases, the collapse of the upper and lower vertebrae may occur.
- Spinal stenosis – It concerns to the narrowing of the spinal canal due to mechanical compression of the spinal root by the bones and soft tissues.
- Spinal infection – It occurs when a bacterial infection travels into the IVD through the bloodstream channels. The infection weakens the AF, which may cause total or partial collapse of the disc or nerve root pressure (disc herniation) [76].

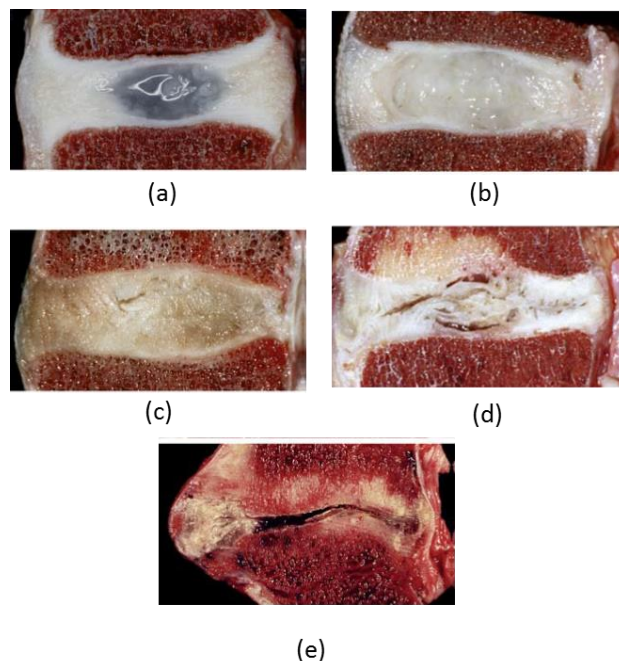


Figure 2.10 - Macroscopic disc changes due to DDD: (a) grade I; (b) grade II; (c) grade III; (d) grade IV; (e) grade V (Adapted from [76]).

2.3.1. Disc Degenerative Disease

The degenerative disc disease (DDD), or spondylosis, is a multi-etiology condition that leads to IVD degeneration. This degeneration is a continuous process, but the morphological changes that occur are macroscopically evident. According to the scale of Thomson, disc degeneration can be identified in five different grades, from I to V: (I) normal juvenile disc, (II) normal adult disc, (III) early stage, (IV) advanced stage, and (V) end stage (Figure 2.10) [76]. Non-invasive medical techniques, such as radiography, computed tomography (CT) and magnetic resonance imaging (MRI), are commonly used in medicine for DDD diagnosis [77].

Degenerative changes of the IVD occur naturally as a part of biological contributions of ageing and genetics, but also as the results of an environmental contribution to disc degeneration and its biomechanical failure.

The IVD works biomechanically to maintain both flexibility and mobility of the spine. It is continuously subjected to bodyweight and muscle activity, only being able to recover and restore its properties during sleep (minimum-loading bearing response). In a normal lumbar IVD, the NP resist to the compressive loads and the AF resist to the tensile stresses. In a DDD situation, the ability to respond mechanically to these loads decreases. This happens because the amount of water retained inside the disc decreases, and consequently, the tensile stresses at the AF's collagen fibers become compressive loads because they stop being activated by the NP [69]. The distinct behaviors of both normal and degenerated IVD under compressive loads are schematically presented in Figure 2.11.

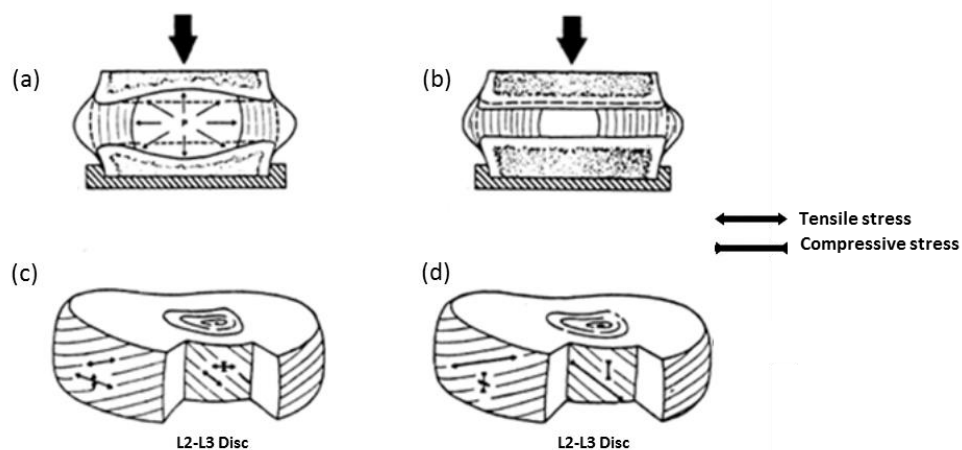


Figure 2.11 - Compression loading of (a) a normal non-degenerated and (b) degenerated disc. (c) Outer annulus layers have a large tension stress along the fibers and also in the tangential peripheral direction. The inner annulus fibers have stresses of smaller magnitude. (d) Annulus fibers show outer layers which are subjected to increased amount of tensile stress. The inner fibers have a high compressive stress (Adapted from [69]).

2.3.2. Solutions for Degenerated Discs

The majority of the adopted treatments to overcome DDD consist of non-invasive approaches. Anti-inflammatory medication, physical therapy and exercise are some of the conservative solutions frequently taken by DDD patients. However, in severe cases, when conservative treatments prove to be ineffective, invasive solutions are applied. Between them, vertebral fusion, intradiscal electrothermal therapy, disc replacement and ozone nucleolysis are the most common approaches [16,78,79].

Vertebral fusion is a solution that consists in joining the two vertebrae which limit the degenerated IVD. This solution aims to reestablish structural integrity, to maintain postural correction after spinal straightening, to prevent progression of an existing deformity, and to decrease back pain. There are several techniques used to perform vertebral fusion. Among them, the posterolateral lumbar interbody fusion, the combined anterior and posterior fusion, the cage devices and minimally invasive techniques are the most applied. Despite the wide range of choices, surgeons and medical doctors have not reach a consensual choice about the best fusion procedure [16].

The intradiscal electrothermal therapy (IDET) is indicated to treat pain originated by radial fissures in the IVDs [67]. This technique requires the insertion of a flexible electrode around the interface between the AF and the NP. When correctly positioned, the electrode deliver heat to the interface, which denervates the painful nociceptors and contracts the AF's collagen fibers, and consequently, the closure of the fissure [78].

Contrarily to spinal fusion, the disc replacement approaches allow the motion between vertebrae to be kept unharmed. Although, as every prosthetic solution, the clinical results of these devices are mainly unknown, as well as their stability in a long-term application or the resistance of the components [80]. There are some contraindications of the use of disc prosthesis, such as facet joint osteoarthritis [78]. However, the offer of disc replacement solutions is very wide, including various designs, materials and customized features developed to enhance its function in the human spine [78].

Finally, ozone nucleolysis therapy is one of the most interesting minimally invasive treatments currently available. It is based on the exploitation of the chemical properties of ozone, an unstable allotropic form of oxygen. A reduction in herniated disc volume is one of the therapeutic aims of

intradiscal administration of ozone, as disc shrinkage may reduce nerve root compression. Another reason for using medical ozone to treat early stages of disc herniation is its analgesic and anti-inflammatory effects [79].

The main solutions for DDD have as principal objective the reduction of the patient's pain. However, from a functional point of view, the use of prosthetic solutions that could reproduce or restore the IVD's mechanical properties are faced as the best approaches as they conserve the physiological role of the degenerated structures. Yet, prosthetic solutions involve higher risks as they imply invasive approaches. Nonetheless, its use is being extensively studied with promising results.

CHAPTER 3

Finite Element Modeling

3.1. Mechanical Modeling

The starting point for this work was the FE modeling, which is here briefly described. The selected FE solver and MS model were extensively described in the work of Castro [44].

The FE solver is a custom tool which is being developed within CT2M (University of Minho), parting from the work of Alves (2010). The first version already included the major hyperelastic laws, viscoelasticity and almost incompressibility effects. At this moment, a novel biphasic poroelastic formulation concerning the multi-physics interactions of the IVD and adjacent structures is also implemented. In addition, the introduction of the osmotic swelling behavior and innovative modeling of AF fibers were also detailed by Castro and Cavalcanti, respectively. Considering all the features of this custom FE solver and its IVD-oriented updates, the CT2M MS FE model is osmo-poro-hyper-visco-elastic with fiber reinforcement [44,81,82].

3.2. Finite Element Model

Parting from the original lumbar spinal FE model developed by Smit [83], Castro developed a partial L3-L4 FE model, containing the L3 and L4 VBs (including both trabecular and cortical bony layers) and the respective IVD (including the three major components, i.e., NP, AF and CEP). After an element-oriented sensibility analysis under uniaxial compression, this model was built with quadratic 27-node hexahedral elements [44].

In 2013, Correia *et al.* used this lumbar MS model to simulate different movements, namely extension-flexion, lateral flexion and axial rotation [84]. Later, this FE model's geometry was simplified by Cavalcanti *et al.* [81], in order to achieve lower simulation times. This version of the CT2M MS FE model was chosen to study the IVD behavior under different loadings and geometric conditions,

because it was simpler than the original model, but still maintained the major geometrical and behavioral characteristics.

At closer inspection, the FE model is built on the 27-node hexahedral mesh and consists on three different materials: the VBs (resulting from transversal cuts of the vertebrae and considered only as cortical bone), the NP and the AF. The removed components are considered to be not relevant for the geometric sensibility analysis. Figure 3.1 depicts a perspective view and a sagittal cut of this FE model.

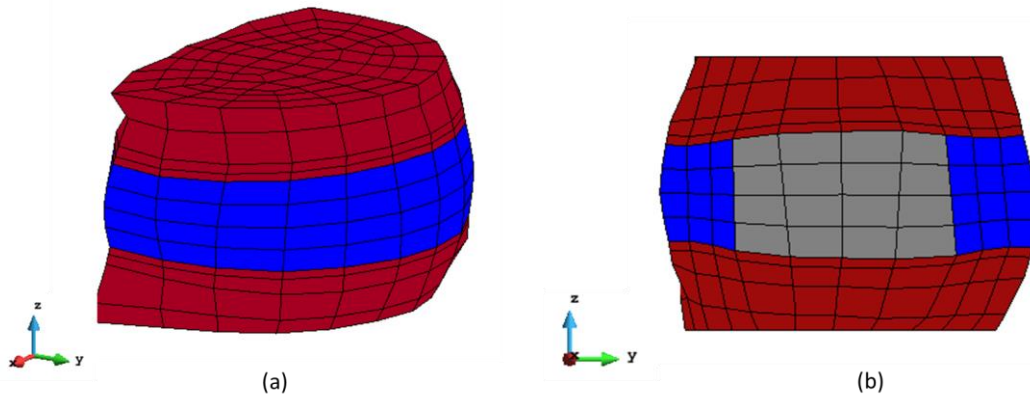


Figure 3.1 - FE mesh: (a) a perspective view; (b) sagittal cut of the FE mesh evidencing the different structures.

The average heights of the full model and the intervertebral disc (IVD) are 28 mm and 11 mm, respectively. Based on the works of Ehlers *et al.*, Iatridis *et al.*, Noailly *et al.*, data fittings were performed to calculate the input values for the material properties [29,85,86]. Tables 3.1 and 3.2 present the material properties of the MS components, and the settings of the AF's fibers. In conjunction with the described geometrical simplification, Correia *et al.* and Cavalcanti *et al.* proposed that the osmo-poroelastic components of the original constitutive modeling were not relevant for the short-term behavior of the IVD, and thus not relevant for the present geometrical sensibility analysis.

Table 3.1 - Material properties of the model components.

		NP	AF	Bone
Isotropy	C_{10} [MPa]	0.0008	0.042	1300
	C_{01} [MPa]	0.0	0.0	300
Anisotropy	\bar{k}	-	300.0	-
	$k_4 = k_6$ [MPa]	-	12.0	-

Viscoelasticity	a_1	1.7	1.2	-
	τ_1 [s]	11.7	0.32	-
	a_2	2.2	1.2	-
	τ_2 [s]	1.1	0.012	-
	a_3	3.0	1.1	-
	τ_3 [s]	0.132	0.0063	-
	a_4	12.0	0.8	-
	τ_4 [s]	0.01	0.0042	-
	a_5	-	0.6	-
	τ_5 [s]	-	0.0031	-

Table 3.2 - Settings of the AF's fibers.

Number of layers	20
Anterior angle	23.2
Posterior angle	46.6
Radial reduction	0.145
Circunferential reduction	0.25

3.3. Geometric Sensibility Study of the FE model

A geometric sensibility study of the model was performed in order to understand the influence of the IVD's geometric characteristics in its dynamic response. The parameters to be analyzed were the wedge angle and average height of the lumbar IVD.

3.3.1. Wedge Angle Variation

The wedge angle is the natural angle of an IVD and it is defined as the angle between both superior and inferior vertebral endplates (VEPs). In the human spine, the different lumbar IVDs have significant angular differences. This approach aims to analyze the influence of the wedge angle on the IVD's

mechanical response to simple movements, such as, extension-flexion (Ex-Fx), lateral flexion (LFx) and axial rotation (AR). Furthermore, the simulation results were used to optimize a three-dimensional multibody (MBS) model of the lumbar spine as described in Chapter 4.

The FE mesh (Figure 3.1) has originally a wedge angle of approximately 2° , corresponding to the L4-L5 motion segment (MS) [87]. The angle variation of the mesh was performed in GiD 11.0.1[®] software. Different rotations were applied to a selection of nodes, and MSs with -2° , 0° , 5° , 7° , 11° and 20° (besides the original 2°) were obtained. These angular values were selected based on the work of Matos, in which radiographs and magnetic resonance images were used to measure the different IVD angles [87]. In figure 3.2 a sagittal cut of each FE model is presented.

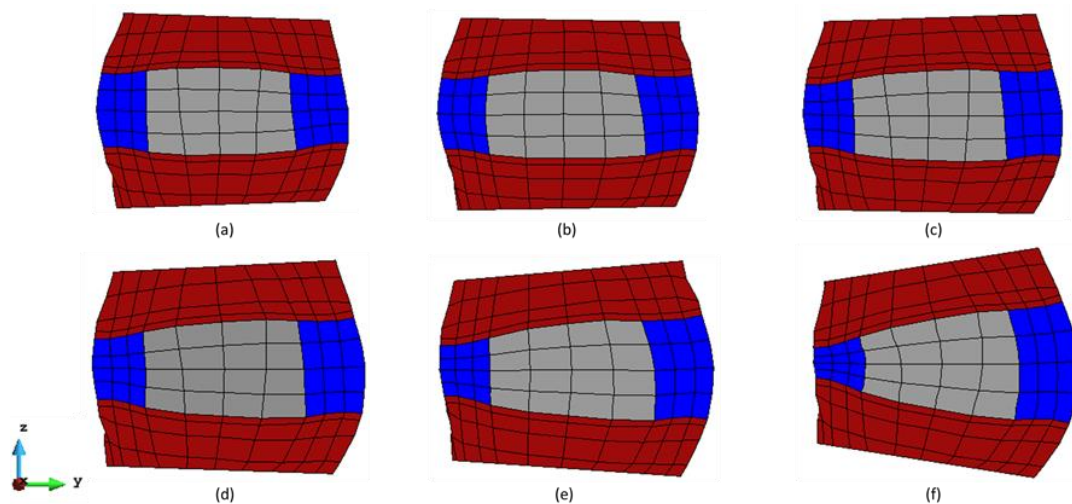


Figure 3.2 - Sagittal cut of the FE model with: (a) -2° ; (b) 0° ; (c) 5° ; (d) 7° ; (e) 11° ; and (f) 20° .

3.3.2. Average Height Variation

The height of an IVD varies among different individuals and different lumbar levels. In addition, during their whole life, individuals tend to lose IVD height as a results of the degeneration of its structures [44]. Thus, the analysis of the IVD's average height variation can be faced as a helpful approach to comprehend its biomechanical behavior when these geometric changes occur.

As mentioned before, the original average disc height is 11 mm. The variation of IVD's height was performed in GiD 11.0.1[®] software, by applying a scale factor in ZZ axis to the FE mesh. In Table 3.3 are presented the applied scale factors and the obtained IVD heights.

Table 3.3 - Inputted scale factors and resulting IVD heights.

Scale Factor	Disc Height (mm)
0	11
0.909	10
0.818	9
0.727	8
0.636	7

3.3.3. Simulation Settings

The analysis of the IVD's biomechanical response was made with a single simulation setup, in order to maintain the coherence between the models. Therefore, the FE mesh is the only variable input on the two aforementioned approaches. All simulations were comprised in two temporal stages: (i) a pre-conditioning period, concerning a volume increase of the IVD (from 0 to 10 s), and (ii) pure moment application around each axis (from 10 to 12 s). During simulation, the inferior vertebra was fixed.

For healthy IVDs, the regulatory internal pressure of the nucleus pulposus (NP) is approximately 0.2 Mpa [44], corresponding to the average native osmotic swelling pressure. To reach this value, a volume increase of both NP and AF was implemented, mimicking the native free osmotic swelling behavior (which is not under use in this model) of the disc. Castro reported that during free swelling periods, the NP and AF's volumes increase with a ratio of 3:1, respectively [44]. Therefore, a volume increase of 12% for the NP and 4% for the AF was implemented for the first 10 seconds of simulation, corresponding to the pre-conditioning period. After this stage, an incremental pure moment was applied in the superior vertebra. The maximum moment applied was 10 Nm, which, from preliminary studies was judged to be sufficient to produce physiologic motions, but small enough to not injure the spine [88]. The axes of rotation were selected depending on the physiological movement intended for simulation, namely extension-flexion, lateral flexion and axial rotation. In Figures 3.3 and 3.4 are depicted the loading profiles.

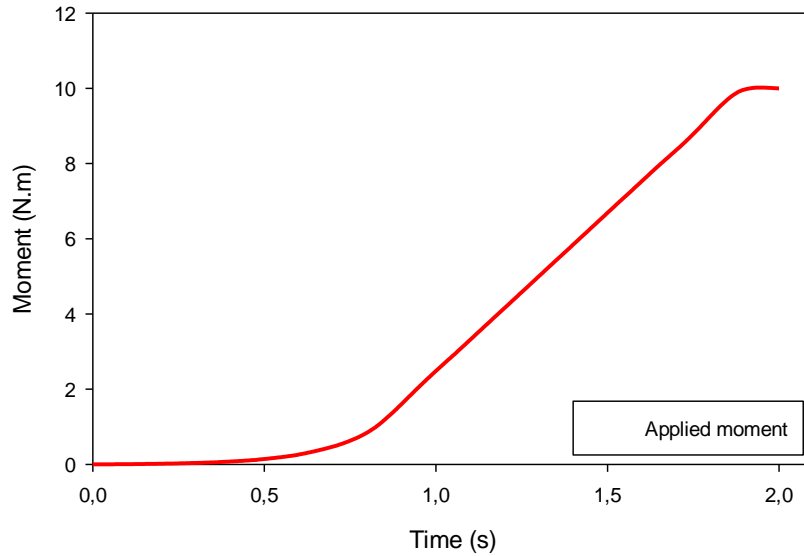


Figure 3.3 - Loading profile of the applied moment.

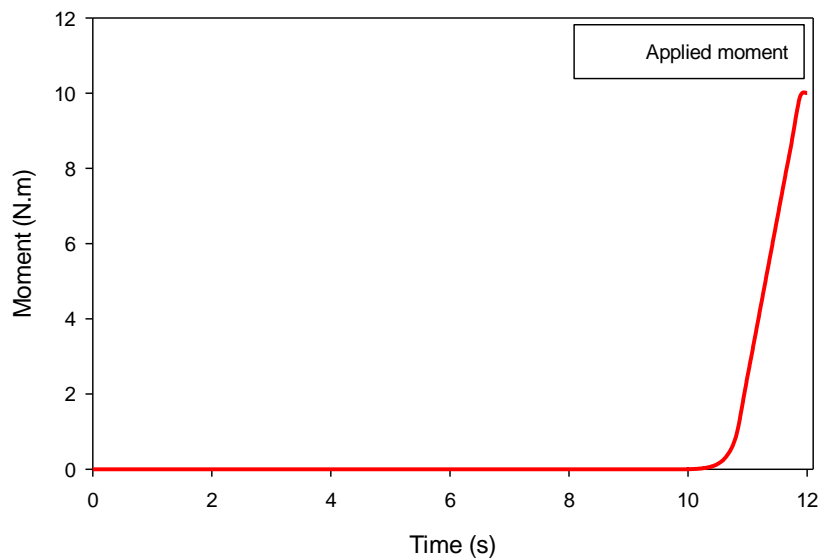


Figure 3.4 - Loading profile of the whole simulation.

It is relevant to mention that the depicted loading ramp (Figure 3.3) induces flexion, right lateral flexion and counter clockwise axial rotation (depending on the axes of rotation). For the opposite movements (extension, left lateral flexion and clockwise axial rotation) the equivalent negative loading ramp was used.

3.3.4. Simulation Results

The analyzed simulation results concerned the disc's volume and pressure variations, angular displacements and AF's fibers stretch. The results are displayed by categories, depending on the simulated movement.

3.3.4.1. Wedge Angle Variation

- Extension-Flexion (Ex-Fx)

The influence of the IVD's wedge angle is analyzed by simulating several IVD models with angular differences. In Figures 3.5 and 3.6 are presented the NP pressure variation during extension and flexion, respectively. On both graphs, it is possible to observe a gradual pressure increase during the pre-conditioning period. At the end of that period ($t=10$ s), NP pressure reaches a value of approximately 0.2 MPa, corresponding to the normal values of NP osmotic pressure [44]. The loading period (from 10 to 12 s) is characterized by an exponential increase of the NP pressure. The different models present similar behavior during extension. However, during flexion, the models with higher wedge angles presented higher pressure values at the end of the loading period.

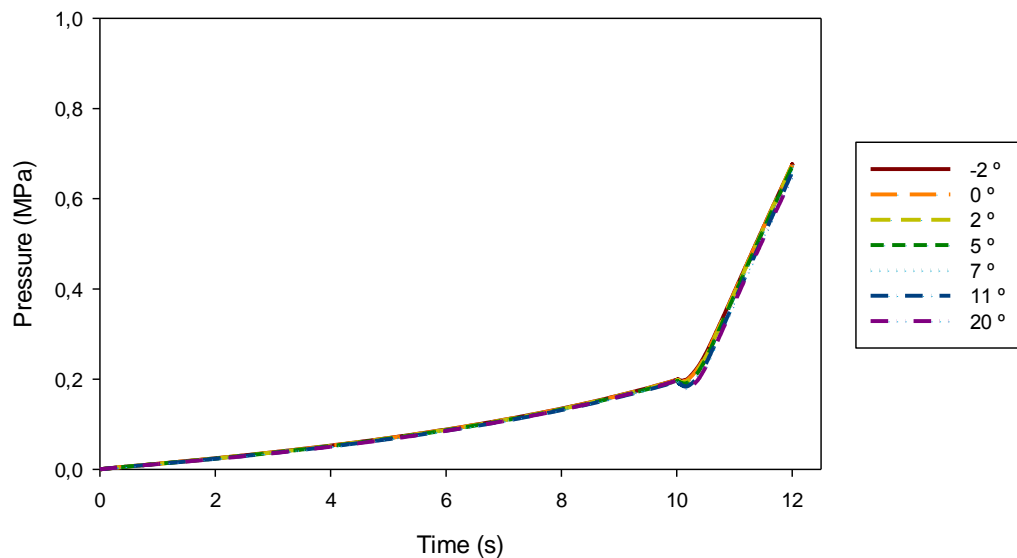


Figure 3.5 - NP pressure variation during extension.

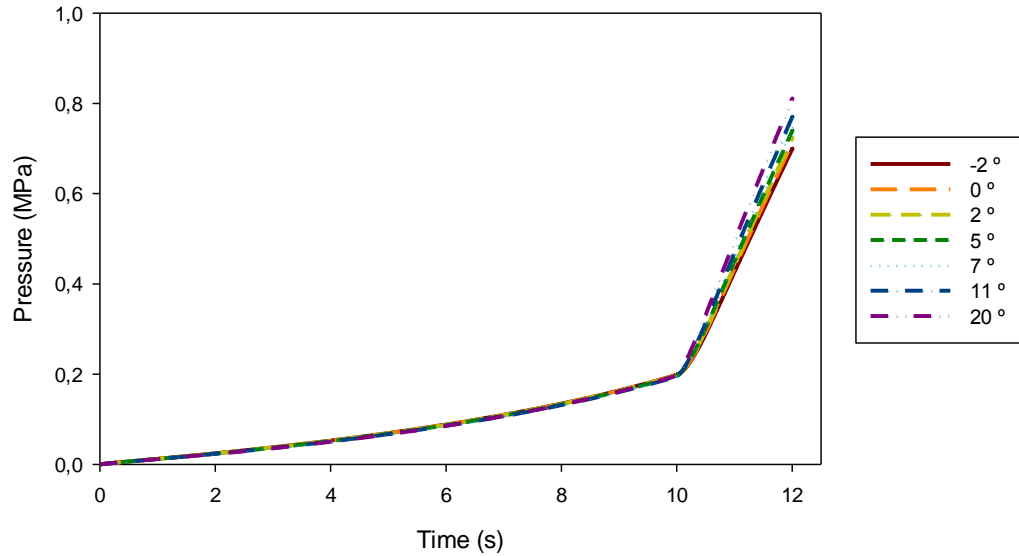


Figure 3.6 - NP pressure variation during flexion.

The AF pressure variation results during extension and flexion are depicted in Figures 3.7 and 3.8, respectively. Similarly to the NP, the AF pressure values increase gradually during the pre-conditioning period and exponentially during the loading period. The first period corresponds to the implemented volume increase, where all IVD models revealed similar behavior. The exponential pressure increase concerns the applied moment. However, significant changes are observed in the loading period on both graphs. During extension, IVD models with higher wedge angles present higher AF pressure values, while during flexion, IVD models with higher wedge angles revealed lower AF pressure values.

The signal difference between the pressure values of NP and AF mean that compressive forces are acting on the NP, while tensile forces are acting on the AF.

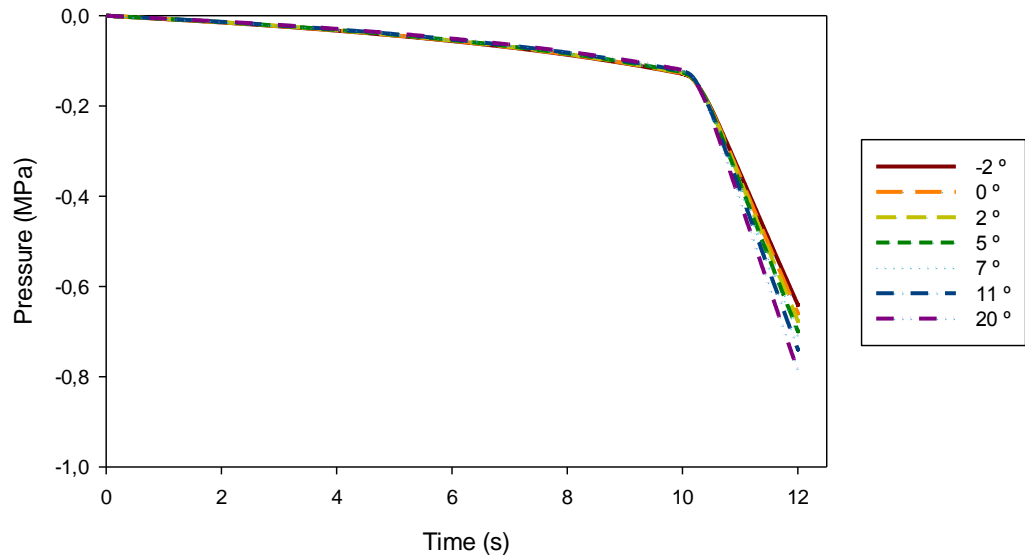


Figure 3.7 - AF pressure variation during extension.

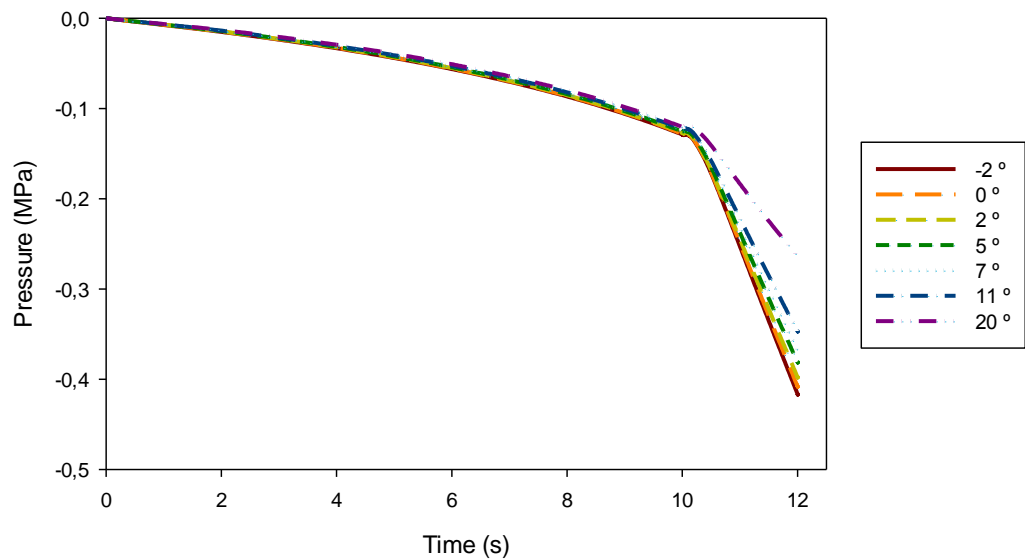


Figure 3.8 - AF pressure variation during flexion.

The volume variation results of both NP and AF during extension and flexion (Figures 3.9 and 3.10) proves that the implemented volume increase during the pre-conditioning period was applied. Hence, all different IVD models present a volume increase of approximately 12% and 4% in the NP and AF, respectively. However, during the loading period, it is possible to observe a decrease in the NP's volume as the volume of the AF increases. According to Castro, this happens due to the fact that under loading conditions, the pressure migrates from the NP to the surrounding structures. In detail, there is a radial flow occurring from the NP into the inner layers of the AF [44]. During extension, these volume variations between NP and AF are more evident than in flexion. In addition, IVD models with

higher wedge angles present higher fluid exchanges between the NP and the AF during extension. In flexion, all IVD models have similar behavior.

In detail, under loading conditions, the pressure transfers from the NP to the surrounding structures, i.e., a radial flow occurs from the NP into the inner layers of the AF and a vertical flow is noticed from the NP into the CEPs.

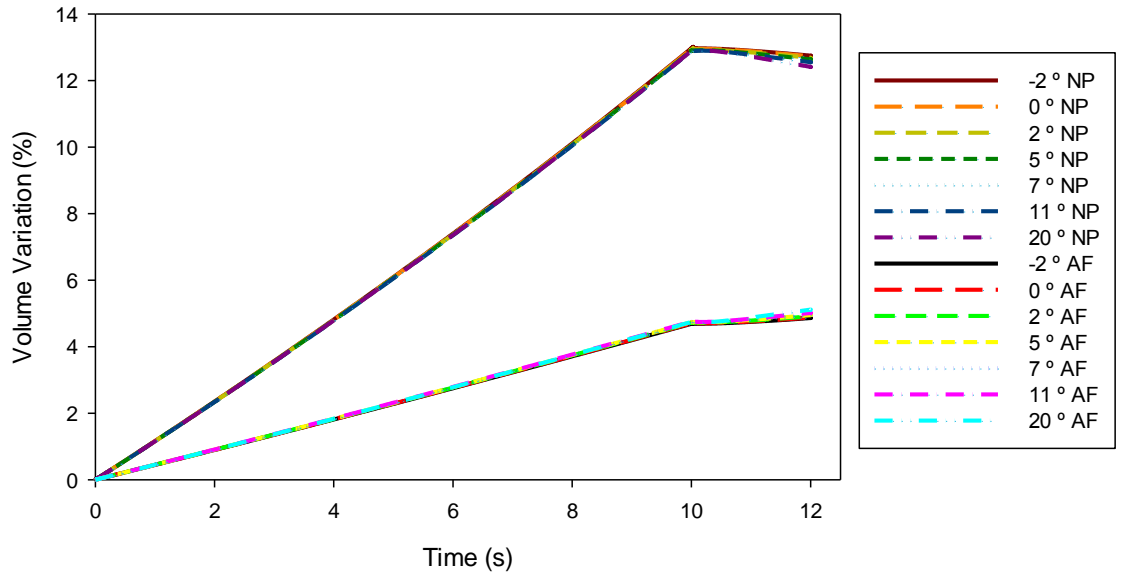


Figure 3.9 - NP and AF volume variation during extension.

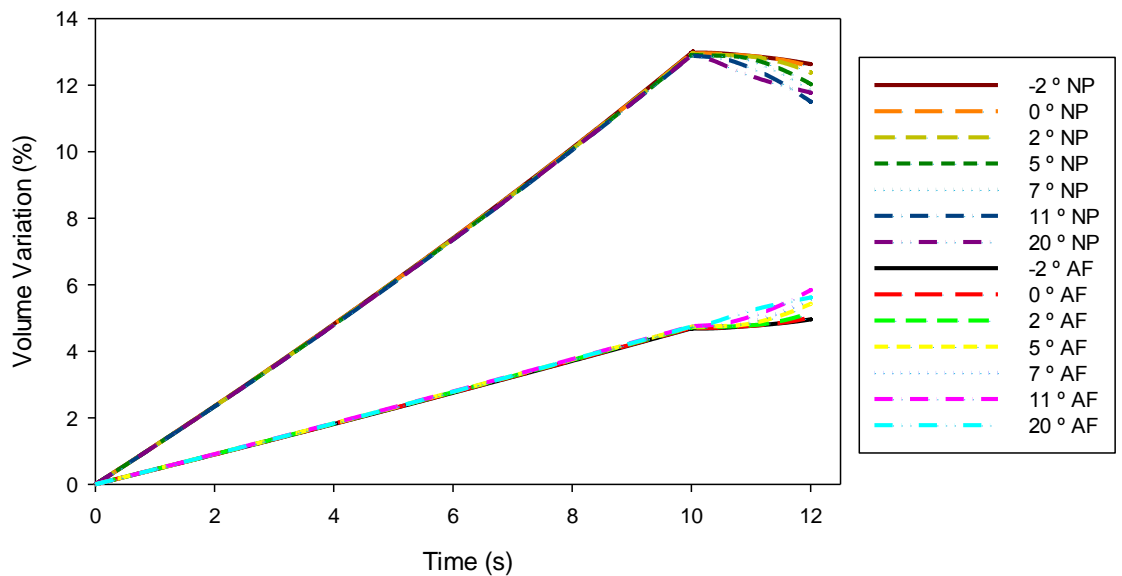


Figure 3.10 - NP and AF volume variation during flexion.

The AF's fibers stretch during extension and flexion is presented in Figures 3.11 and 3.12, respectively. Two key time points of the simulation were selected: (a) 10 s, corresponding to the end of the pre-conditioning period; and (b) 12 s, corresponding to the end of the loading period. As

evidenced in Figures 3.11(a) and 3.12(a), at $t=10$ s, the majority of the AF fibers (about 90%) is under tension. However, during extension (Figure 3.11(b)), there is a decrease of the number of tensioned fibers (about 80%) but the grade of tension increases. Consequently, the number and grade of compressed fibers increases. On the other hand, during flexion (Figure 3.12(b)) the number of compressed fibers decreased about 4%, while the number and grade of tensioned fibers has increased. The different IVD models have similar behavior on both extension and flexion.

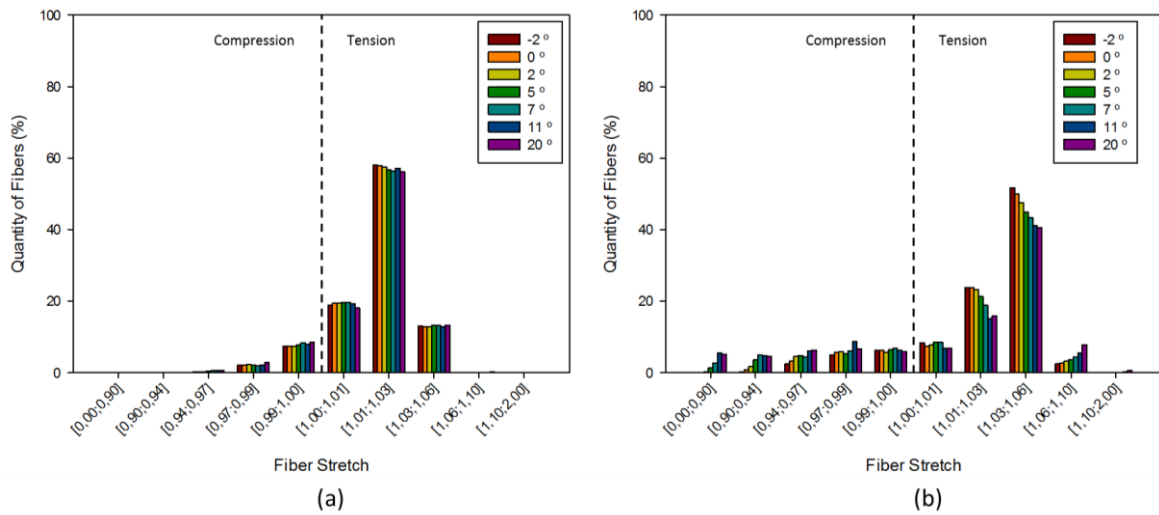


Figure 3.11 - AF fiber stretch during extension: (a) at 10s - end of pre-conditioning period; (b) 12s - end of loading period.

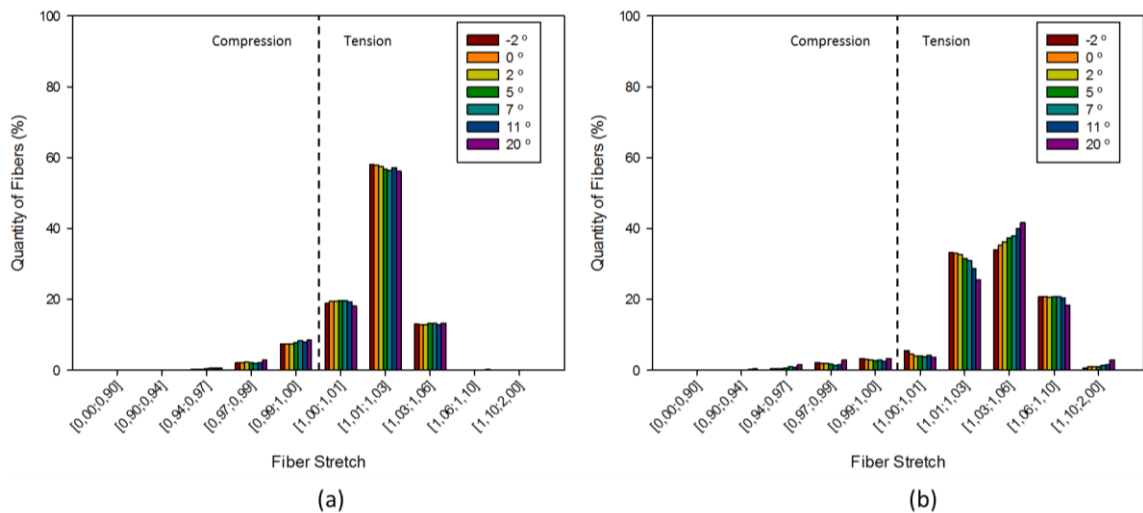


Figure 3.12 - AF fiber stretch during flexion: (a) at 10s - end of pre-conditioning period; (b) 12s - end of loading period.

The angular range of movement of the different IVDs is displayed in Figure 3.13. In all cases, the range of motion is larger in extension than in flexion. However, IVD models with higher wedge angle present higher extension range and lower flexion range.

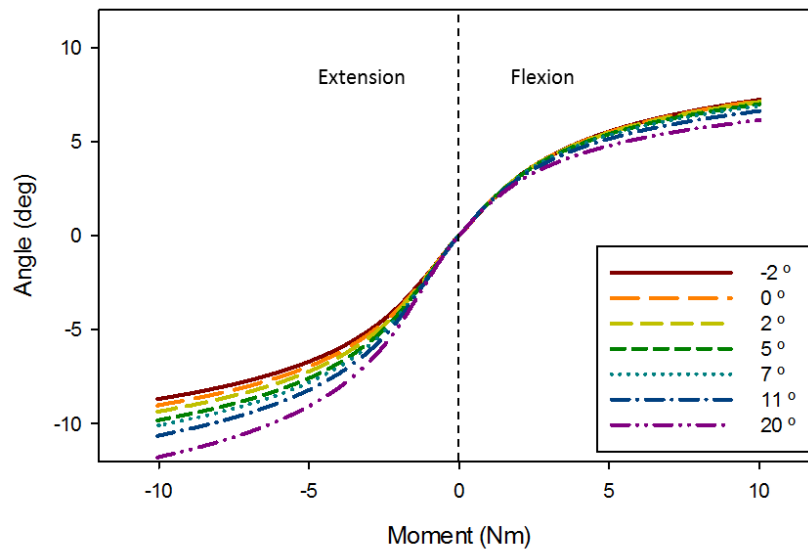


Figure 3.13 - Angular range of extension-flexion movement.

- Lateral Flexion (LFx)

The IVD FE models are symmetrical on the sagittal plane, therefore, the simulation results are equivalent to both left and right lateral flexion. Hence, only right lateral flexion results are presented.

Similarly to Ex-Fx, both NP and AF pressure results (Figures 3.14 and 3.15) present an expected mild increase during the pre-conditioning period (corresponding to the defined volume increase), and an exponential increase during the loading period. Slight changes can be noticed between different models, more specifically, IVDs with lower wedge angles present higher pressure values.

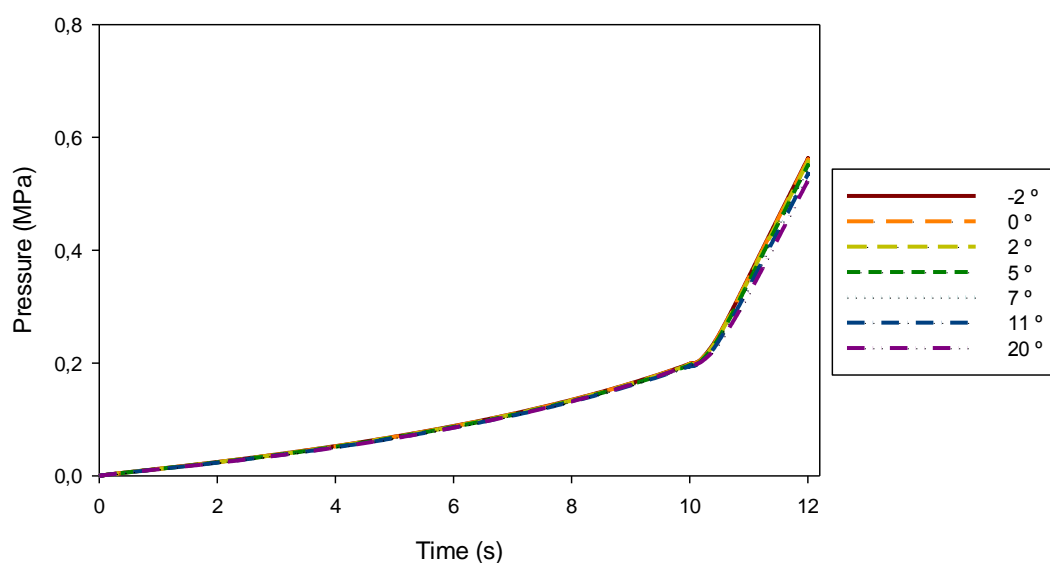


Figure 3.14 - NP pressure variation during lateral flexion.

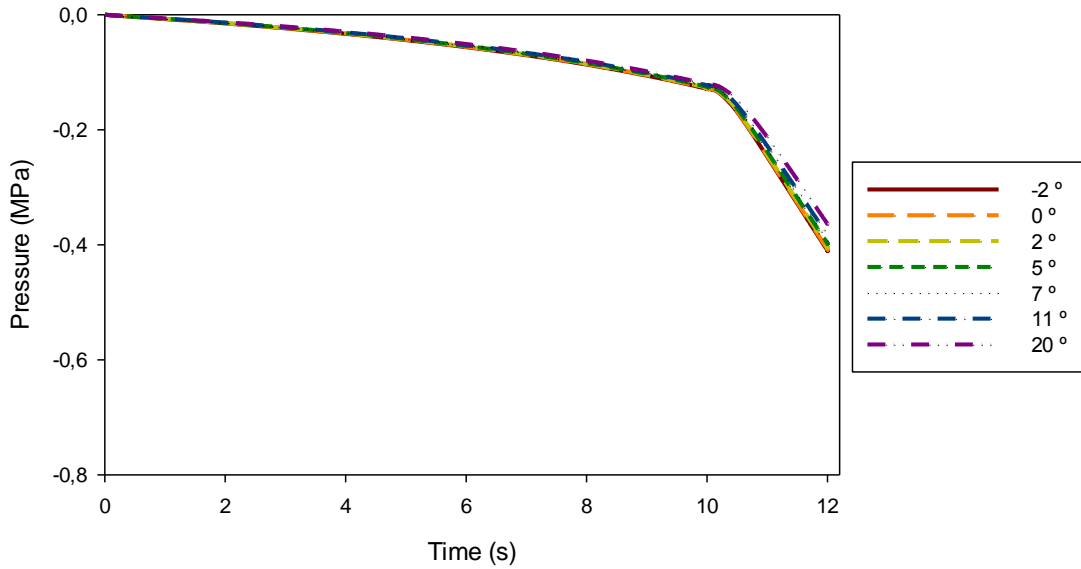


Figure 3.15 - AF pressure variation during lateral flexion.

The volume variation results are showed in Figure 3.16, and present similar behavior to equivalent results in Ex-Fx, with a defined volume increase for both NP and AF during the first period. The loading period implies an increase of the AF's volume, while the volume of the NP decreases. Similarly to Ex-Fx the IVDs with higher wedge angels imply higher fluid exchange between the NP and AF.

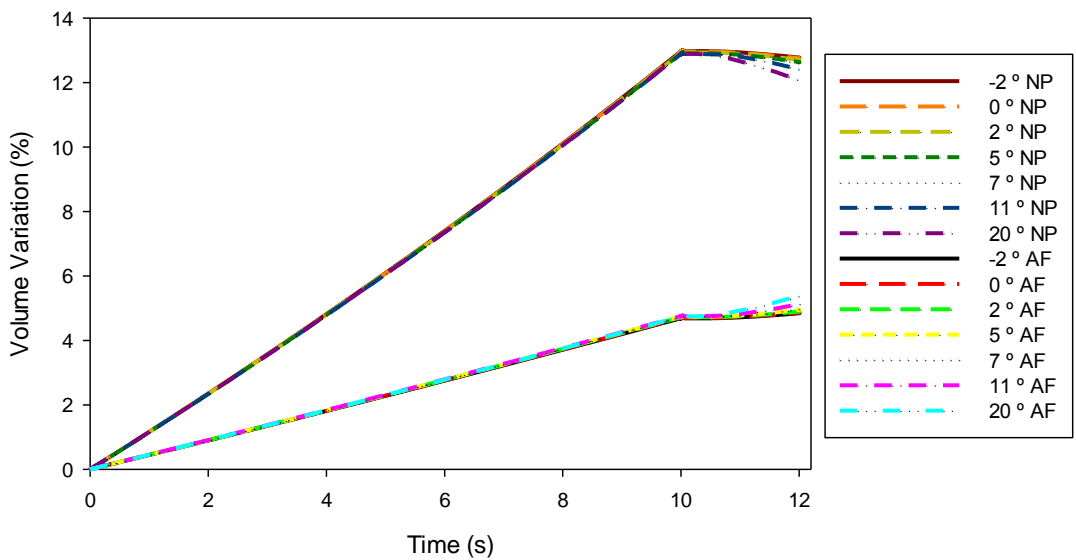


Figure 3.16 - NP and AF volume variation during lateral flexion.

Identically to extension movement, the AF fiber stretching during LFx (Figure 3.17) leads not only to an increase of the number and grade of compressed fibers, but also to an increase of the stretching grade of the tensioned fibers.

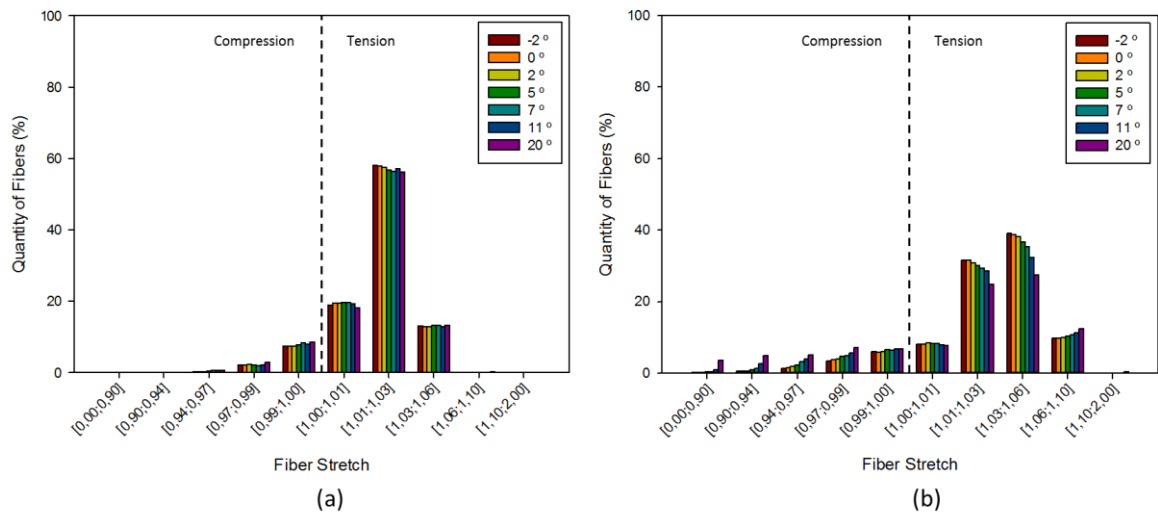


Figure 3.17 - AF fiber stretch during lateral flexion: (a) at 10s - end of pre-conditioning period; (b) at 12s - end of loading period.

IVD models with lower wedge angles present higher range of motion in lateral flexion, as evidenced in Figure 3.18.

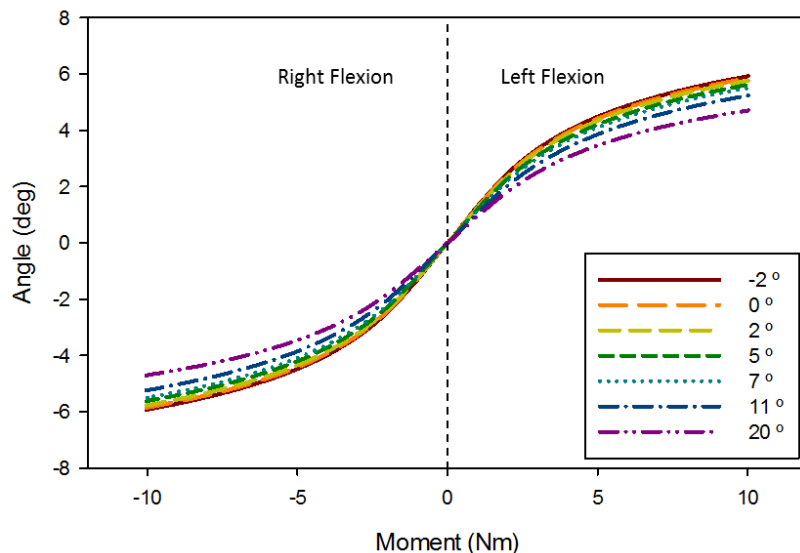


Figure 3.18 - Angular range of bilateral flexion movement.

- Axial Rotation (AR)

Equivalently to LFx, both clockwise and counterclockwise axial rotations present the same behavior. Hence, only axial rotation in the counterclockwise direction results are presented.

The NP and AF pressure variation (Figures 3.19 and 3.20) follows the same behavior of both Ex-Fx and LFx movements. In the first period the pressure increases gradually (until 0.2 Mpa in the NP), but in the second period (loading period), due to the lack of compressive forces, the pressure increase is not as pronounced as in the case of Ex-Fx or LFx. All different IVD models present similar behavior.

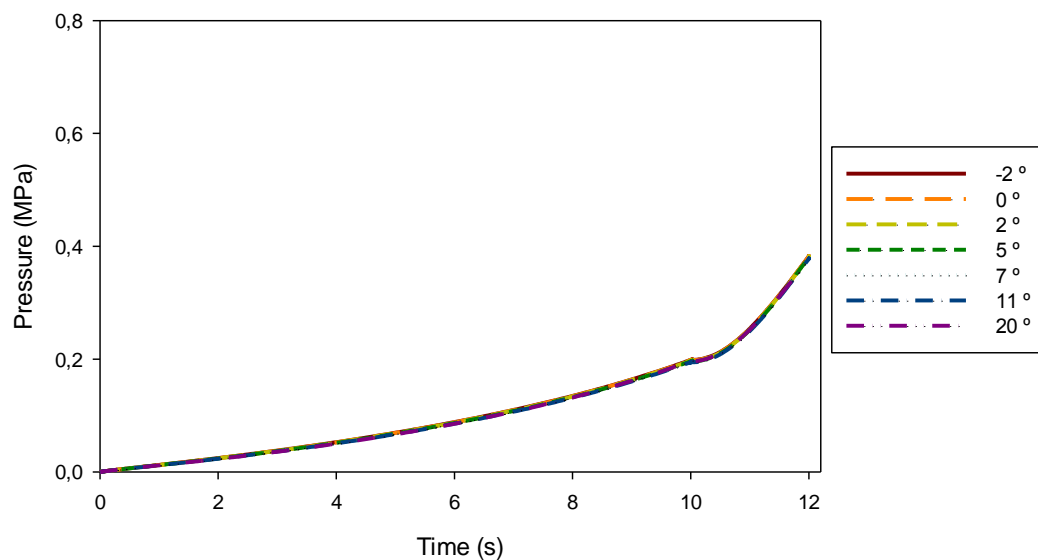


Figure 3.19 - NP pressure variation during axial rotation.

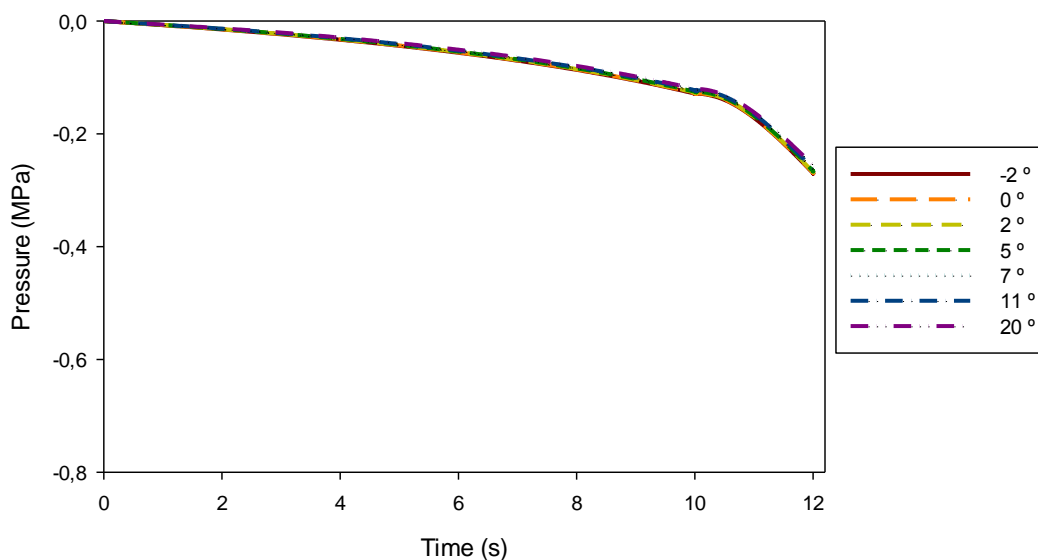


Figure 3.20 - AF pressure variation during axial rotation.

As shown in Figure 3.21, both NP and AF volume variations present the same behavior that Ex-Fx and LFx movements in the pre-conditioning period. Nonetheless, during the loading period, the previously mentioned decrease of the NP's volume and increase of the AF's volume is almost imperceptible. Once again, this happens due to the lack of compressive forces that contribute to the pressure radial flow from the NP to the inner layers of the AF [44]. Once again, the wedge angle revealed no influence in the behavior of the IVD under axial rotation.

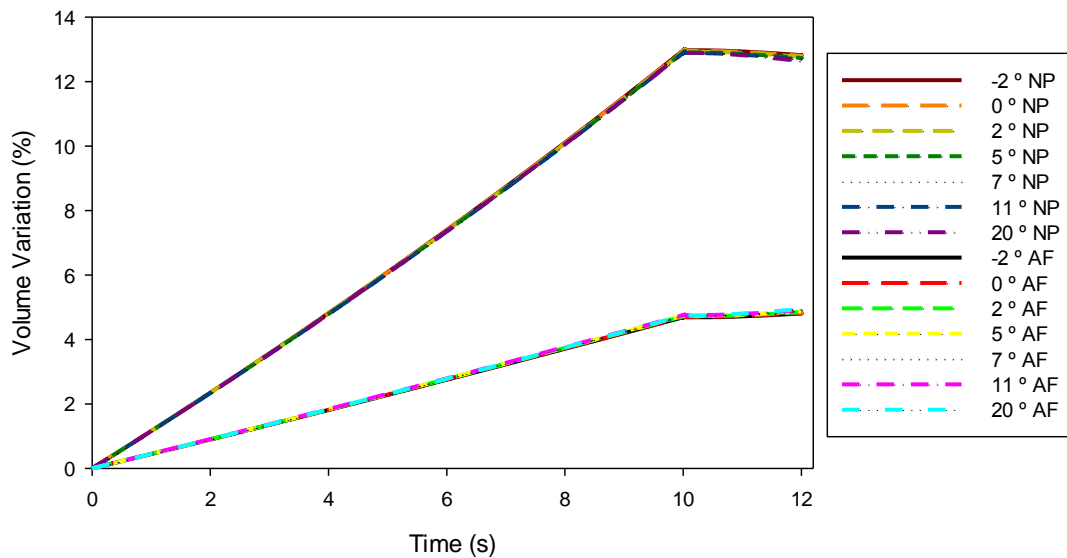


Figure 3.21 - NP and AF volume variation during axial rotation.

Similarly to Ex-Fx and LFx, the AF fibers stretching conditions at the end of the pre-conditioning period ($t=10s$) implies around 90% of the fibers in tension. Yet, during axial rotation, the stretch grade of the tensioned fibers increased, but the number of fibers in compression increased significantly, reaching approximately 30% of the AF fibers. By comparing the fiber stretch results with Ex-Fx and LFx, it is under axial rotation that the number of AF fibers under compression is higher. As highlighted in Figure 3.22, all IVDs showed identical behavior.

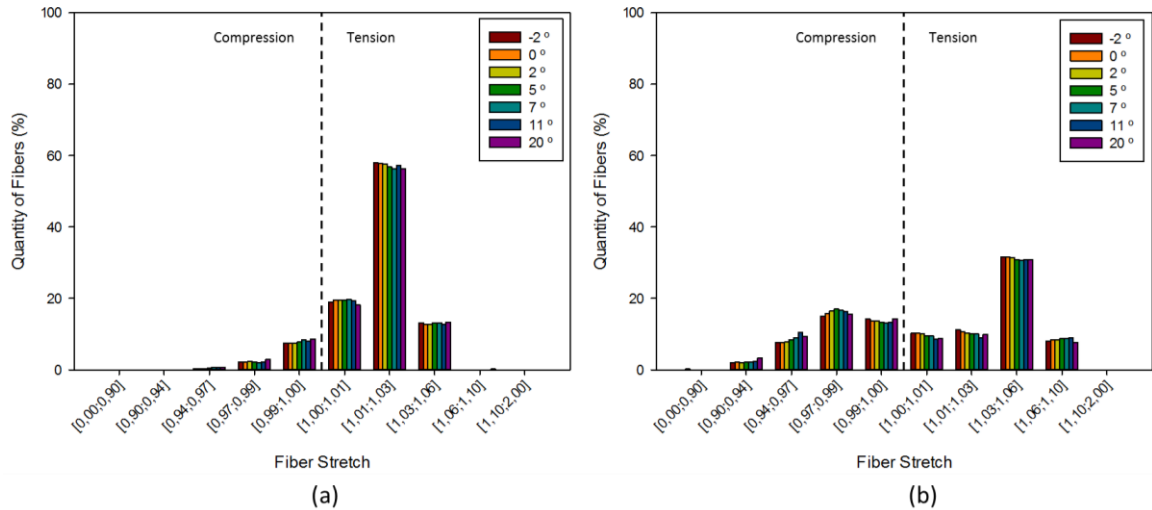


Figure 3.22 - AF fiber stretch during axial rotation: (a) at 10s - end of pre-conditioning period; (b) at 12s - end of loading period.

Consistently with LFx, axial rotation reveals symmetric behavior for both clockwise and counterclockwise rotation. The angle range during AR (Figure 3.34) is significantly smaller when compared with Ex-Fx and LFx movements. In addition, the angle range of all IVD models is similar contrarily to Ex-Fx and LFx.

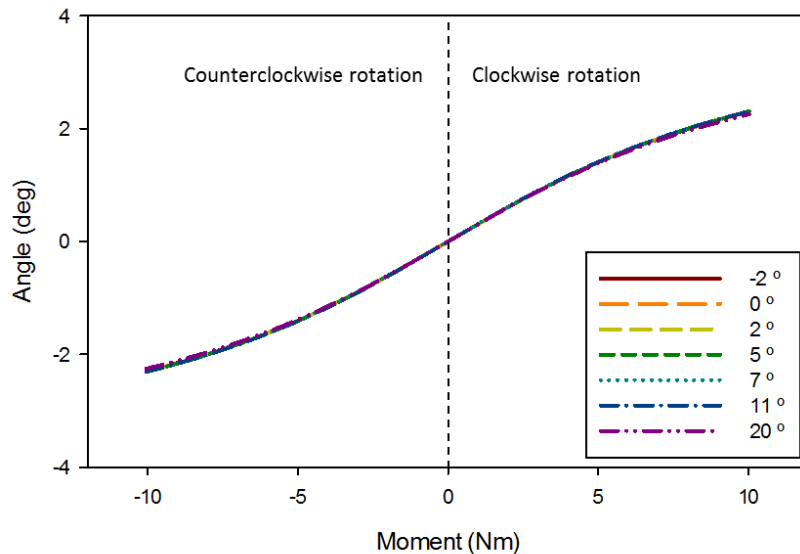


Figure 3.23 - Angular range of axial rotation movement.

In summary, all models with different wedge angle behaved similarly under loading, showing no significant differences in what concerns pressure and volume variation, and AF fiber stretching. However, it can be noticed that the variation of the disc's angle influence significantly its range of motion during Ex-Fx and LFx.

3.3.4.1. Average Height Variation

- Extension-Flexion (Ex-Fx)

The biomechanical response analysis of the IVD models with different height under loadings, contributes to study both the influence of disc height at different lumbar levels, and the height loss due to degeneration situations or normal ageing.

The NP pressure variation during Ex-Fx is presented in Figures 3.24 and 3.25. As expected, a pressure increase is noticed during the pre-conditioning period, reaching 0.2 Mpa at $t=10$ s on both extension and flexion. However, during the loading period on extension, thicker IVD models present slightly higher pressure values. Nevertheless, in flexion all models present the same behavior, reaching higher pressure values than in extension.

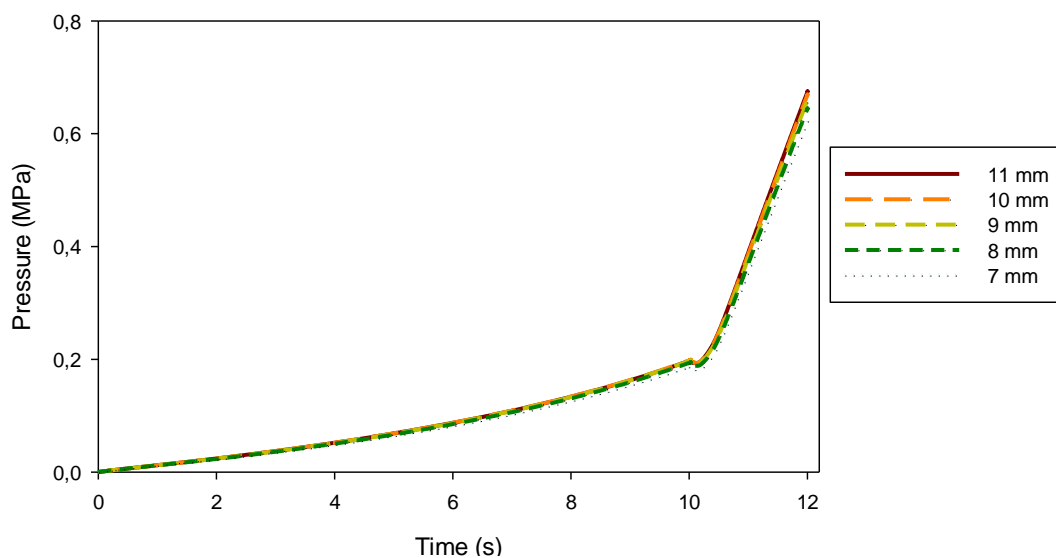


Figure 3.24 - NP pressure variation during extension.

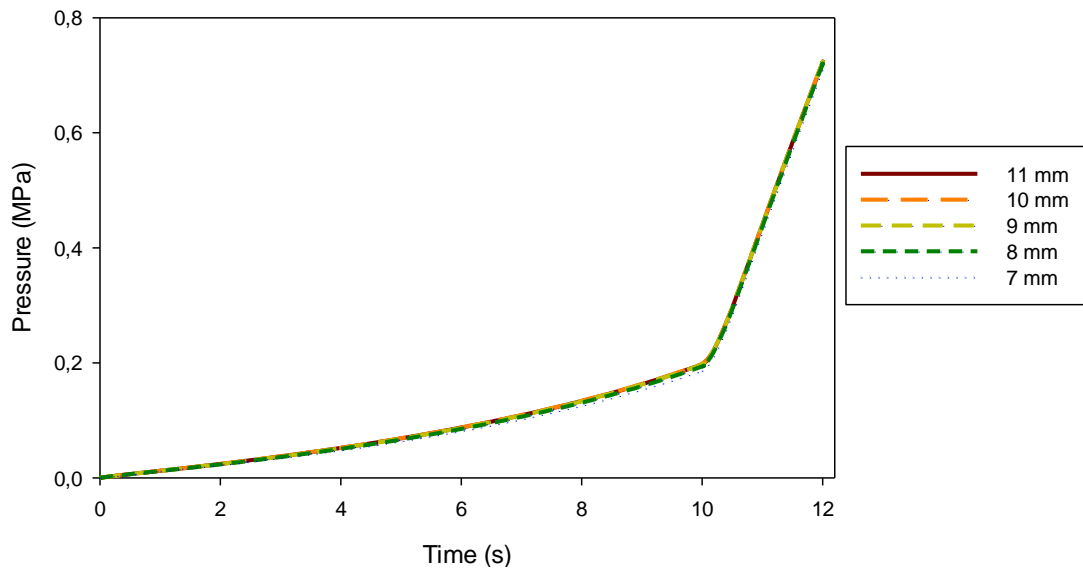


Figure 3.25 - NP pressure variation during flexion.

When the AF pressure varies (Figures 3.26 and 3.27), either graphs present the same behavior during the first period with the pressure increasing due to a defined volume increase. Yet, in the loading period, contrarily to NP pressure, the extension movement present similar behavior for all models and the pressure values are higher than in flexion. In addition, during flexion the thicker IVD models present slightly higher values of AF pressure.

As aforementioned, the values of NP and AF pressure present opposite signal due to the fact that the NP responds to compressive forces and the AF responds to tensile forces.

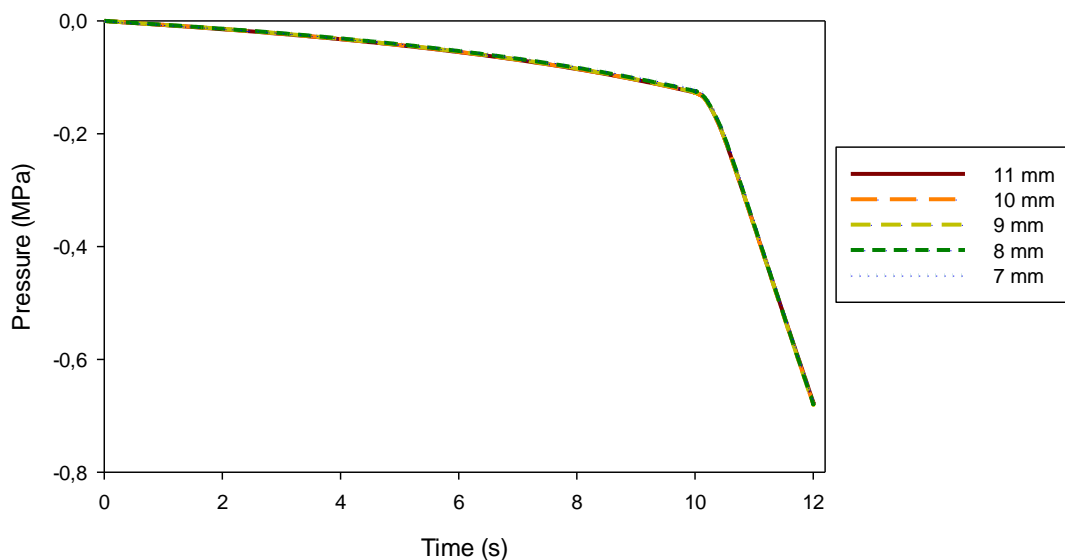


Figure 3.26 - AF pressure variation during extension.

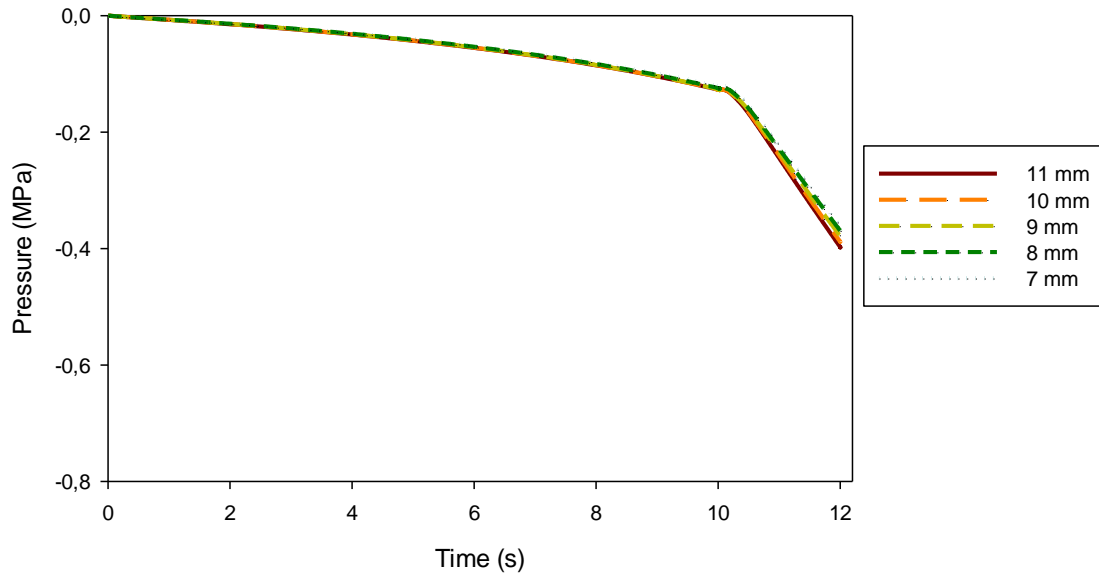


Figure 3.27 - AF pressure variation during flexion.

Pre-defined volume increases of 12% to NP and 4% to AF are observed during the pre-conditioning periods of both extension and flexion (Figures 3.28 and 3.29). Moreover, during loading periods in Ex-Fx, the NP volume has a slight decrease while the AF volume increases. As mentioned before, the reason for these variations is due to the radial flow from the NP to the AF when the disc is under loading [84]. However, this variation is more noticeable during extension, and thinner IVD models present a higher fluid exchange.

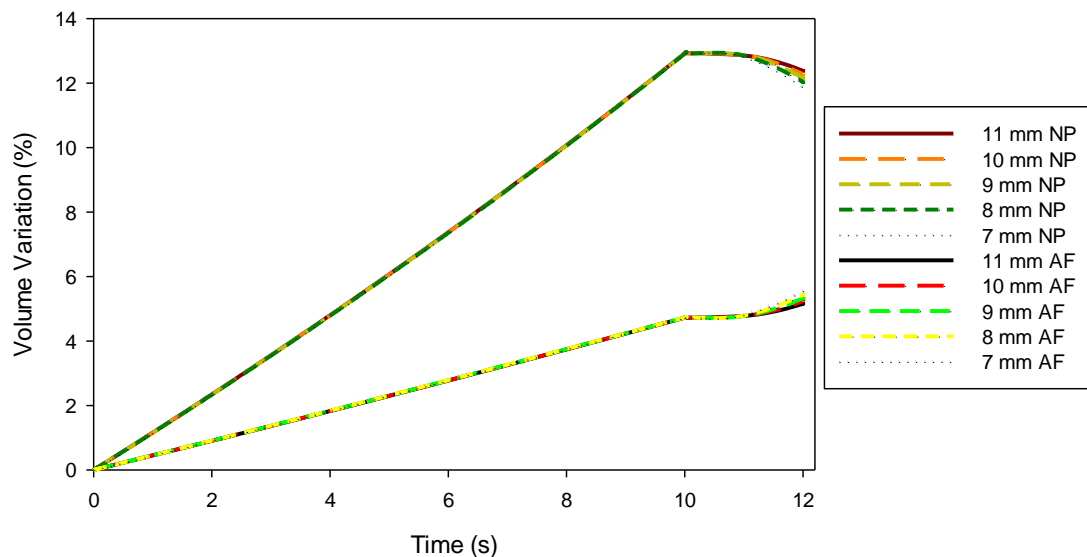


Figure 3.28 - NP and AF volume variation during extension.

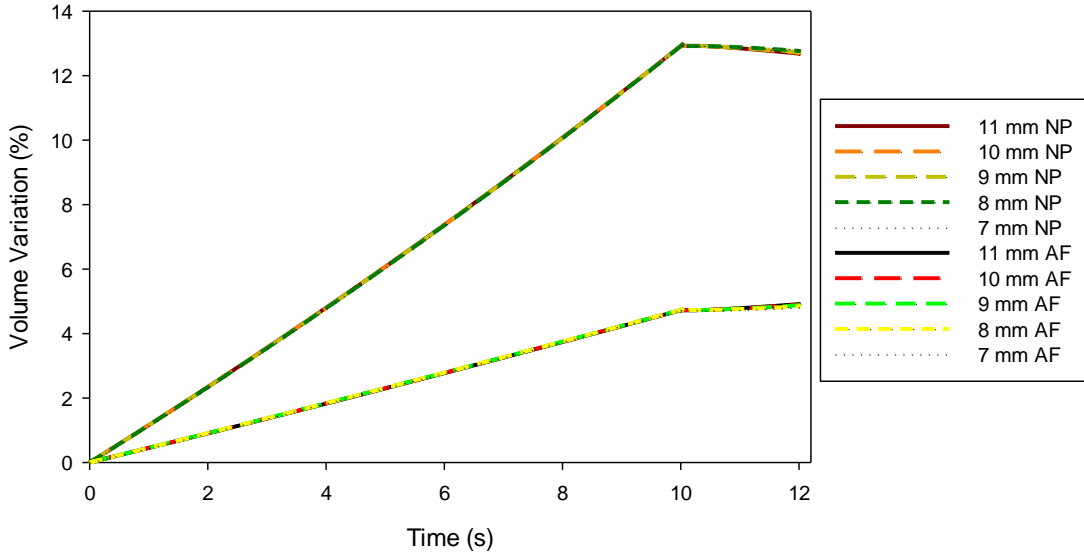


Figure 3.29 - NP and AF volume variation during flexion.

The AF fibers stretch in extension and flexion are depicted in Figures 3.30 and 3.31. As expected, in both cases, at the end of the pre-conditioning period ($t=10s$), approximately 90% of all AF fibers are under tension. Nonetheless, during extension, the number of compressed fibers increased significantly (from 10% to 20%). Despite the decrease on the number of tensioned fibers, the grade of stretch increased during extension. In flexion, the opposite is observed, with the number and grade of tensioned fibers increasing. In general, on both extension and flexion, the different IVDs showed similar behavior.

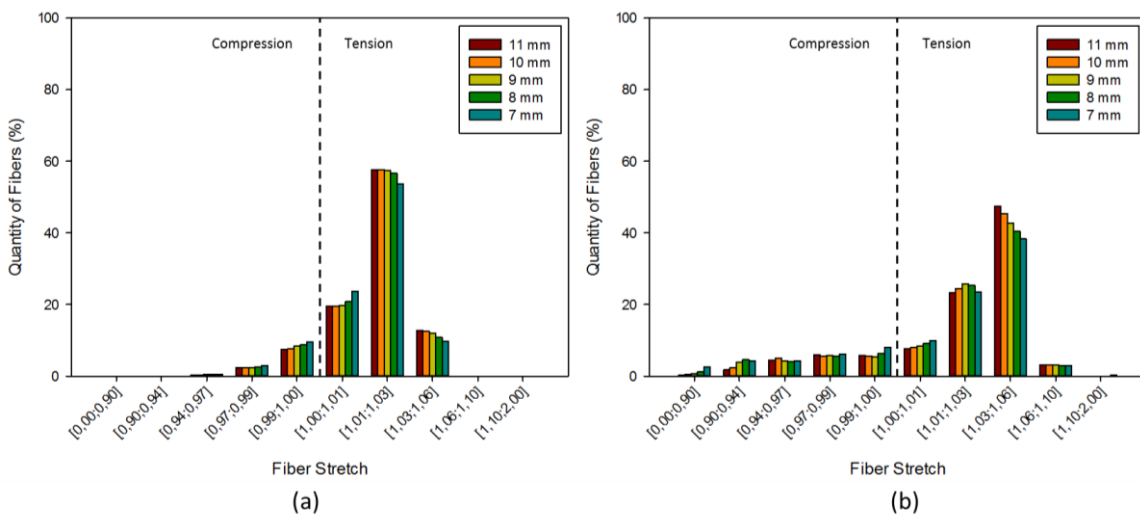


Figure 3.30 - AF fiber stretch during extension: (a) at 10s - end of pre-conditioning period; (b) at 12s - end of loading period.

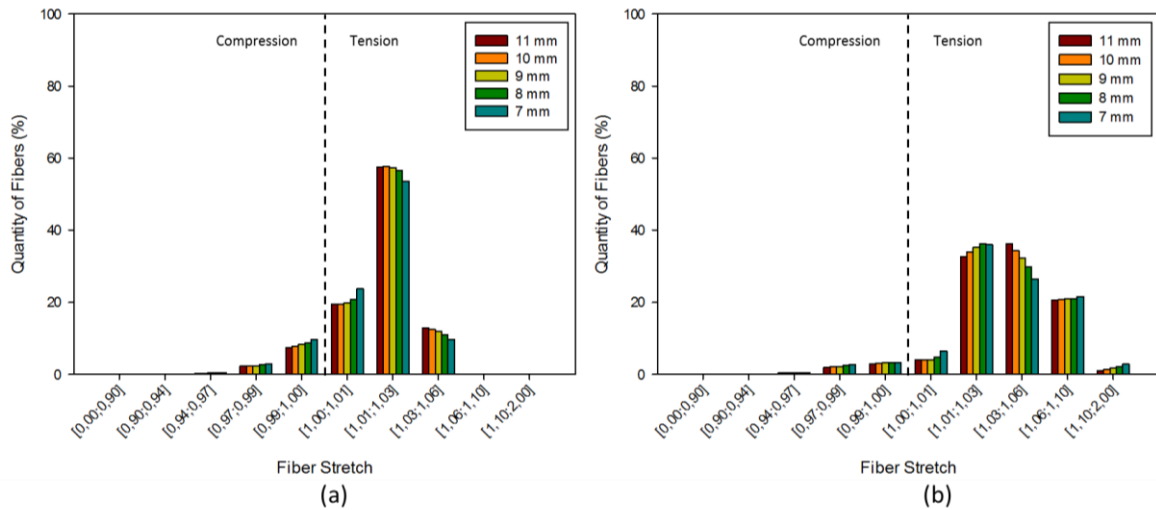


Figure 3.31 - AF fiber stretch during flexion: (a) at 10s - end of pre-conditioning period; (b) at 12s - end of loading period.

The range of motion for Ex-Fx is displayed in Figure 3.32, where it is possible to observe that for all cases, extension has a higher range than flexion. Yet, thicker IVD models present higher ranges of angular movement.

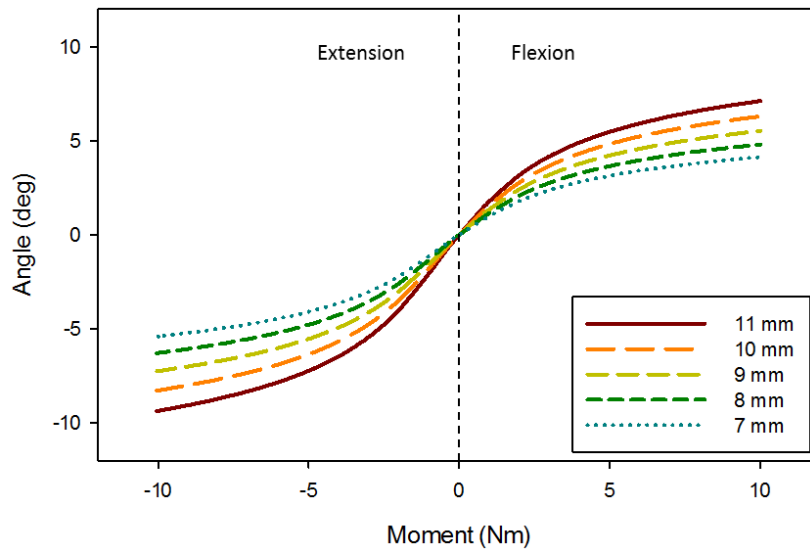


Figure 3.32 - Angular range of extension-flexion movement.

- Lateral Flexion (LFx)

During LFx, both NP and AF pressure variation (Figures 3.33 and 3.34) presented an expected behavior, similar to Ex-Fx. Firstly a gradual increase of pressure is noticed until t=10s. Then, the

pressure increase is more sharp, reaching higher values in the NP. However, the pressure values are lower comparing to those observed for during Ex-Fx. Nonetheless, no significant differences were observed in the behavior of the different IVDs.

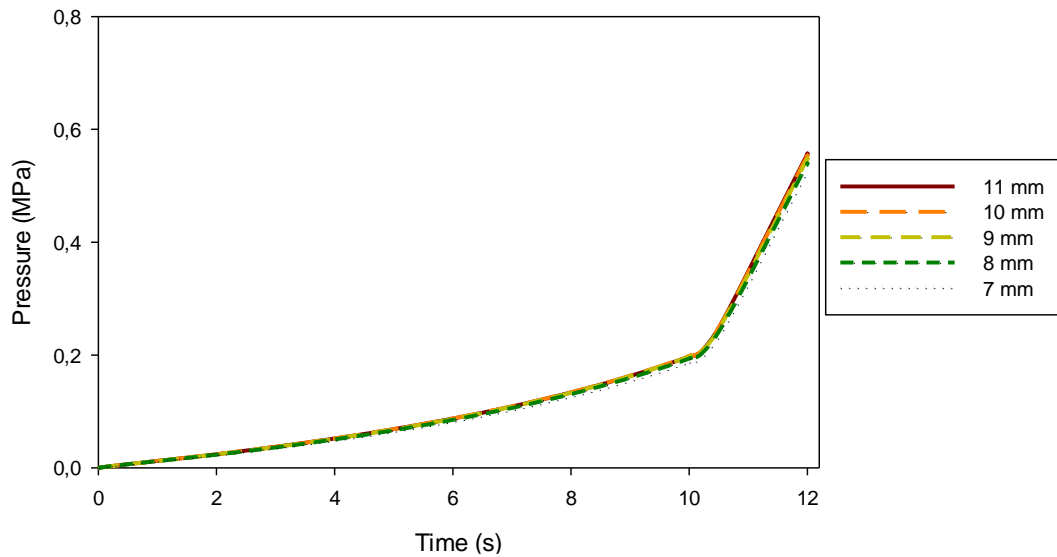


Figure 3.33 - NP pressure variation during lateral flexion.

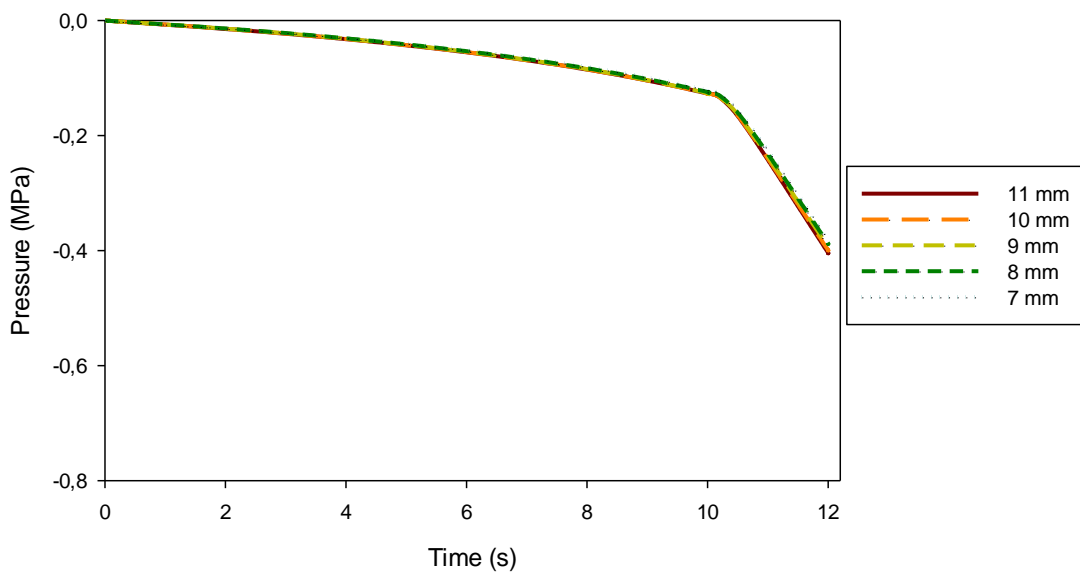


Figure 3.34 - AF pressure variation during lateral flexion.

Identically to Ex-Fx, the volume variation during LFx (Figure 3.35) shows the predefined volume increase in the first period, and the flow from the NP to the AF in the loading period. In LFx the height differences showed no influence on the IVD's behavior.

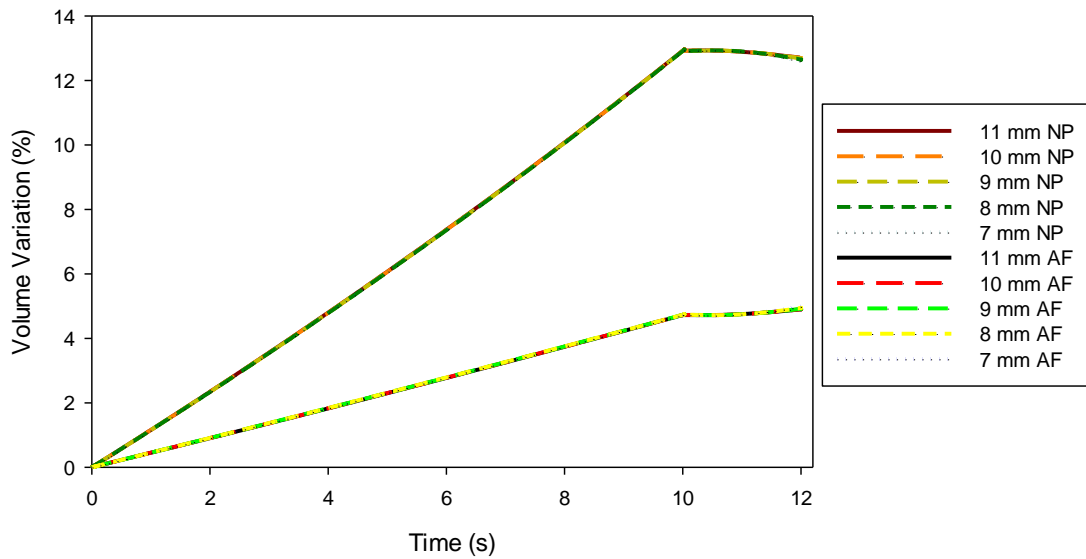


Figure 3.35 - NP and AF volume variation during lateral flexion.

The AF fibers stretching in LFx (Figure 3.36) revealed a similar behavior to that on of the extension results, presenting not only an increase of the number and grade of compressed fibers, but also an increase on the stretch grade of the tensioned fibers.

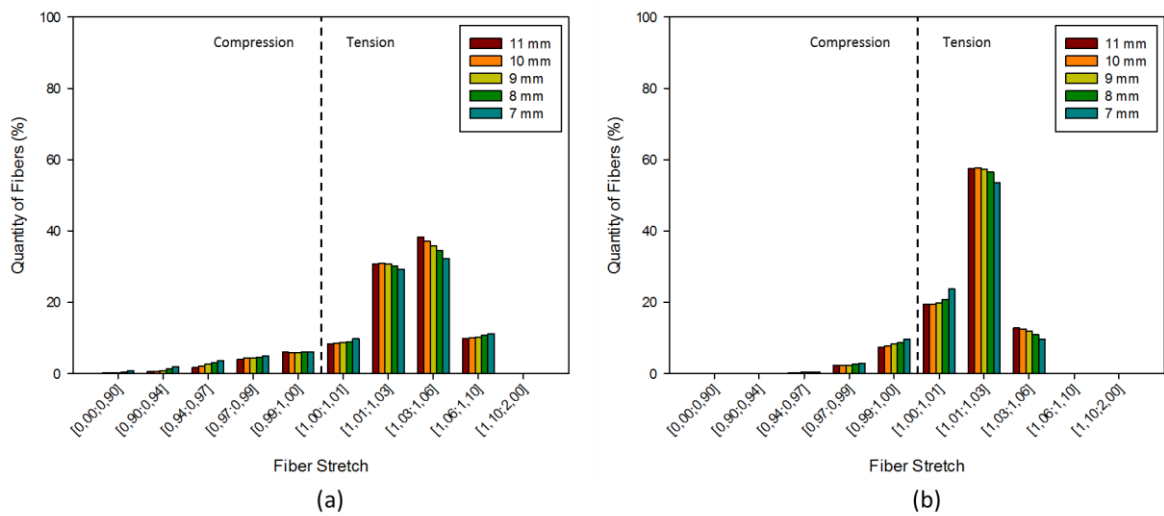


Figure 3.36 - AF fiber stretch during lateral flexion: (a) at 10s - end of pre-conditioning period; (b) at 12s - end of loading period.

As expected, both right and left lateral flexion revealed equal behavior. The range of movement in LFx is presented in Figure 3.37, in which can be noticed that thicker IVD models have higher range of angular movement.

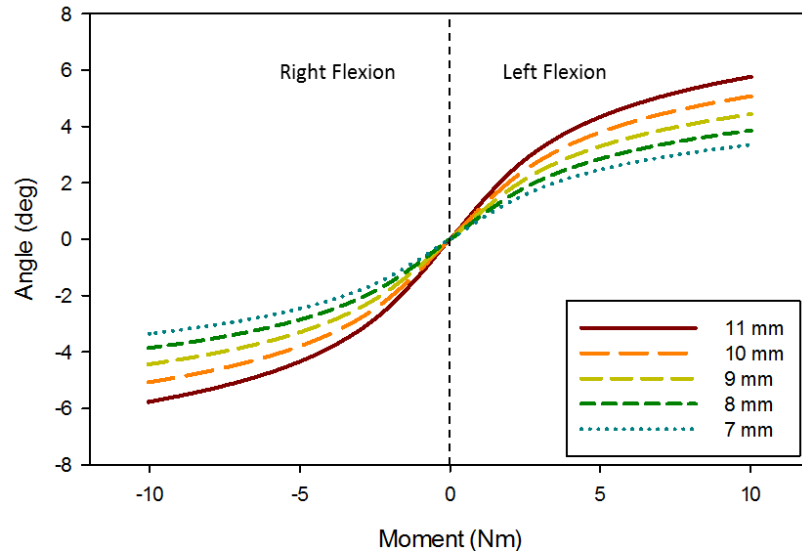


Figure 3.37 - Angular range of bilateral flexion movement.

- Axial Rotation (AR)

Similarly to LFx, clockwise and counterclockwise axial rotations are expected to reveal the same behavior. Therefore, only the results of counterclockwise axial rotation are presented.

The pressure variation of both NP and AF (Figures 3.38 and 3.39) during axial rotation, displayed similar behavior to the LFx movements. In the pre-conditioning period (until $t=10s$), the pressure increases gradually due to a defined volume increase. In the loading period, a more pronounced increase of both NP and AF pressures is observed. However, due to the lack of compressive forces, this subsequent increase implies lower values when compared to Ex-Fx and LFx movements. Besides that, all different IVD models present the same behavior.

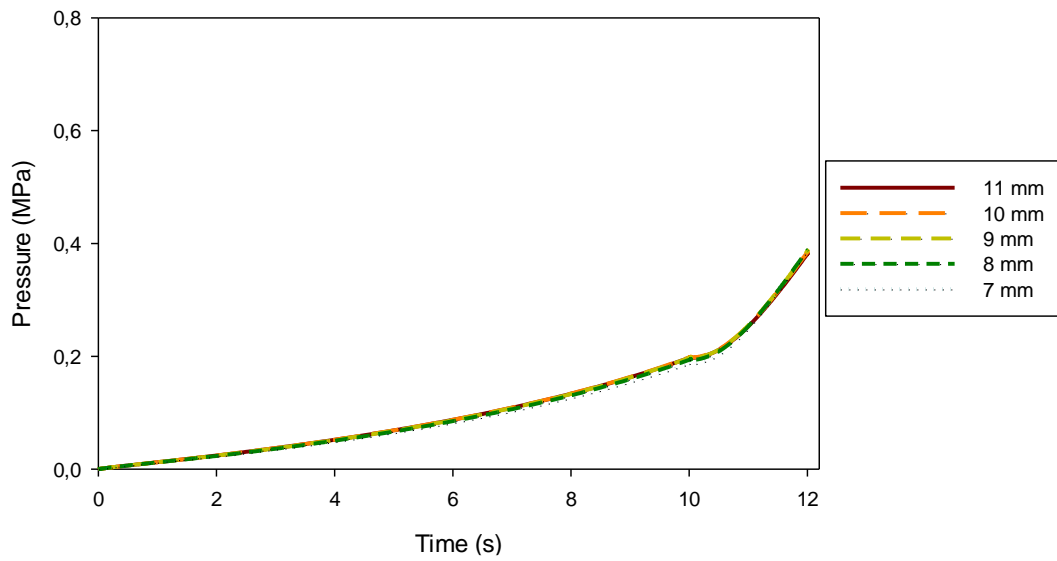


Figure 3.38 - NP pressure variation during axial rotation.

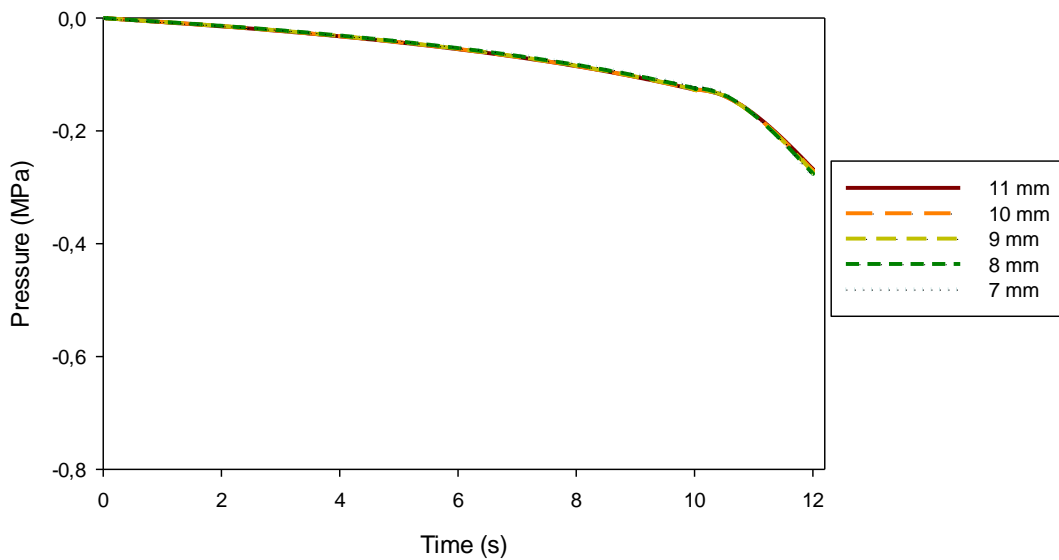


Figure 3.39 - AF pressure variation during axial rotation.

As depicted in Figure 3.40, NP and AF volume variations are identical to those observed Ex-Fx and LFx. However, in the loading period, the decrease and increase of the NP and AF volumes, respectively, are almost imperceptible. As mentioned before, since there are no compressive forces acting, the fluid exchange is almost null, as evidenced by the results.

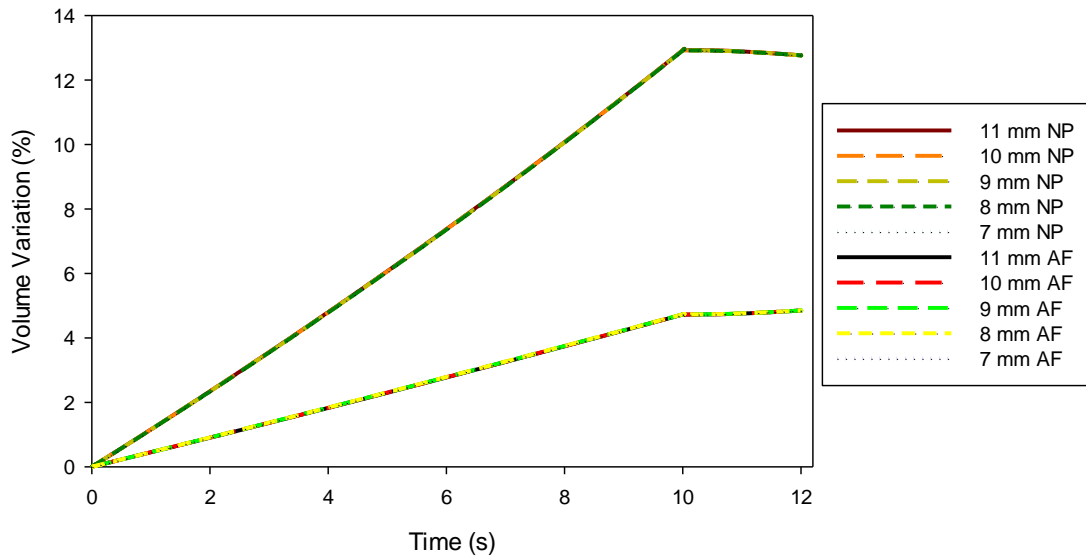


Figure 3.40 - NP and AF volume variation during axial rotation.

The AF fibers stretch results (Figure 3.41) revealed that the majority of fibers (90%) were tensioned at the end of the pre-conditioning period. Yet, during axial rotation, it can be observed that not only the number of fibers in compression increases significantly (30%), but also that the stretch grade of the tensioned fibers increases. These results evidence a higher number of compressed fibers during the loading period comparing to Ex-Fx and LFx movements. The different IVD models revealed identical behavior.

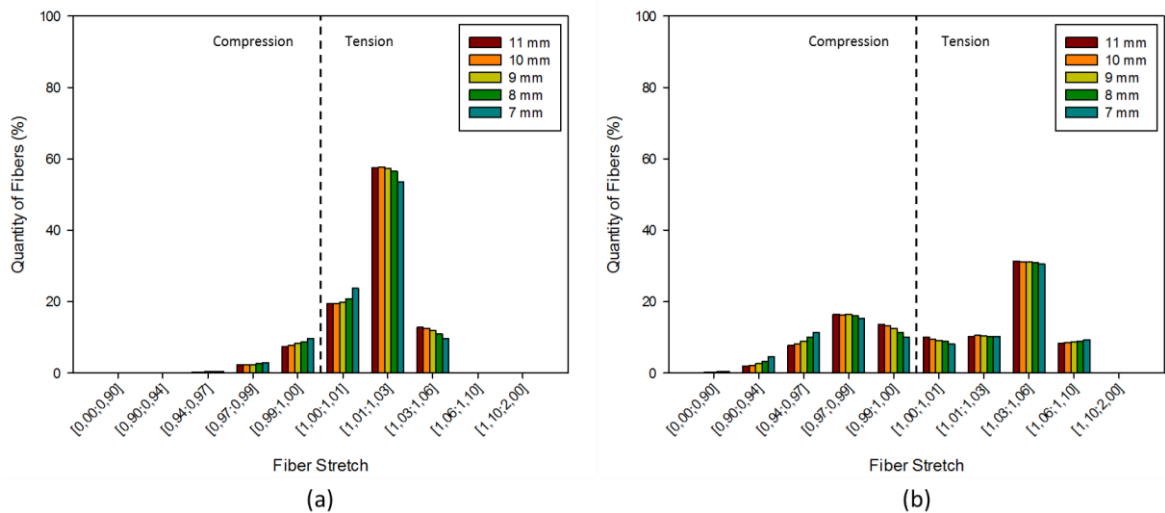


Figure 3.41 - AF fiber stretch during axial rotation: (a) at 10s - end of pre-conditioning period; (b) at 12s - end of loading period.

The axial rotation's range of motion of the different models is presented in Figure 3.42. Comparing to Ex-Fx and FLx, axial rotation presented the smallest range of angular movements. However, it can be noticed that the IVD's height influences the range of motion, as thicker IVDs demonstrates higher angular amplitudes.

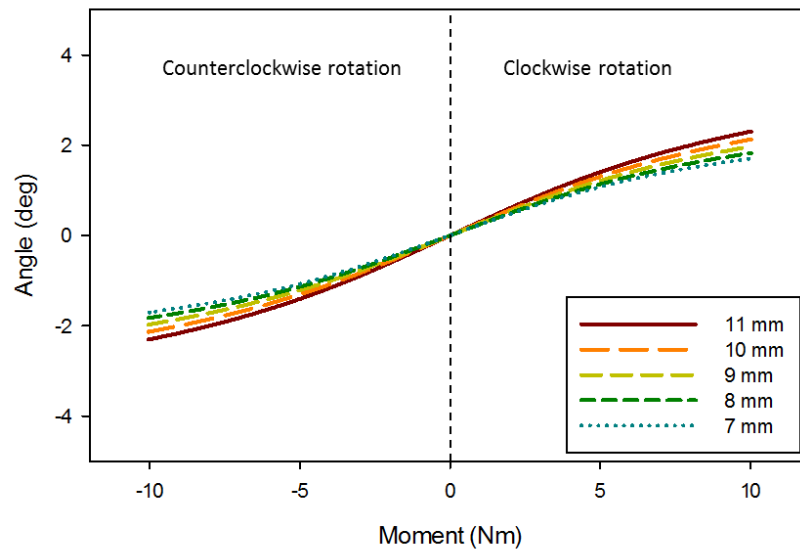


Figure 3.42 - Angular range of axial rotation movement.

Similarly to the variation of the IVD's wedge angle, the disc's average height only influences with significance its range of motion during loading.

To sum up, the angular variations of the IVD's geometry revealed that the main influenced parameter is the angular range of motion, where it is noticed that IVDs with higher wedge angles have a higher range of motion during Ex, but a lower one during Fx. In addition, IVDs with lower wedge angles revealed higher range of motion in LFx. The IVD's angular differences revealed no influence in the angular motion during AR, as all IVDs displayed equal behavior. In what concerns to the pressure and volume variation of the IVD's components, and the AF's fibers stretching, all different models behaved identically, as expected. On the other hand, the variation of the IVD's height revealed that thinner IVDs achieve lower angular amplitudes in all movements. In addition, both IVD's pressure and volume variation, as well as AF's fiber stretch have shown similar behavior for all different IVD models.

These results highlighting the influence of the IVD's geometry in its biomechanical response indicate that the different IVDs along the lumbar spine respond differently to loading stimuli. Therefore, this analysis serves as a starting point for the optimization of a lumbar spine MBS model, described in the next chapter.

CHAPTER 4

Multibody Dynamic Modeling

4.1. Multibody System Formulation

The dynamics of MBS is based on classical mechanics and has a long and prolific history. MBS serve as a basis for many models of mechanical systems and have been applied in many areas of science and engineering [89]. This mathematical formulation is often used to analyze biological and human motion processes.

A general MBS embraces two main characteristics: (i) mechanical components that describe large translational and rotational displacements, and (ii) kinematic joints that impose constraints on the relative motion of the bodies [89]. In a simple manner, a MBS consists of an assembly of rigid and/or flexible bodies interconnected by kinematic joints and possibly some force elements [90]. Driving elements and prescribed trajectories for given points can also be represented under this general concept of MBS [89]. In Figure 4.1, a schematic representation of a MBS is presented.

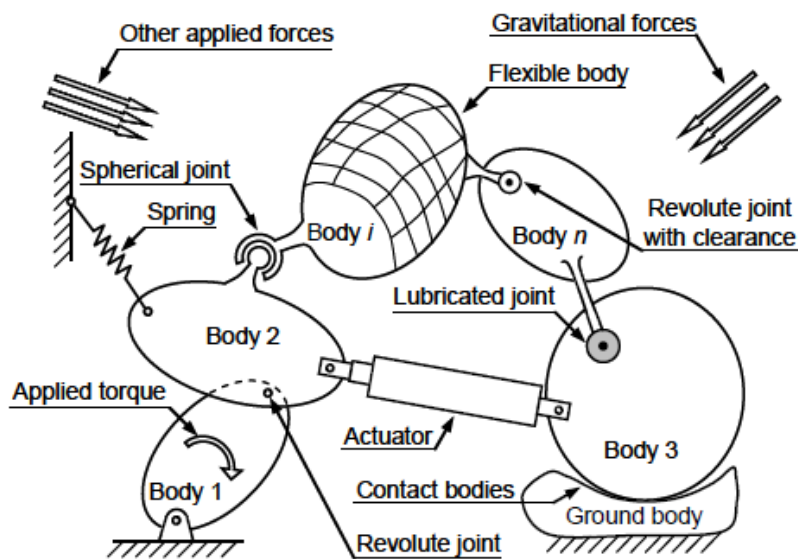


Figure 4.1 - Schematic representation of a general MBS (Adapted from [89]).

The MBS formulation is a powerful tool when it comes to study the motion of a system. However, this mechanical formulation concerns two different approaches for the analysis of a system: (i) a kinematic approach, and (ii) a dynamic approach [89]. On the one hand, using a kinematic approach it is possible to analyze the positions, velocities and accelerations of a MBS without regarding the involved causes. On the other hand, dynamic approaches also consider the forces acting on the system. In addition, MBS can be divided into: (i) forward dynamics analysis, and (ii) inverse dynamics analysis. In a forward dynamics approach, the motion is determined as the result of an external load, while in an inverse dynamics approach, the internal forces and their reactions are calculated based on the system's movements [89].

4.2. 3D Multibody Spine Model

In 2013, Matos presented a 3D MBS model of the human lumbar spine. The model consisted in six rigid bodies, modeling the lumbar vertebrae and the sacrum (L1-S1) linked by spring/damper bushing elements and linear spring/damper sets, representing the IVDs and the lumbar ligaments, respectively. Although the construction of the model was correctly performed, due to mathematical limitations of the used software, its biomechanical response was unadjusted to the implemented motion equations [87]. However, this model served as a starting point to the work of Sousa, which recently, optimized the model of Matos by using six independent spring/damper sets to model each IVD, and therefore, bypassing the software's mathematical limitations [91]. In addition, based on the work of Lourenço [92], Sousa accurately modeled the lumbar ligaments, providing a more realistic biomechanical response. The implemented IVD spring/damper constant equations were parameterized from the FE analysis of a 2° lumbar IVD (performed within the project group) [91].

The model developed by Sousa revealed a good mechanical response under loadings. However, the fact that all lumbar IVDs were modeled with results from only one geometry may compromise the validation of the model. Hence, using the results of the geometry sensibility analysis (reported on Chapter 3), the optimization of the model was performed.

4.2.1. Description of the model

The skeletal part (vertebrae) of the spinal model was built using a 3D free data sharing library. From the 1.80 m original skeleton model, only the lumbar vertebrae and the sacrum were used. Using the work of Keller *et al.*, the vertebrae mass was defined [93]. In Figure 4.2 is presented the original skeleton model and the respective spatial coordinate system.

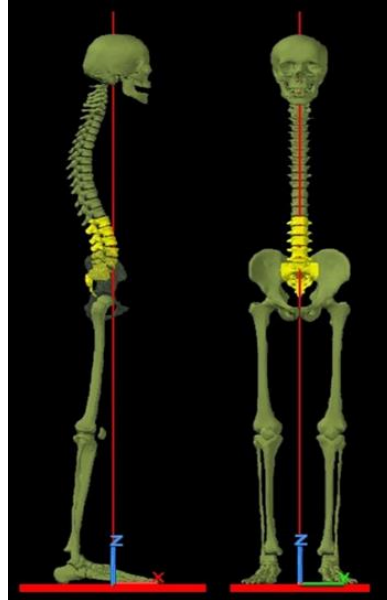


Figure 4.2 - Original model with the referential system highlighted.

The sacrum's position and orientation was maintained from the original model, while the coordinates and angles of the remaining vertebrae were defined by analyzing medical images of the lumbar spine [87]. In Table 4.1 are presented the position, orientation and mass of each rigid component.

Table 4.1 - World position, orientation and mass of the vertebrae (Adapted from [87]).

Vertebra	Angle (°)			Position (m)			Mass (kg)
	x	y	z	x	y	z	
L1	0	8.5	0	-0.032	0	1.17307	0.17
L2	0	6	0	-0.0315	0	1.13675	0.17
L3	0	5	0	-0.025	0	1.09858	0.114
L4	0	5	0	-0.018	0	1.06292	0.114
L5	0	15	0	-0.014	0	1.02479	0.114
S1	0	1.7	0	-0.0333	0	0.98299	6

¹ Absolut values.

Using the same technique as before, the IVDs geometric properties were defined [87]. In Table 4.2 are displayed the position, orientation and thickness of each IVD.

Table 4.2 - World position, orientation and thickness of all IVDs (Adapted from [87]).

IVD	Angle ($^{\circ}$) ¹			Position (m)			Thickness (mm)
	x	y	z	x	y	z	
L1-L2	0	11	0	-0.02473	0	1.15675	0.007877
L2-L3	0	8	0	-0.01872	0	1.1197	0.00895
L3-L4	0	5	0	-0.01153	0	1.08235	0.010515
L4-L5	0	1	0	-0.00528	0	1.04368	0.011588
L5-S1	0	22	0	-0.00875	0	1.006001	0.00719

¹ Absolut values.

As previously mentioned, based on the work of Lourenço, Sousa modeled as spring elements the main lumbar ligaments, namely, anterior longitudinal ligament, posterior longitudinal ligament, ligamentum flavum, interspinous ligament and supraspinous ligament. Based on the experimental data from Chazal, the interspinous and supraspinous ligaments were modeled as a single element [91]. To model the six DOF of each IVD, dummy massless connecting bodies were linked between them and connected to the adjacent vertebrae according to Figure 4.3.

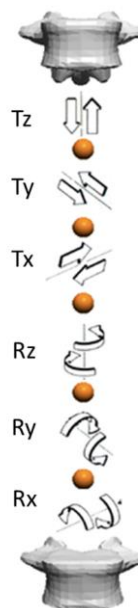


Figure 4.3 - Schematic representation of the IVD modeling.

Six spring/damper sets (three linear and three rotational) were implemented between spheres and/or vertebra to model the relative motion of the IVDs. With the translation movements of each motion segment (MS) already implemented by Sousa, only rotation movements (Ex-Fx, Lfx and AR) were accurately optimized based on the FEM results.

In the previous Chapter, both wedge angle and average height variation results proved the influence of these two geometric features on the IVD's range of movement. However, these characteristics are not totally independent from each other. In a simple manner, by varying the wedge angle of an IVD, an average height variation might be occurring. In addition, the opposite situation does not occur. Therefore, only the FEM results for the wedge angle variation were considered to optimize the MBS model.

4.2.1.1. Intervertebral Discs modeling

Based on the IVD angles of the MBS model (Table 4.1), only five of the seven wedge angle results were selected. The chosen angular values were selected in order to match the IVD wedge angles of the MBS model. Hence, Table 4.3 present the MBS IVD wedge angles and the corresponding FEM results.

Table 4.3 - Wedge angle of the different MBS lumbar levels and corresponding FEM model's angle.

IVD	MBS Model			FEM Model		
	Angle (°) ¹			Angle (°) ¹		
	x	y	z	x	y	z
L1-L2	0	11	0	0	11	0
L2-L3	0	8	0	0	7	0
L3-L4	0	5	0	0	5	0
L4-L5	0	1	0	0	2	0
L5-S1	0	22	0	0	20	0

¹ Absolut values.

In Figures 4.4, 4.5 and 4.6 are displayed the extension-flexion, lateral flexion and axial rotation movements of the selected IVD models.

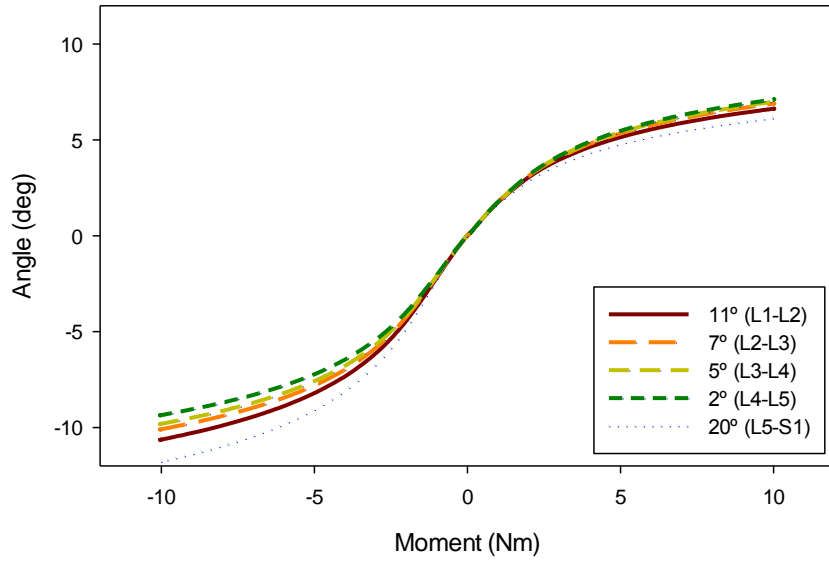


Figure 4.4 - Extension-flexion FEM results.

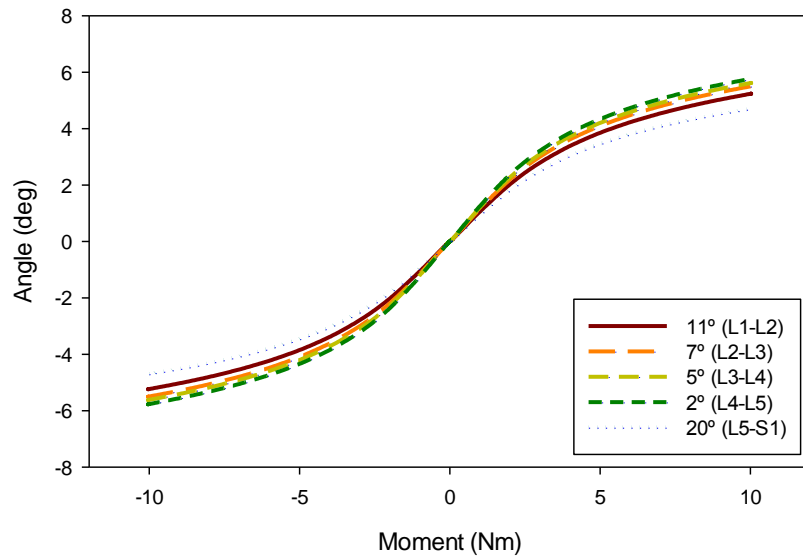


Figure 4.5 - Lateral flexion FEM results.

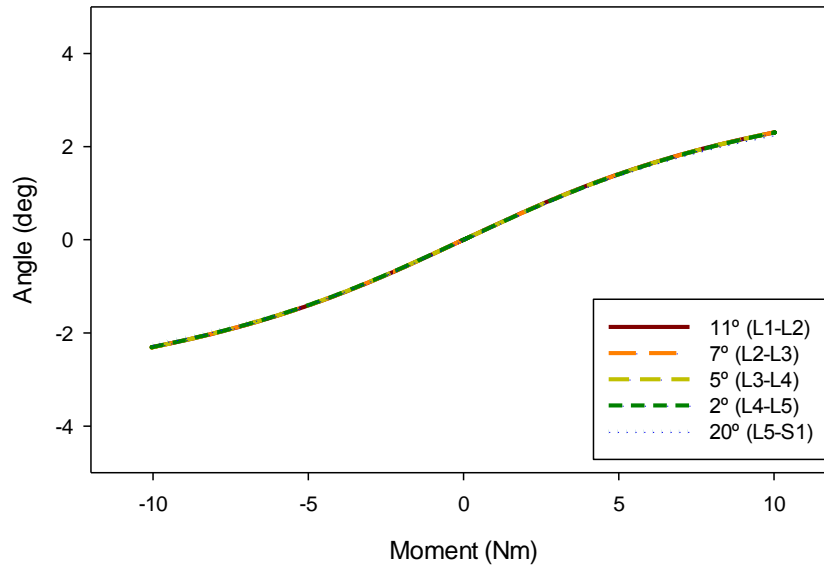


Figure 4.6 - Axial rotation FEM results.

The three rotation movements were modeled by rotational spring/damper sets. These sets are defined by spring natural angle and torque and damping torque. Spring torque is determined by:

$$\text{Spring torque} = -k \cdot x \quad (1)$$

Where k is the spring constant and x is the angle. However, due to limitations of Working Model®, to implement the obtained FEM results in the MBS model, a parameterization of the FEM results was required. Thus, the curves were divided into six linear segments and the respective equations were defined. In Figure 4.7 is depicted an example of the segmentation process performed on the results of L2-L3 during extension-flexion.

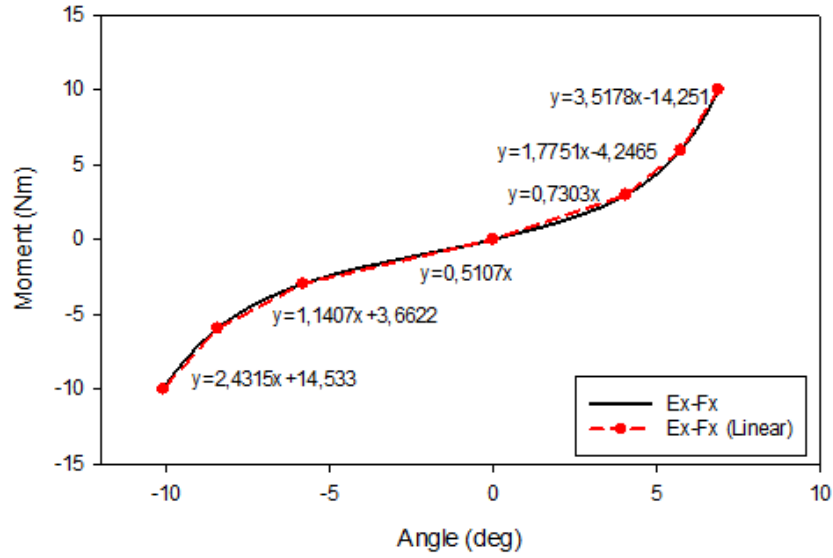


Figure 4.7 - Segmentation and linearization of the L2-L3 Ex-Fx FEM result.

Using this method, six different segments are obtained according to the linear equation:

$$y = kx + b \quad (2)$$

Where k corresponds to the slope of each segment that defines the spring constant. In Table 4.4 are displayed the segmentation points for L2-L3 Ex-Fx movement and the respective k of each segment. Spring constant (k) was implemented in Working Model® as an if function:

$$k = \text{if}(\text{spring angle} < x_1, k_1, \text{if}(\text{spring angle} < x_2, k_2, \text{if}(\text{spring angle} < x_n, k_n))) \quad (2)$$

Where x_n and k_n match respectively, the angle and k values from Table 4.4. Hence, for the Ex-Fx movement of L2-L3 MS, spring constant equation was implemented as:

$$k = \text{if}((-constraint[207].r.y) < -5.7409 \text{ deg}, 3.5178, \text{if}((-constraint[207].r.y) < -4.0644 \text{ deg}, 1.7751, \text{if}((-constraint[207].r.y) < 0 \text{ deg}, 0.7303, \text{if}((-constraint[207].r.y) < 5.8125 \text{ deg}, 0.5107, \text{if}((-constraint[207].r.y) < 8.42133 \text{ deg}, 1.1407, 2.4315)))))) \text{ Nm/deg} \quad (3)$$

Table 4.4 - Segmentation parameters for L2-L3 Ex-Fx movement.

L2-L3 (Ex-Fx) Parameterization			
Segment	Moment (Nm)	Angle (deg)	k (Nm/deg)
1	-10	-10.089	2.4315
	-5.94425	-8.4213	
2	-5.94425	-8.4213	1.1407
	-2.96825	-5.8125	
3	-2.96825	-5.8125	0.5107
	0	0	
4	0	0	0.7303
	2.96825	4.0644	
5	2.96825	4.0644	1.7751
	5.94425	5.7409	
6	5.94425	5.7409	3.5178
	10	6.8939	

According to specificities of the software, beside the spring constant equation, the creation of an additional function to adjust the spring's natural angle was necessary to adjust the spring curve's behavior. The curve adjustment procedure is described in detail by Sousa [91].

The modeling procedure was applied to Ex-Fx, LFx and AR results from all lumbar IVD models. In Figure 4.8 are displayed the anterior, left lateral and posterior view of the three-dimensional MBS model of the human lumbar spine.

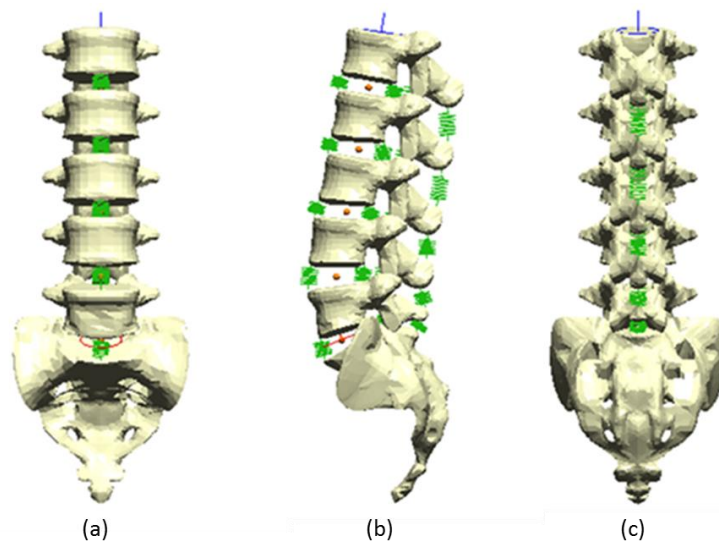


Figure 4.8 - Three-dimensional MBS model of the lumbar spine: (a) anterior view; (b) left lateral view; (c) posterior view.

4.2.2. Comparison of FEM and MBS results

In order to validate the MBS modeling method, a comparison of both FEM and MBS results was performed. Therefore, all five lumbar MSs were simulated individually under the same conditions of the FEM simulation. Each MS was simulated three times under three incremental pure moments for two seconds. Figure 4.9 displays the incremental moment applied at the top of the MS.

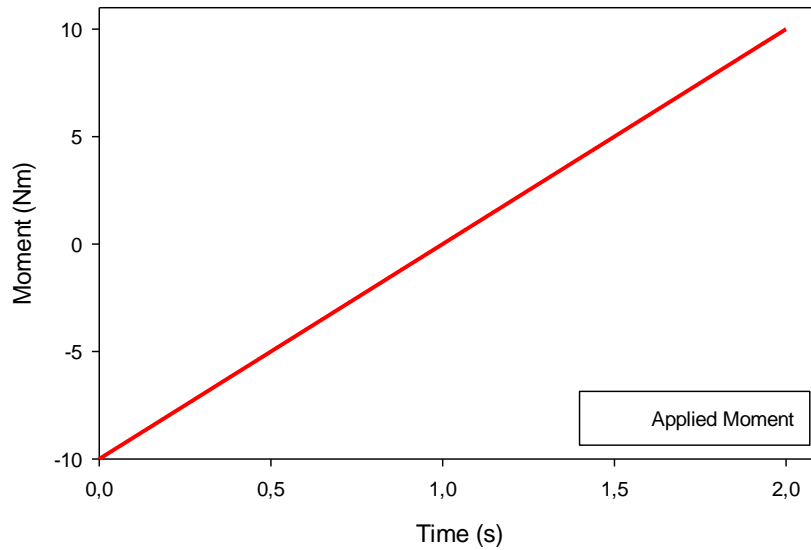


Figure 4.9 - Incremental moment applied.

Since the FEM analysis of the IVDs was performed without considering the lumbar ligaments, the MBS model was simulated with the lumbar ligaments disabled and the results were compared. In addition, to observe the influence of lumbar ligaments during motion, the MBS model with the ligaments enabled was also simulated. In Figures 4.10 – 4.14 are presented the FEM and MBS results of Ex-Fx movement for each lumbar level.

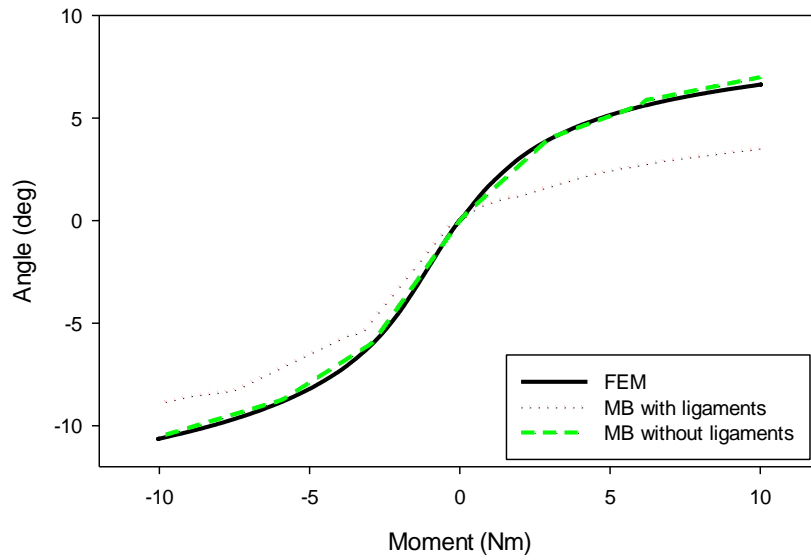


Figure 4.10 - Extension-flexion FEM and MBS simulation results of L1-L2.

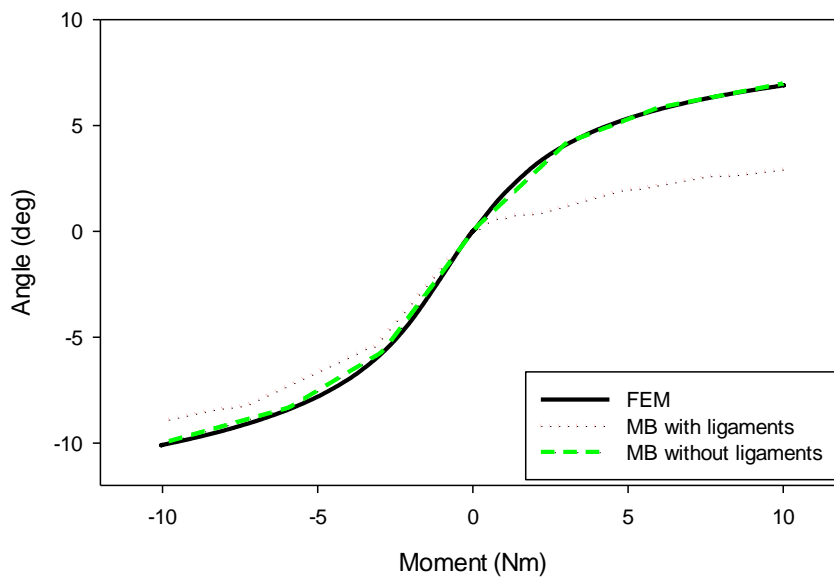


Figure 4.11 - Extension-flexion FEM and MBS simulation results of L2-L3.

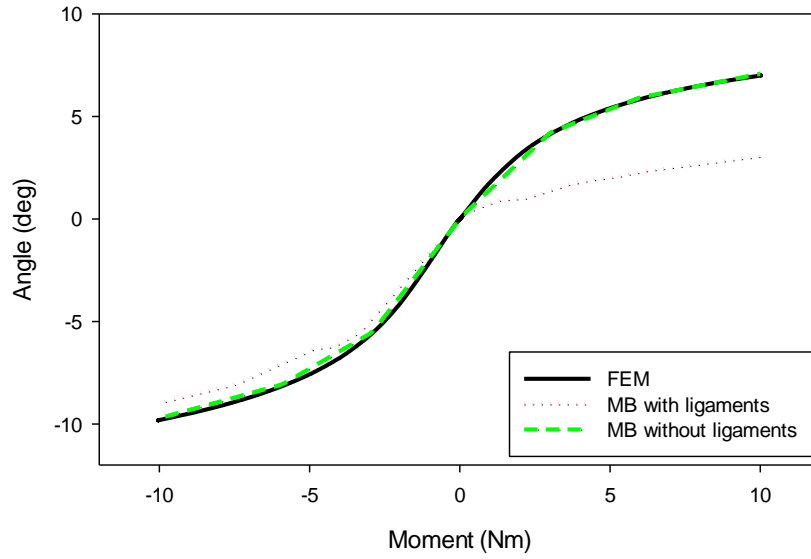


Figure 4.12 - Extension-flexion FEM and MBS simulation results of L3-L4.

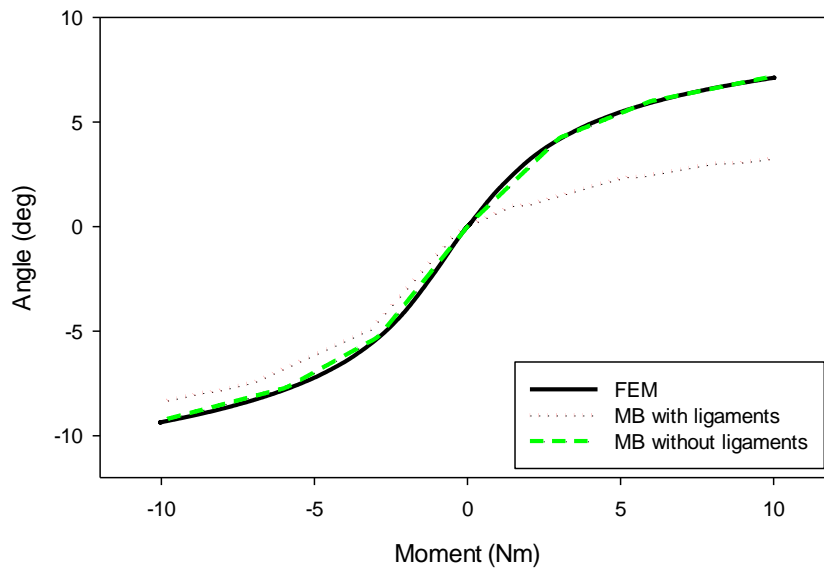


Figure 4.13 - Extension-flexion FEM and MBS simulation results of L4-L5.

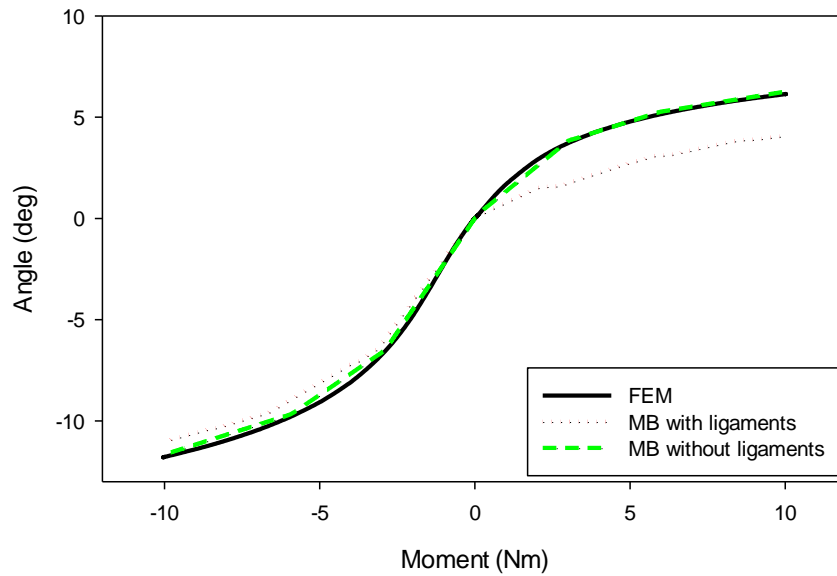


Figure 4.14 - Extension-flexion FEM and MBS simulation results of L5-S1.

Both FEM and MBS (without ligaments) results show a very similar behavior, which indicates the success of the implemented MBS modeling procedure. In addition, these results reveal the importance of lumbar ligaments on the limitation of the range of motion. By adding ligaments, the angular range decreased 6-11% in extension and 33-54% in flexion.

In Figures 4.15 – 4.19 are displayed the FEM and MBS simulation results for lateral flexion movement.

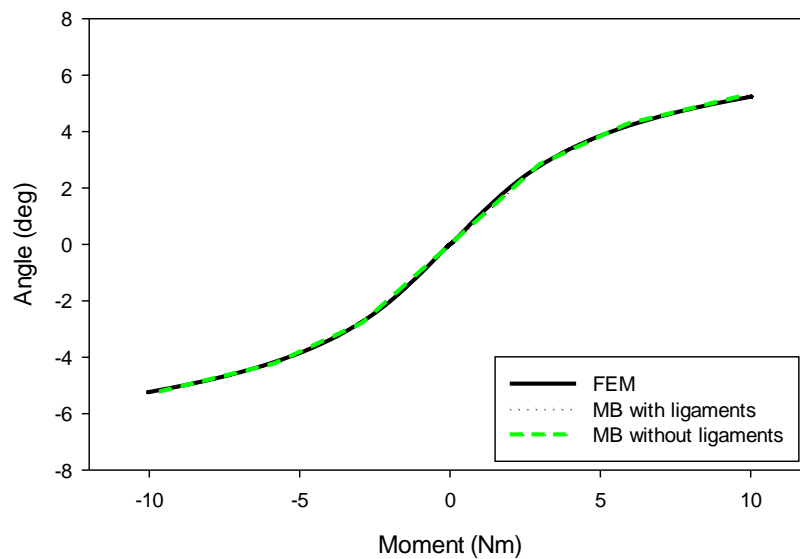


Figure 4.15 - Lateral flexion FEM and MBS simulation results of L1-L2.

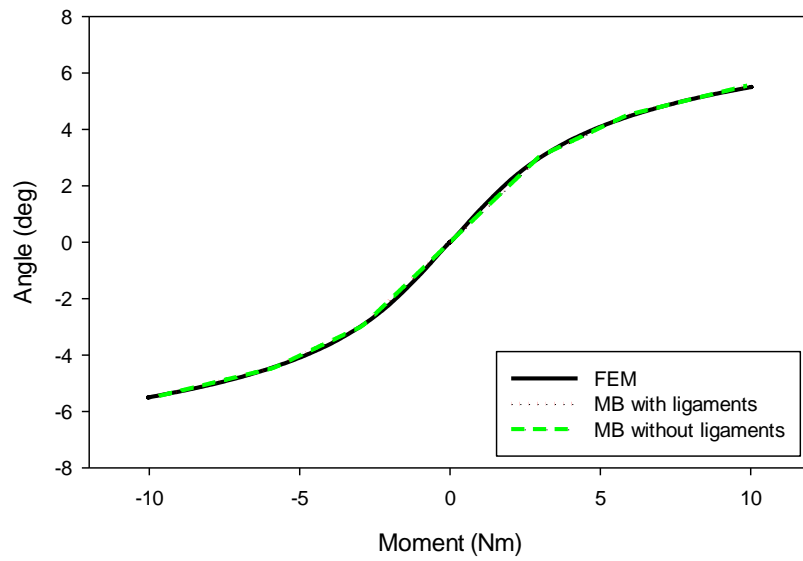


Figure 4.16 - Lateral flexion FEM and MBS simulation results of L2-L3.

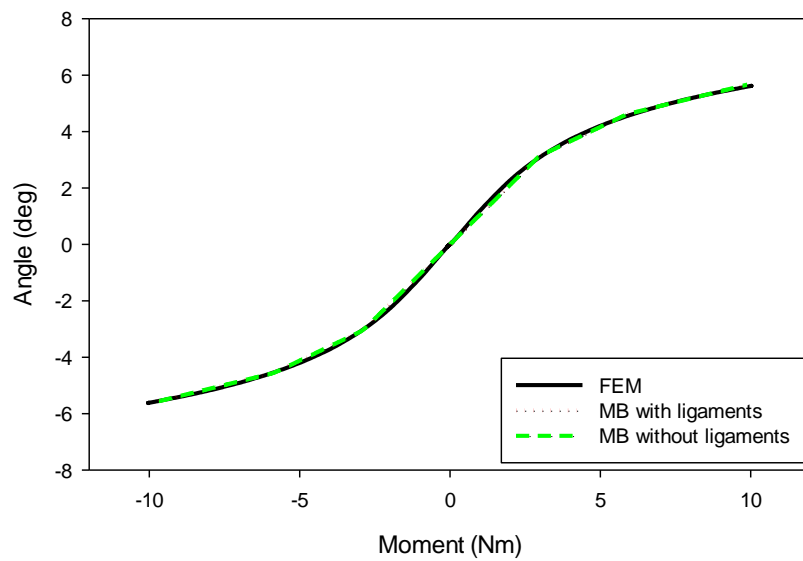


Figure 4.17 - Lateral flexion FEM and MBS simulation results of L3-L4.

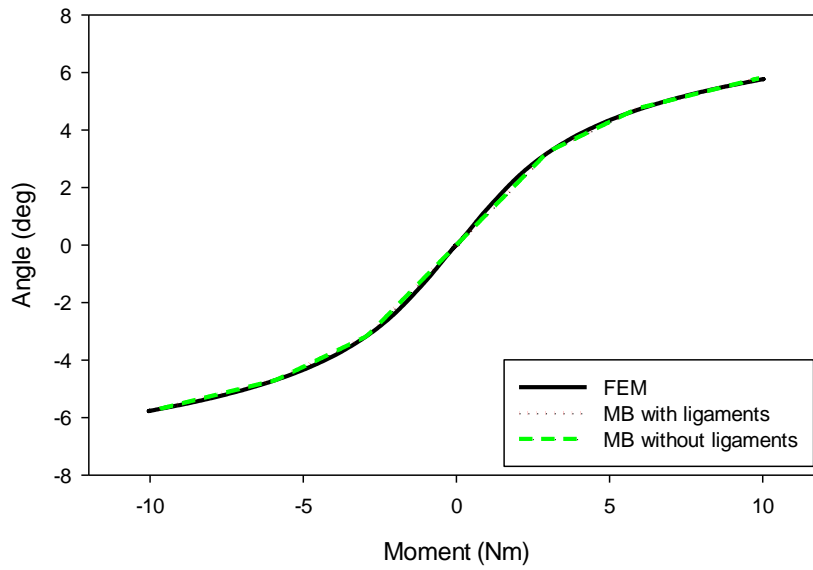


Figure 4.18 - Lateral flexion FEM and MBS simulation results of L4-L5.

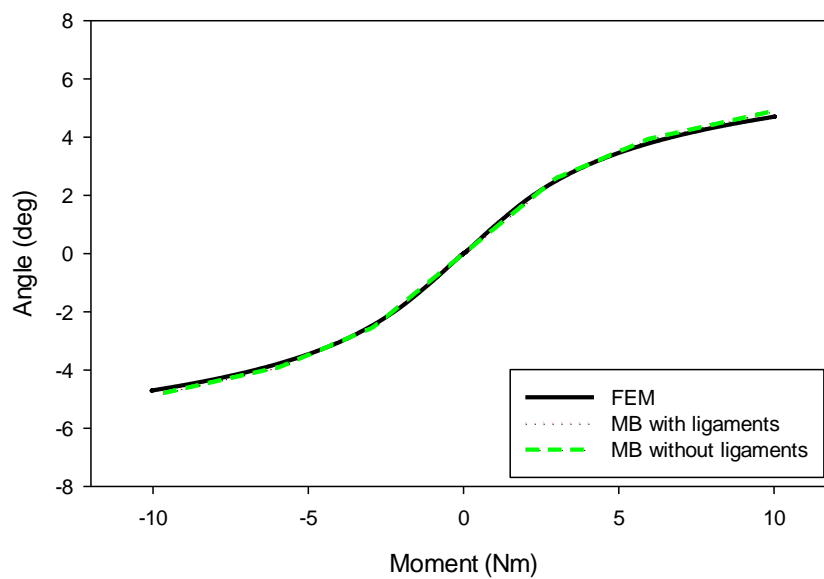


Figure 4.19 - Lateral flexion FEM and MBS simulation results of L5-S1.

The presented lateral flexion simulation results evidences the equal behavior between FEM and MBS curves. In addition, the presence of lumbar ligaments during this type of motion proves to be irrelevant.

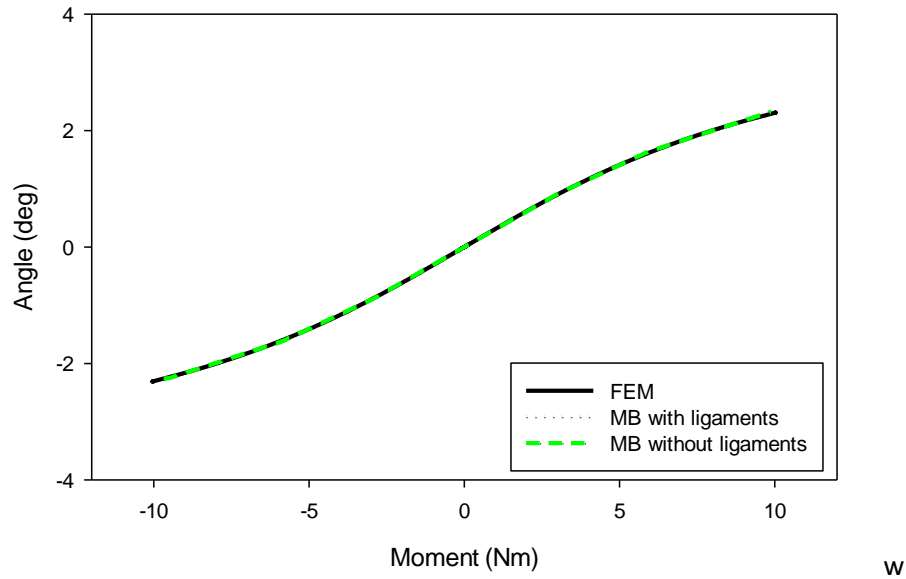


Figure 4.20 - Axial rotation FEM and MBS simulation results of all modeled IVDs.

Since the axial rotation FEM results proved to be equal in all IVDs, the MBS modeling of ARx was performed based on a single FEM curve. Figure 4.20 presents both FEM and MBS curves (with and without ligaments). One can observe that ligaments seems to be not influencing the range of motion.

These results indicate the correct implementation of the FEM results in the MBS lumbar spine model, as both FEM and MBS (without ligaments) curves seem to fit perfectly in each other.

4.2.3. Validation of the model

To validate the MBS model, a comparison between the simulation results and experimental data from Guan *et al.*, Panjabi *et al.* and Yamamoto *et al.* was performed [88,94,95].

In the work of Panjabi *et al.*, the three-dimensional motion of each lumbar intervertebral level was measured under different types of loadings. Nine fresh-frozen cadaveric human lumbar spine specimens were loaded under three pure moments, promoting Ex-Fx, LFx and AR movements. The measured displacements were determined with the use of stereophotogrammetry [95].

The study performed by Guan *et al.* describes the experimental tests performed on the lumbar spine to test the hypothesis that the lumbosacral joint (L1-S1) behaves differently than the other lumbar intervertebral joints. Ten cadaveric lumbar spines were used and pure moments were applied at the top of L1 to simulate Ex-Fx and LFx [94].

The work of Yamamoto *et al.* reports the experimental tests performed on ten cadaveric human lumbar spines. In their study, the specimens (between 25-63 years old) were tested under pure moments to test the range of motion of all lumbar intervertebral joints in Ex-Fx, LFx and AR [88]. However, the resulting data from this work present only the complete range of motion during the three movements, and do not display the evolutionary behavior during the incremental loading. Therefore, these results will be compared with the total range of motion of the model posteriorly.

The developed MBS model was simulated under the same conditions to assess its accuracy in reproducing the human lumbar motion. Three pure moments were applied to the superior vertebral endplate (VEP) of L1, and the resulting angular motion of each intervertebral level was measured and compared with the experimental data.

Figures 4.21 – 4.25 show both simulation results and experimental data (from Panjabi *et al.*, and Guan *et al.*) of Ex-Fx movement.

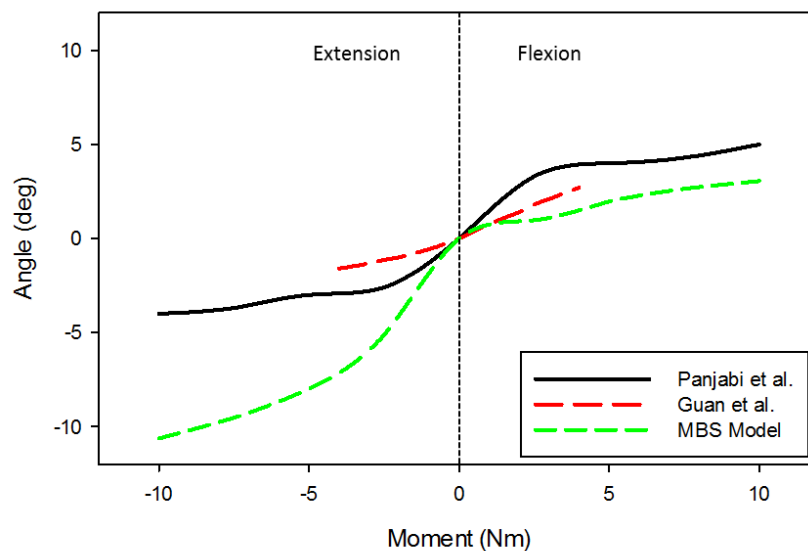


Figure 4.21 - Comparison between experimental and simulation results of L1-L2 during Ex-Fx.

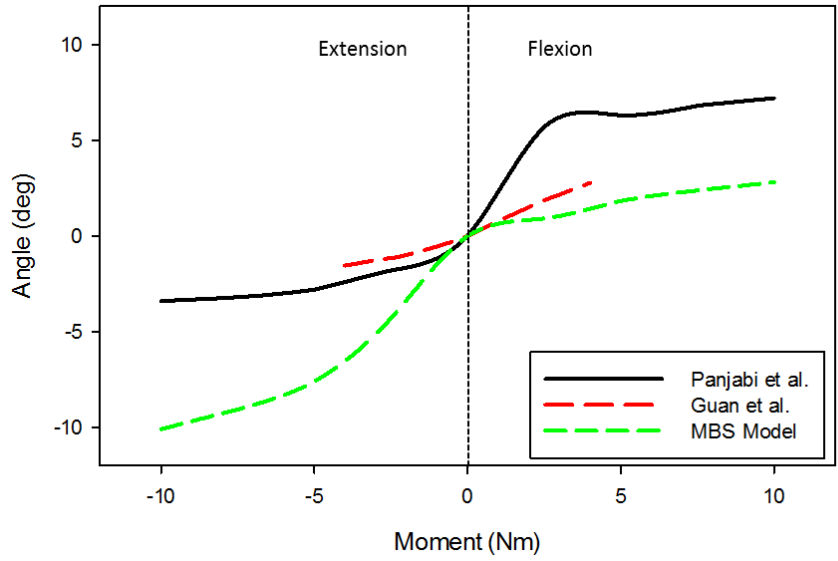


Figure 4.22 - Comparison between experimental and simulation results of L2-L3 during Ex-Fx.

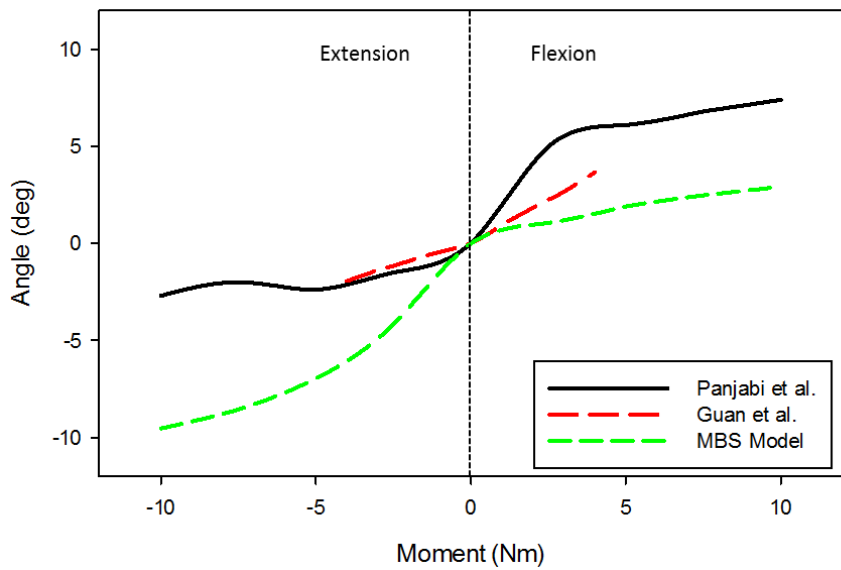


Figure 4.23 - Comparison between experimental and simulation results of L3-L4 during Ex-Fx.

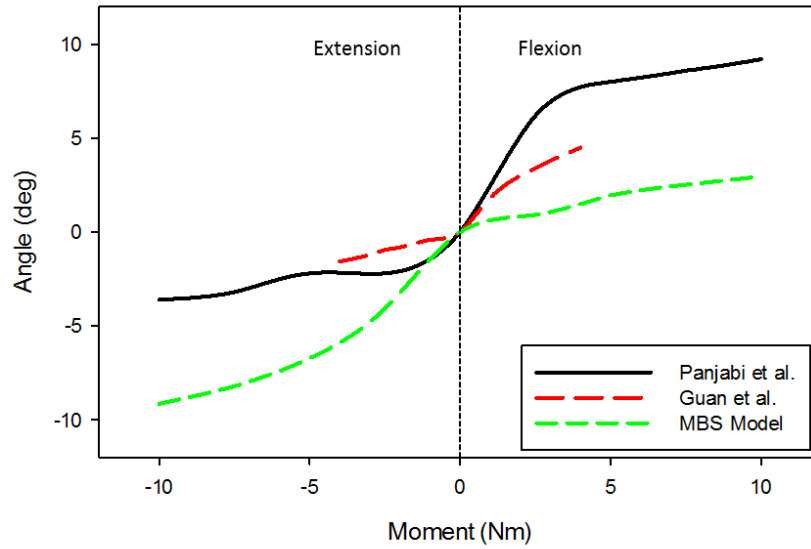


Figure 4.24 - Comparison between experimental and simulation results of L4-L5 during Ex-Fx.

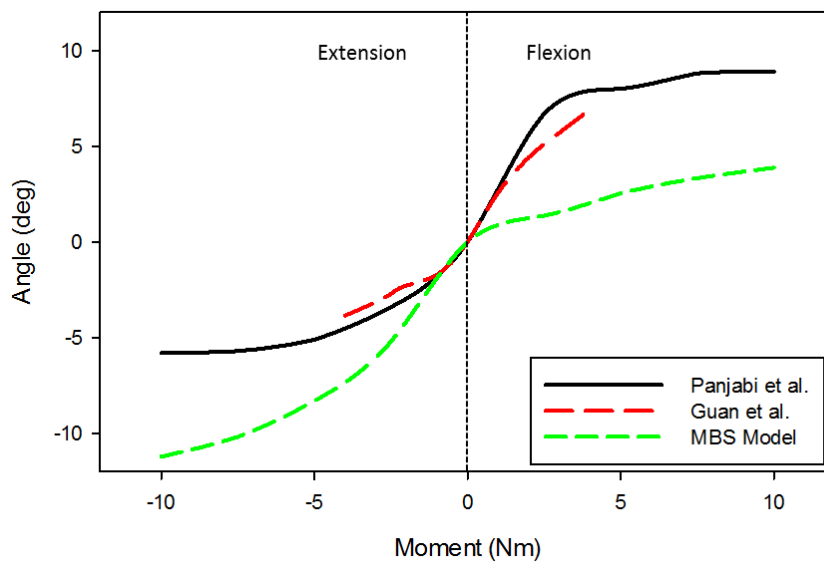


Figure 4.25 - Comparison between experimental and simulation results of L5-S1 during Ex-Fx.

These results show significant differences between the experimental data and the simulation results. On the one hand, during extension, the MBS model present higher range of motion at all lumbar levels comparing to the experimental data. On the other hand, the experimental results demonstrate substantially higher amplitudes during flexion in all MSs. The behavior of the MBS model can be described as more flexible in extension and more rigid in flexion, by comparing with experimental data. Although the presence of ligaments in the model contribute to these results, it was

previously demonstrated that even without ligaments, the MBS model present a higher range of motion in extension than in flexion.

Contrarily to the work of Panjabi *et al.* and Guan *et al.*, in the work of Yamamoto *et al.* it is not evidenced the evolution of the angle with the applied moment, but only the resulting range of motion during Ex-Fx and LFx. Nonetheless, the angular amplitude quantification of both Ex-Fx and LFx movements was performed. Figure 4.26 displays the total range of motion during Ex-Fx of experimental and simulation results.

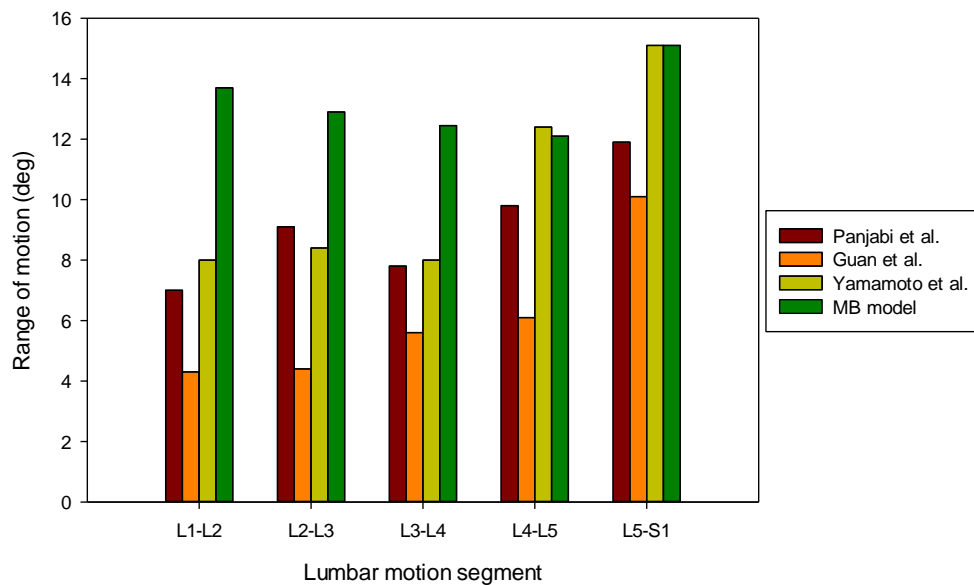


Figure 4.26 - Total range of motion during Ex-Fx of both experimental and simulation results.

Although these results may induce some errors in its interpretation, some conclusions can be established. Similarly to the experimental data, the MBS model reveals the highest range of motion in the L5-S1 MS. In addition, for both L4-L5 and L5-S1 the model's Ex-Fx amplitude is similar to the experimental data of Yamamoto *et al.*

Figures 4.27 – 4.31 show the comparison between the MBS model and experimental results during lateral flexion.

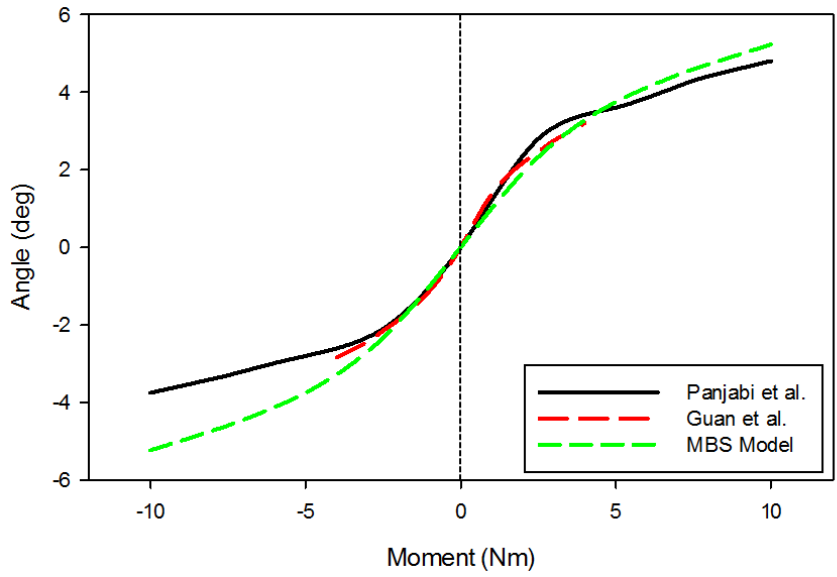


Figure 4.27 - Comparison between experimental and simulation results of L1-L2 during LFx.

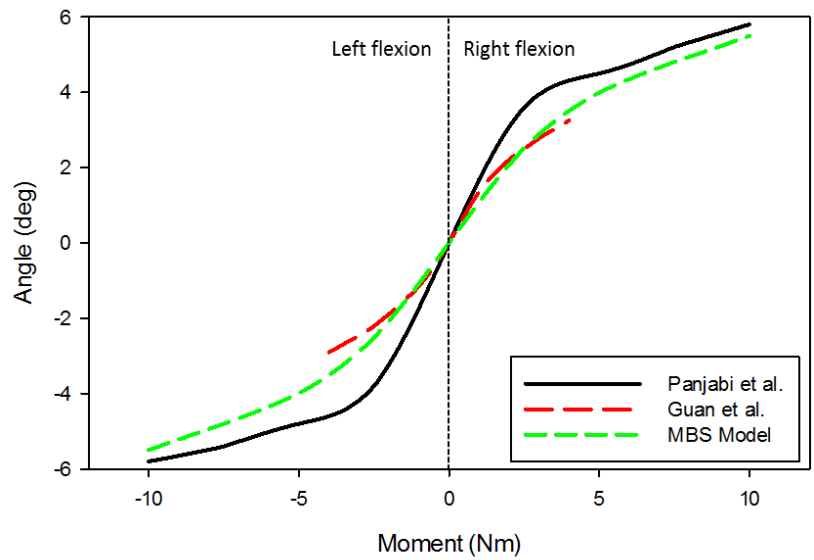


Figure 4.28 - Comparison between experimental and simulation results of L2-L3 during LFx.

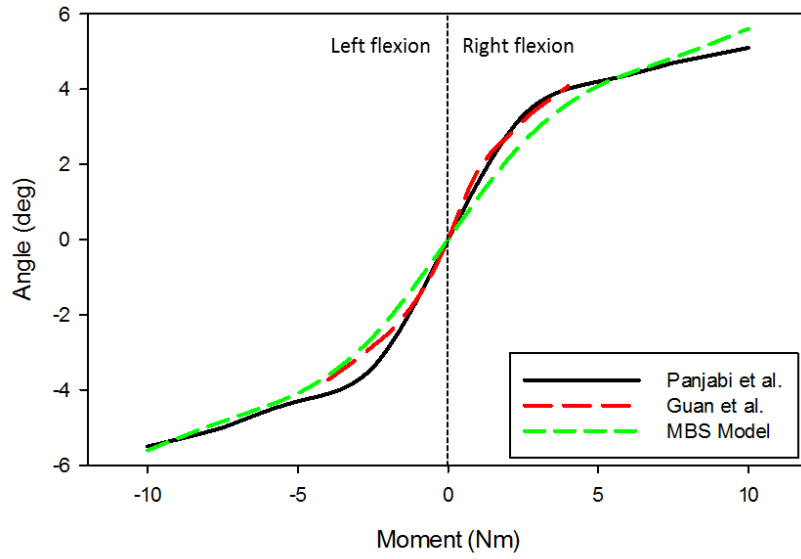


Figure 4.29 - Comparison between experimental and simulation results of L3-L4 during LFx.

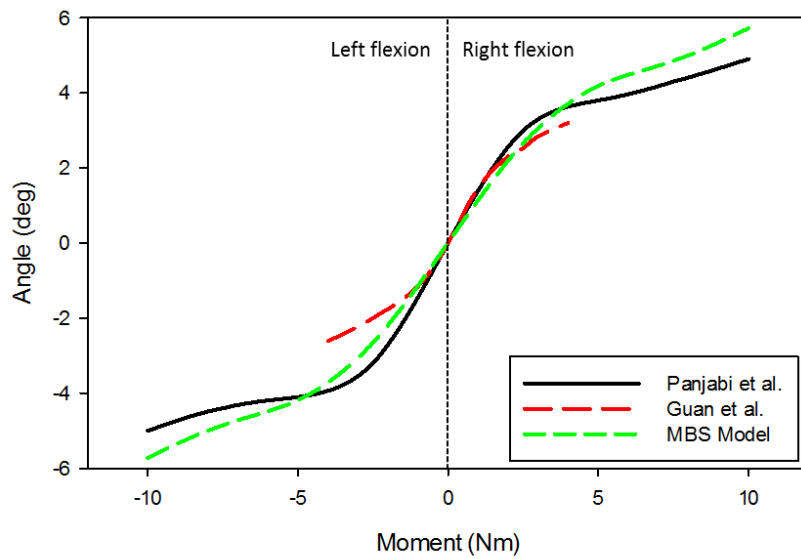


Figure 4.30 - Comparison between experimental and simulation results of L4-L5 during LFx.

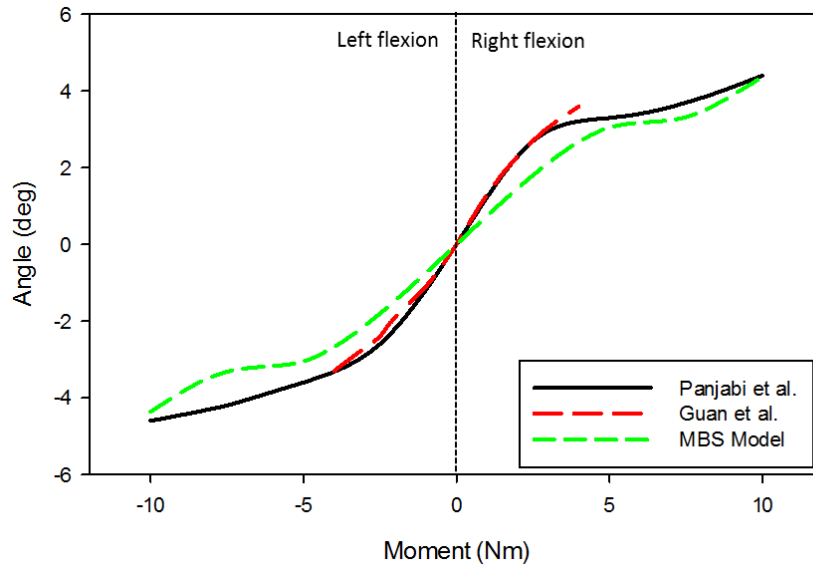


Figure 4.31 - Comparison between experimental and simulation results of L5-S1 during LFx.

By interpreting these results, it is possible to notice that the curves relative to the experimental data present two phases: (a) linear, for small moments (under 4 Nm), and (b) nonlinear, for moments higher moments (over 5 Nm). The behavior of the MBS model also reveal this tendency, being very similar in the linear phase, especially in L1-L2.

The experimental curves also reveal a higher range of motion for the left lateral flexion in all MSs. The reason for this fact may be related with the experimental settings or with the asymmetry of the body segments. In addition, the authors report that L2-L3 presents the highest range of motion during LFx. Similarly, in the MBS results it is possible to observe this same tendency, with L2-L3 MS revealing the higher amplitude of motion.

Figure 4.32 shows the total angular range of each MS during LFx.

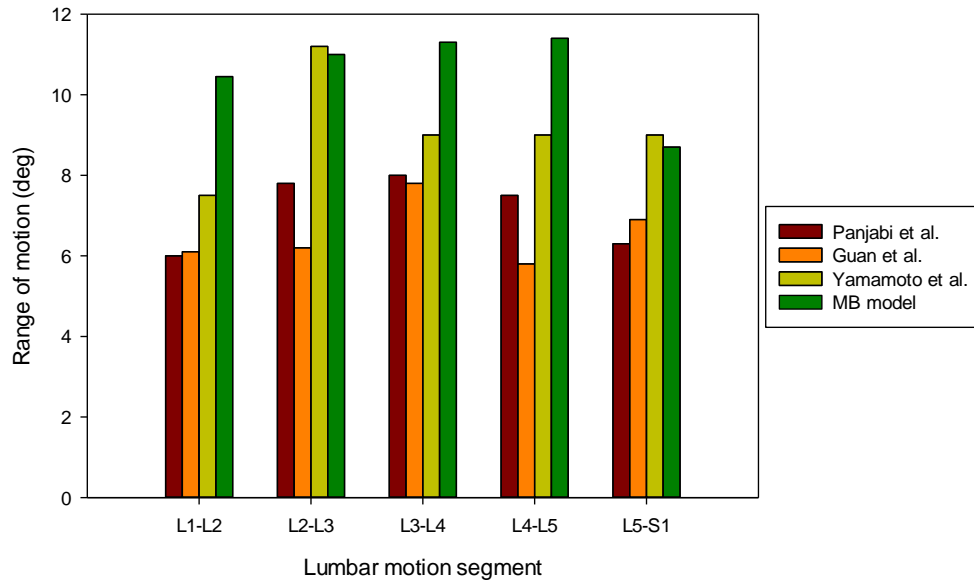


Figure 4.32 - Total range of motion during LFx of both experimental and simulation results.

Noticeable similarities can be observed between the total range of motion of the MBS model and the experimental data from Yamamoto *et al.*, especially in L2-L3 and L5-S1. However, these results are not conclusive in terms of the behavior of the lumbar spine under loading. In Figure 4.31 it is also possible to notice that, in general, the MBS model has a more flexible behavior than the experimental results.

Figures 4.33 – 4.38 depict the comparison between experimental and simulation results for AR movement in all lumbar IVDs. The work of Panjabi *et al.* is the only one describing the evolution of the angular displacement under pure moments. Therefore, the simulation results are only compared with the experimental data obtained by Panjabi *et al.*

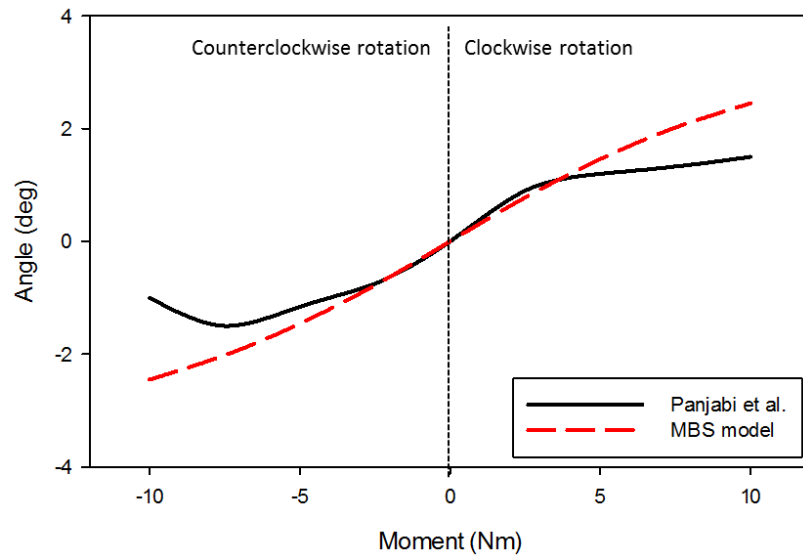


Figure 4.33 - Comparison between experimental and simulation results of L1-L2 during AR.

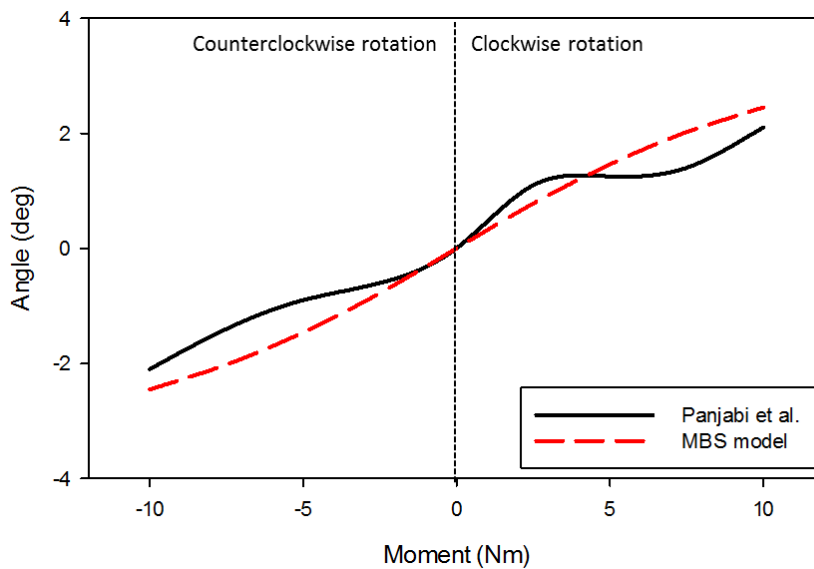


Figure 4.34 - Comparison between experimental and simulation results of L2-L3 during AR.

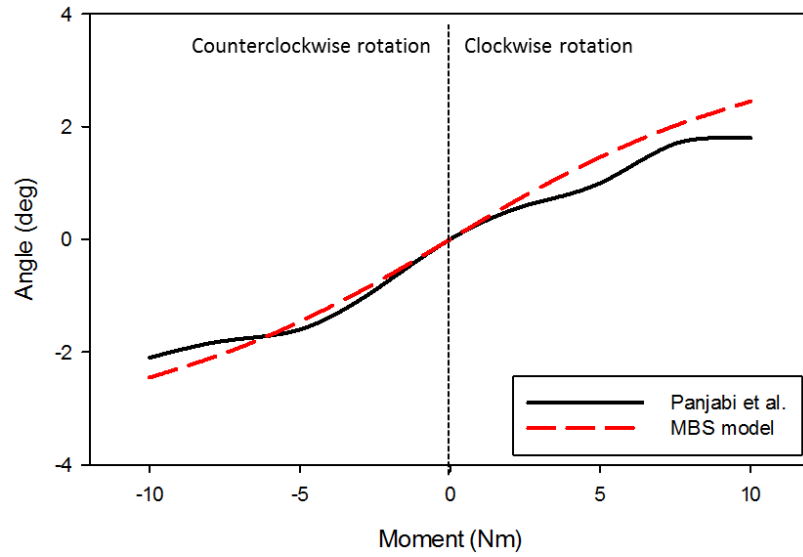


Figure 4.35 - Comparison between experimental and simulation results of L3-L4 during AR.

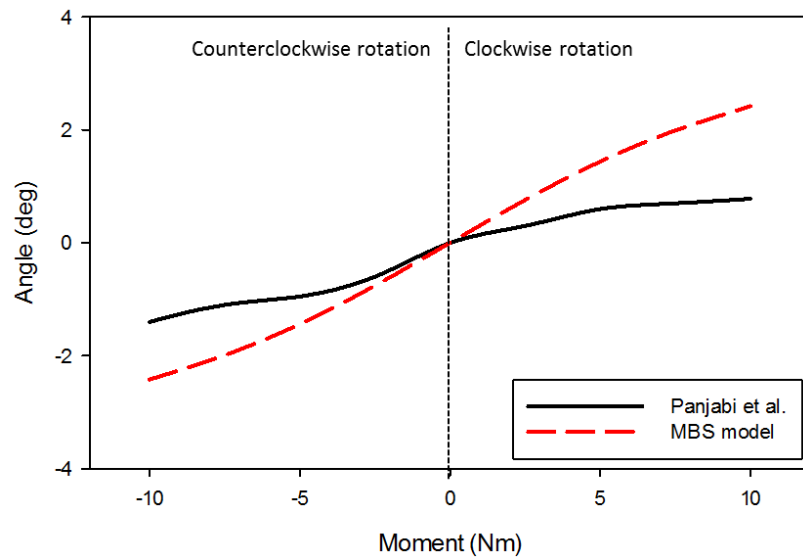


Figure 4.36 - Comparison between experimental and simulation results of L4-L5 during AR.

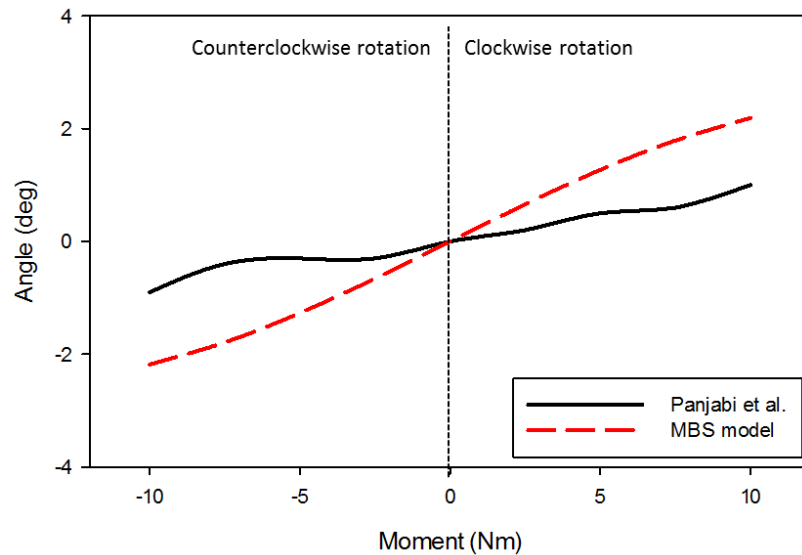


Figure 4.37 - Comparison between experimental and simulation results of L5-S1 during AR.

In general, the behavior of both curves is similar, having some coincident points, particularly in the first three lumbar levels. In their work, Panjabi *et al.* report that L2-L3 present significantly higher range of motion than L4-L5, however, in the MBS results the differences are not so clear [95]. In addition, the MBS axial rotation has the same range of motion for all intervertebral joints, as it was modeled based on only one curve's behavior. The implementation of capsular ligament, which dampens the contact between facet joints and limits the distance between facet joints, could provide to the MBS curve, a better fitting to the experimental data.

4.2.4. Application of the model

After validating the model, it is important to assess the model in order to comprehend its dynamic response under different loading conditions. From a mechanical point of view, the lumbar spine is an interconnected system that responds simultaneously to the applied loads. However, there are some mechanical parameters that cannot be measured *in vivo*, so the use of dynamic models is the best approach. An example of it, is the load distribution in the spine when a force is applied. As stated by White *et al.*, lower lumbar levels are more susceptible to disc degeneration and/or disorders [16]. This fact is related with the reaction forces experienced by the lower lumbar IVDs, particularly the L4-L5 and L5-S1.

In this section a simulation is presented, in which forces are applied in order to measure the reaction in each different lumbar level. Firstly, four values of force in the X-axis (promoting flexion) were applied in L1, with the values of 250, 500, 600 and 700 N. These values were selected based on the work of Sousa [91]. In Figures 4.38 and 4.39 are displayed respectively X and Z reaction forces (Rx and Rz) on each IVD when flexion-promoting forces are applied.

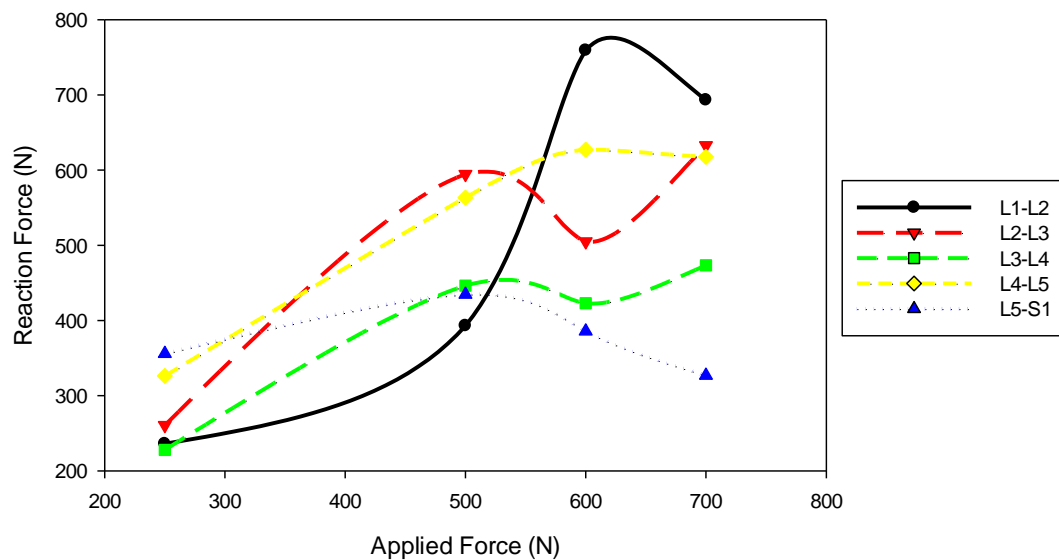


Figure 4.38 - Measured reaction forces (X-axis) when different loads are applied in X-axis.

As expected, in general the results show different Rx values for each IVD. For the lowest applied load (250 N) it can be noticed that L4-L5 and L5-S1 present the highest reaction values. However, as the applied force increases substantially (over 500 N), the reaction in L5-S1 tends to decrease, but in L4-L5 increases significantly. In addition, for the highest force applied (700 N), the highest reaction values were measured in L1-L2. Yet, the highest mean of all IVD's reaction values during simulation corresponds to the L4-L5 IVD.

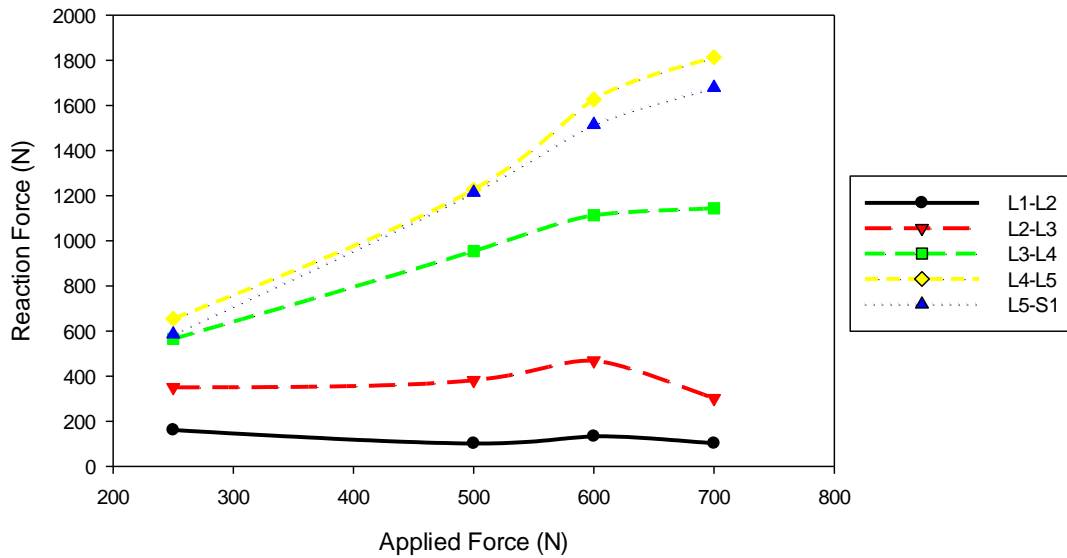


Figure 4.39 - Measured reaction forces (Z-axis) when different loads are applied in X-axis.

The Z reactions results display a specific pattern, with all R_z values from the different IVDs revealing a linear behavior. However, it can be observed that the lowest three IVDs (L3-L4, L4-L5 and L5-S1) present significantly higher R_z values than the other two. In addition, L4-L5 displays the higher reaction values in all cases.

The reaction values along the Y-axis are not presented, as they are null during the application of a force in X-axis.

Both in X and Z axes, the L4-L5 IVD present the highest reaction values when flexion-promoting forces are applied at L1. This may be related to the fact that the lower lumbar levels present a pronounced anatomical inclination in relation to the applied forces [64].

In addition to these conditions, the MBS model was also subjected to compressive and lateral bend-promoting forces applied (Z and Y axes). The applied force values were selected based on the study of Sousa [91]. Figures 4.40 and 4.41 depict both Y and Z reaction forces when a lateral bend-promoting force (Y-axis) is applied.

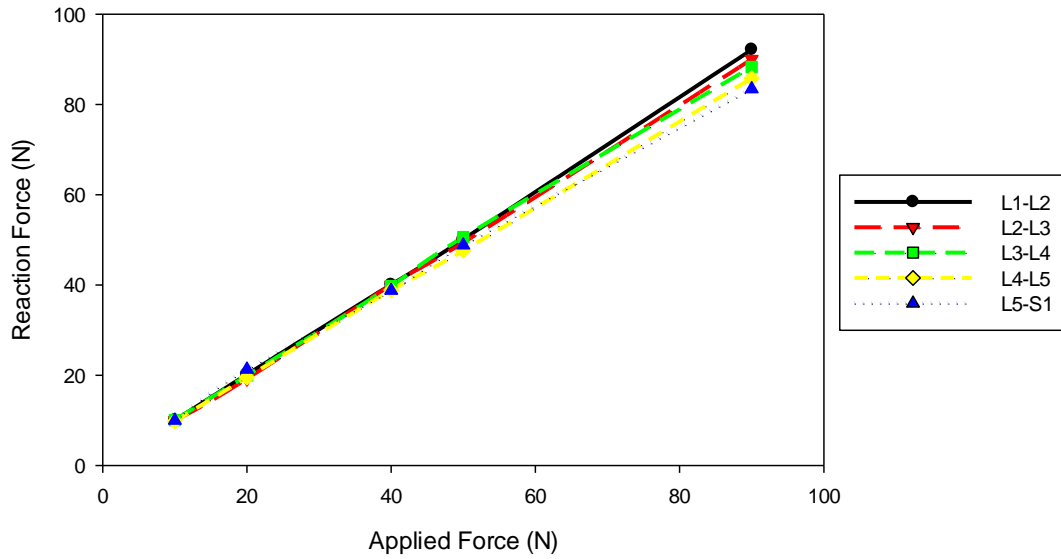


Figure 4.40 - Measured reaction forces (Y-axis) when different loads are applied in Y-axis.

The reaction forces in Y-axis (R_y) present similar behavior in all IVDs. In addition, the R_y values behave linearly, with a proportional increase as the applied load values are higher.

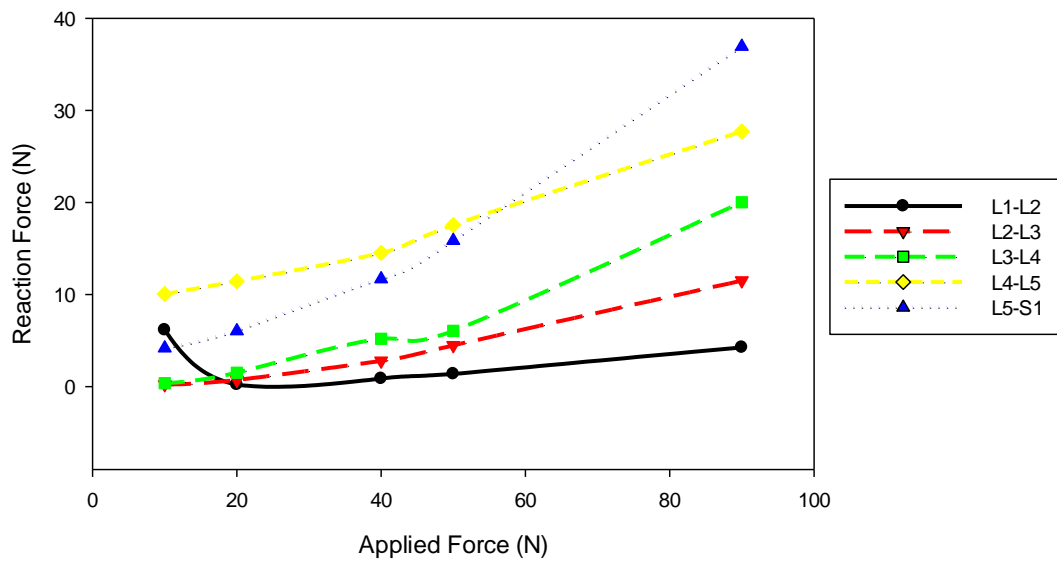


Figure 4.41 - Measured reaction forces (Z-axis) when different loads are applied in Y-axis.

In general, it can be noticed that the two lowest lumbar levels (L4-L5 and L5-S1) present the highest R_z values. In addition, when the maximum value of lateral bend-promoting force is applied (90 N), the R_z values increase as one moves downwards along the lumbar spine.

In this case, Rx values are inexistent when forces in the Y-axis are applied.

Figures 4.42 and 4.43 display respectively, the measured X and Z reactions when different compressive forces are applied at the top of L1.

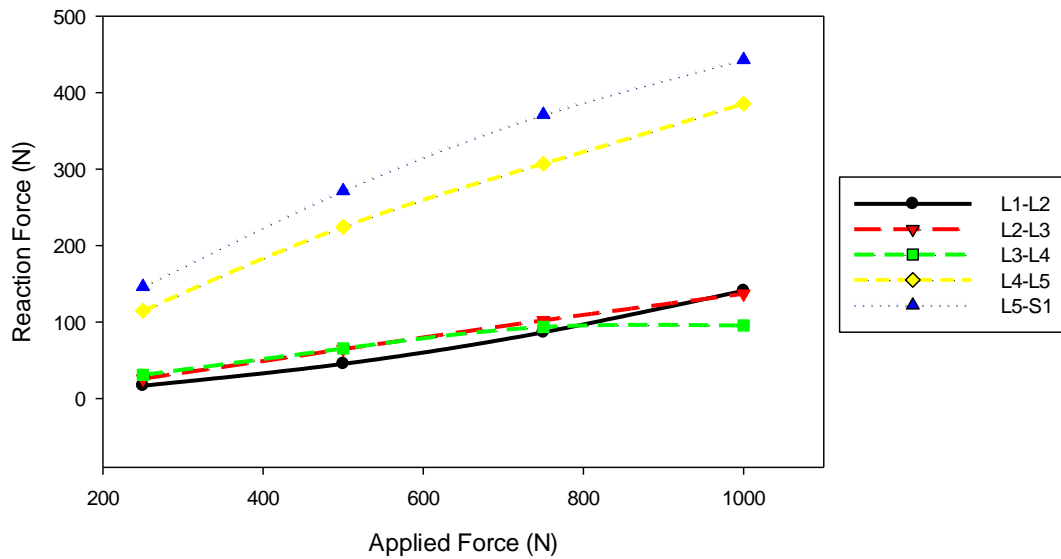


Figure 4.42 - Measured reaction forces (X-axis) when different loads are applied in Z-axis.

Similarly to the Rz results during flexion-promoting forces, it can be observed that both L4-L5 and L5-S1 reveal significantly higher Rz values than the other IVDs during the different load application.

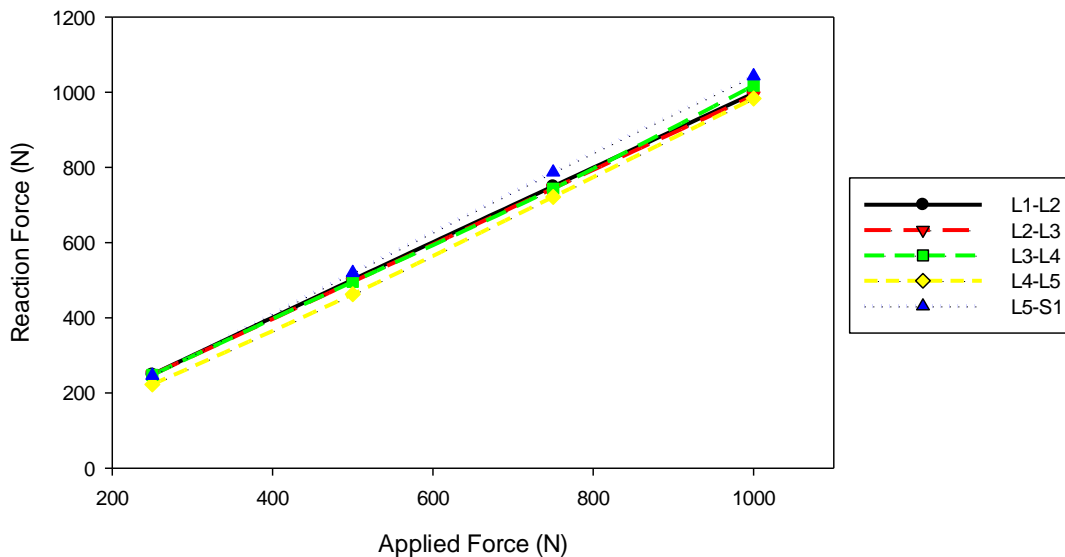


Figure 4.43 - Measured reaction forces (Z-axis) when different loads are applied in Z-axis.

The Rz values present a very similar behavior at all lumbar levels. However, for the maximum compressive force applied, the L5-S1 reveal slightly higher reaction values. The Ry forces are not displayed, as the simulation proved them to be inexistent when compressive forces are applied.

These results indicate that in general, the lower lumbar IVDs are more susceptible to higher mechanical stresses, and therefore, most probably connected with the higher rates of disc injuries are associated to those lumbar levels [16].

CHAPTER 5

Conclusions

The present work aimed to study the biomechanical behavior of the human lumbar IVDs under two different mathematical approaches. Firstly, FEM techniques were applied to study the behavior of the different IVD components under loading and to analyze the effect of the IVD's geometry on its dynamic response to pure moments. Then, by optimizing and simulating a three-dimensional human lumbar multibody system (MBS), the assessment of the whole lumbar spine was performed and the lumbar load distribution was analyzed. On the one hand, FEM approach provided an insight on the general behavior of the IVD and also on the interaction between the different components. On the other hand, the MBS approach provided a macroscopic assessment over the mechanical behavior of the human lumbar spine. Therefore, the primary objectives of this work were achieved.

The first stage of the present work comprised the motivation to perform this study, and provided a general view of the developed spine models, available in the literature, using either of the FEM and/or MBS formulations. Furthermore, the objectives and goals aimed for this study were defined.

Thereafter, an anatomico-physiological description of the human lumbar spine and associated disorders was performed in order to best present the anatomical features that were later mentioned and implemented in the FEM and/or MBS model.

In a third stage, the FEM formulation and the respective IVD model were briefly described, and a geometry sensibility analysis was performed to the IVD. The original IVD model was modified, and ten other geometrically different IVD models were obtained, varying in angle and height. All models were simulated under the same loading conditions to allow for consistent comparison. From this analysis, different mechanical aspects of the IVD's behavior were obtained, such as volume and pressure variations of both AF and NP, quantity and grade of AF's fibers stretching, and range of angular motion. The respective results proved the accurate modeling of the different biomechanical features of the IVD. However, the range of motion during Ex-Fx displayed a non-expected behavior, with the extension range being higher than the flexion one. Nonetheless, the general conclusion obtained was that both

wedge angle and average height variations, influence the behavior of the IVD under loading. Posteriorly, these results were used to optimize a three-dimensional MBS model of the human lumbar spine.

In the fourth stage, the MBS concept was defined, and the previously developed MBS model described. Subsequently, the parameterization of the FEM results was performed and its implementation in the MBS model was executed, allowing the optimization of the IVDs' mechanical behavior according to their angle. Then, the simulation was performed and the results were compared with the ones obtained in the previous stage, proving the correct MBS modeling method. After that, the model was validated by using the experimental data of three different studies found on the literature. Although the model presented some discrepancies in the Ex-Fx movement, both Lfx and AR movements proved to have identical behavior to the experimental results. However, the model's range of motion revealed more flexibility compared to the experimental data.

After validation, different forces were applied the MBS model in order to understand the loading distribution along the lumbar spine. The results indicated that the inferior lumbar IVDs, namely L4-L5 and L5-S1 are more susceptible to mechanical stresses, which is probably related to IVD degeneration and associated disorders.

The major contribution of the present work concerns the understanding of the biomechanical behavior of the intervertebral disc in a healthy condition. Such knowledge may not only serve as a basis to study situations and mechanisms of disc degeneration, but also to consider potential solutions to treat and/or prevent this type of disorders.

Future developments should include the improvement of the IVD's behavior during Ex-Fx movements. The incorporation of the missing elements in the partial MS FEM model (posterior vertebral elements, facet joints and CEPs) might reproduce more accurately the biomechanical response during Ex-Fx. These improvements could also enhance the response of whole lumbar spine during MBS simulation, improving the feedback methodology applied in this work. In addition, the implementation of muscular elements in the MBS model would optimize its behavior, as it would provide a more accurate approach to its physiological functions.

References

- [1] WARD, B. W., SCHILLER, J. S., GOODMAN, R. A., "Multiple Chronic Conditions Among US Adults: A 2012 Update," *Preventing Chronic Disease*, vol. 11, no. 3, pp. 4–7, 2014.
- [2] CENTRE FOR DISEASE CONTROL AND PREVENTION, "Chronic Diseases and Health Promotion", 2014, Available online at: <http://www.cdc.gov/chronicdisease/overview/index.htm>, accessed on September 2014.
- [3] WORLD HEALTH ORGANIZATION, "Chronic rheumatic conditions", Available online at: <http://www.who.int/chp/topics/rheumatic/en/>, accessed on September 2014.
- [4] VAN TULDER, M., KOES, B., BOMBARDIER C., "Low back pain," *Best Practice & Research Clinical Rheumatology*, vol. 16, no. 5, pp. 761–775, 2002.
- [5] ANDERSSON, G. B. J., "Epidemiological features of chronic low-back pain," *Lancet*, vol. 354, pp. 581–585, 1999.
- [6] ANDERSSON, G. B. J., "The epidemiology of spinal disorders," *Frymoyer JW*, pp. 93–141, 1997.
- [7] PRAEMER, A., FURNER, S., RICE, D., "Musculoskeletal Conditions in the United States", 2nd Ed., American Academy of Orthopaedic Surgeons, 1999.
- [8] TAYLOR, V. M., DEYO, R. A., CHERKIN, D. C., KREUTER, W., "No Low-back pain hospitalization: recent United States trends and regional variations," *Spine*, vol. 19, pp. 1207–13, 1994.
- [9] HART, L. G., DEYO, R. A., CHERKIN, D. C., "Physician office visits for low back pain," *Spine*, vol. 20, pp. 11–19, 1995.
- [10] FRANK, A. "Low Back Pain," *BMJ*, vol. 306, pp. 901–909, 1993.
- [11] NACHEMSON, A. L., "Back pain. Causes, diagnosis and treatment," Swedish Council on Technology Assessment - Health Care, 1991.
- [12] KRAMER, J., "Intervertebral Disk Diseases: Causes, Diagnosis, Treatment and Prophylaxis." Thieme, 2008.
- [13] MIZRAHI, J., SILVA, M. J., KEAVENY, T. M., EDWARDS, W. T., HAYES, W. C., "Finite Element Stress Analysis of the Normal and Osteoporotic Lumbar Vertebral Body," *Spine*, vol. 18, no. 14, pp. 2088–2096, 1993.
- [14] SKALLI, W., ROBIN, S., LAVASTE, F., DUBOUSSET, J., "A Biomechanical Analysis of Short Segment Spinal Fixation Using a Three-Dimensional Geometric and Mechanical Model," *Spine*, vol. 18, no. 5, pp. 536–545, 1993.

- [15] VAN DER HORST, M., "Human Head Neck Response in Frontal, Lateral and Rear End Impact Loading", PhD Thesis, Eindhoven University of Technology, Netherlands, 2002.
- [16] WHITE, A., PANJABI, M., "Clinical Biomechanics of the Spine", 2nd Ed., Lippincott, 1990.
- [17] ESAT, V., "Biomechanical modelling of the whole human spine for dynamic analysis", PhD Thesis, Loughborough University, United Kingdom, 2006.
- [18] HAKIM, N. S., KING, A. I., "A Computer Aided Technique for Generation of a 3D Finite Element Model of a Vertebra," *Computers in Biology and Medicine*, vol. 8, pp. 187–196, 1978.
- [19] BELYTSCHKO, T., KULAK, R. F., SCHULTZ, A. B., GALANTE, J. O., "Finite Element Stress Analysis of an Intervertebral Disc," *Journal of Biomechanics*, vol. 7, pp. 277–285, 1974.
- [20] CARTER, D. R., HAYES, W. C., "The Compressive Behaviour of Bone as a Two Phase Porous Structure," *Journal of Bone and Joint Surgery*, vol. 59A, pp. 954–962, 1977.
- [21] KUMARESAN, S., YOGANANDAN, N., PINTAR, F. A., "Finite element modeling approaches of human cervical spine facet joint capsule," *Journal of Biomechanics*, vol. 31, pp. 371–376, 1998.
- [22] GOEL, V. K., KONG, W., HAN, J. S., WEINSTEM, J. N., GILBERTSON, L. G., "A Combined Finite Element and Optimization Investigation of Lumbar Spine Mechanics with and without Muscles", *Spine*, vol. 18, no. 11, pp. 1531–1541, 1993.
- [23] BOZIC, K. J., KEYAK, J. H., SKINNER, H. B., BUEFF, U., BRADFORD, D. S., "Three-Dimensional Finite Element Modeling of Cervical Vertebrae: An Investigation of Burst Fracture Mechanism," *Journal of Spinal Disorders & Techniques*, vol. 7, no. 102–110, 1994.
- [24] DEL PALOMAR, P., CALVO, B., DOBLARÉ, M., "An accurate finite element model of the cervical spine under quasi-static loading," *Journal of Biomechanics*, vol. 41, no. 3, pp. 523–31, 2008.
- [25] FAGAN, M. J., JULIAN, S., SIDDALL, D. J., MOHSEN, M., "Patient-specific spine models. Part 1: Finite element analysis of the lumbar intervertebral disc-a material sensitivity study," *Proceedings of the Institution of Mechanical Engineers: Part H - Journal of Engineering in Medicine*, vol. 216, no. 5, pp. 299–314, 2002.
- [26] KUROWSKI, P., KUBO, A., "The Relationship of Degeneration of the Intervertebral Disc to Mechanical Loading Conditions on Lumbar Vertebrae," *Spine*, vol. 11, pp. 726–731, 1986.
- [27] GOEL, V. K., MONROE, B. T., GILBERTSON, L. G., BRINCKMANN, P., "Interlaminar Shear Stresses and Laminae Separation in a Disc: Finite Element Analysis of the L3-L4 Motion Segment Subjected to Axial Compressive Loads," *Spine*, vol. 20, no. 6, pp. 689–698, 1995.

- [28] GALANTE, J. O., "Tensile Properties of the Human Lumbar Annulus Fibrosus," *Acta Orthopaedica Scandinava Supplements*, vol. 100, 1967.
- [29] IATRIDIS, J. C., KUMAR, S., "Shear Mechanical Properties of Human Lumbar Annulus Fibrosus," *Journal of Orthopaedic Research*, vol. 17, pp. 732–737, 1999.
- [30] KUMARESAN, S., YOGANANDAN, N., PINTAR, F. A., MAIMAN, D. J., "Finite element modeling of the cervical spine: role of intervertebral disc under axial and eccentric loads," *Medical Engineering and Physics*, vol. 21, no. 1999, pp. 689–700, 2000.
- [31] SHIRAZI-ADL, A., SHRIVASTAVA, S. C., AHMED, A. M., "Stress Analysis in the Lumbar Disc Body Unit in Compression," *Spine*, vol. 21, pp. 689–700, 1984.
- [32] LITTLE, J. P., ADAM, C. J., EVANS, J. H., PETTET, G. J., PEARCY, M. J., "Nonlinear finite element analysis of anular lesions in the L4/5 intervertebral disc.," *Journal of Biomechanics*, vol. 40, no. 12, pp. 2744–51, 2007.
- [33] SCHMIDT, H., HEUER, F., SIMON, U., KETTLER, A., ROHLMANN, A., CLAES, L., WILKE, H. J., "Application of a new calibration method for a three-dimensional finite element model of a human lumbar annulus fibrosus.," *Clinical Biomechanics*, vol. 21, no. 4, pp. 337–44, 2006.
- [34] NATARAJAN, R. N., KE, J. H., ANDERSSON, G. B. J., "A Model to Study the Disc Degeneration Process," *Spine*, vol. 19, no. 3, pp. 259–265, 1994.
- [35] WANG, J. L., PARNIANPOUR, M., SHIRAZI-ADL, A., ENGIN, A. E., LI, S., PATWARDHAN, A., "Development and validation of a viscoelastic finite element model of an L2 / L3 motion segment," *Theoretical and Applied Fracture Mechanics*, vol. 28, pp. 81–93, 1997.
- [36] SIMON, B. R., WU, J. S. S., CARLTON, M. W., EVANS, J. H., KAZARIAN, L. E., "Structural Models for Human Spinal Motion Segments Based on a Poroelastic View of the Intervertebral Disc," *Journal of Biomechanical Engineering*, vol. 107, pp. 327–335, 1985.
- [37] LAIBLE, J. P., PFLASTER, D. S., KRAG, M. H., SIMON, B. R., HAUGH, L. D., "A Poroelastic Swelling Finite Element with Application to the Intervertebral Disc," *Spine*, vol. 18, no. 5, pp. 659–670, 1993.
- [38] SIMON, B. R., LAIBLE, J. P., PFLASTER, D. S., YUAN, Y., KRAG, M. H., "A Poroelastic Finite Element Formulation Including Transport and Swelling in Soft Tissues Structures," *Journal of Biomechanical Engineering*, vol. 118, pp. 1–9, 1996.
- [39] FERGUSON, S. J., ITO, K., NOLTE, L. P., "Fluid flow and convective transport of solutes within the intervertebral disc," *Journal of Biomechanics*, vol. 37, no. 2, pp. 213–221, 2004.
- [40] NATARAJAN, R. N., WILLIAMS, J. R., LAVENDER, S. A., ANDERSSON, G. B. J., "Poro-elastic finite element model to predict the failure progression in a lumbar disc due to cyclic loading," *Computers & Structures*, vol. 85, no. 11–14, pp. 1142–1151, 2007.

- [41] SCHROEDER, Y., SIVAN, S., WILSON, W., MERKHER, Y., HUYGHE, J. M., MAROUDAS, A., BAAIJENS, F. P. T., "Are Disc Pressure, Stress, and Osmolarity Affected by Intra- and Extradiscal Fluid Exchange?," Wiley Interscience, October, pp. 1317–1324, 2007.
- [42] STRANGE, D. G. T., FISHER, S. T., BOUGHTON, P. C., KISHEN, T. J., DIWAN, A. D., "Restoration of compressive loading properties of lumbar discs with a nucleus implant-a finite element analysis study.," Spine, vol. 10, no. 7, pp. 602–9, 2010.
- [43] HUANG, J., YAN, H., JIAN, F., WANG, X., LI, H., "Numerical analysis of the influence of nucleus pulposus removal on the biomechanical behavior of a lumbar motion segment.," Comput. Methods Biomech. Biomed. Engin., no. June, pp. 1–9, Jun. 2014.
- [44] CASTRO, A. "Development of a biomimetic finite element model of the intervertebral disc diseases and regeneration", PhD Thesis, University of Minho, Portugal, 2013.
- [45] CASTRO, A., WILSON, W., HUYGHE, J. M., ITO, K., ALVES, J. L., "Intervertebral disc creep behavior assessment through an open source finite element solver.," Journal of Biomechanics, vol. 47, no. 1, pp. 297–301, 2014.
- [46] LATHAM, F., "A Study in Body Ballistics: Seat Ejection," Proceedings of the Royal Society B: Biological Sciences, vol. 147, no. 926, pp. 121–139, 1957.
- [47] ORNE, D., LIU, Y., "A mathematical model of spinal response to impact," Journal of Biomechanics, vol. 4, no. 1, pp. 49–71, 1970.
- [48] MERRILL, T., "Three-Dimensional Lumped Parameter Impact Analysis of a Head/Neck System", University of California, United States of America, 1981.
- [49] MERRILL, T., GOLDSMITH, W., DENG, Y., "Three-Dimensional Response of a Lumped Parameter Head-Neck Model due to impact and Impulsive Loading," Journal of Biomechanics, vol. 17, no. 2, pp. 81–95, 1984.
- [50] DENG, Y., GOLDSMITH, W., "Response of a human head/neck/upper-torso replica to dynamic loading -I. Physical Model," Journal of Biomechanics, vol. 20, no. 5, pp. 471–486, 1987.
- [51] BROMAN, H., POPE, M., HANSSON, T., SPINE, I., CITY, I., "A mathematical model of the impact the seated subject," Medical Engineering & Physics, vol. 18, no. 5, pp. 410–419, 1996.
- [52] STOKES, I., GARDNER-MORSE, M., "Quantitative anatomy of the lumbar musculature," Journal of Biomechanics, vol. 32, pp. 311–316, 1999.
- [53] DE JAGER, M., "Mathematical Head-Neck Models for Acceleration Impacts", PhD Thesis, Eindhoven University of Technology, Netherlands, 2000.

- [54] WATERS, T., LI, F., HUSTON, R., KITTUSAMY, N., "Biomechanical modeling of spinal loading due to jarring and jolting for heavy equipment operators", Proceedings of XVth Triennial Congress of the International Ergonomics Association and 7th Joint Conference of Ergonomics Society of Korea/Japan Ergonomics Society, pp. 4-7, 2003.
- [55] ISHIKAWA, Y., SHIMADA, Y., IWAMI, T., KAMADA, K., MATSUNAGA, T., MISAWA, A., AIZAWA, T., ITOI, E., "Model simulation for restoration of trunk in complete paraplegia by functional electrical stimulation", Proceedings of IFESS05 Conference, pp. 2-4, 2005.
- [56] FERREIRA, A., "Multibody Model of the Cervical Spine and Head for the Simulation of Traumatic and Degenerative Disorders", MSc Thesis, Instituto Superior Técnico, Portugal, 2008.
- [57] JUCHEM, S., GRUBER, K., "MBS Model for the Estimation of Forces and Torques in the Human Lumbar Spine", Proceedings of World Congress on Medical Physics and Biomedical Engineering, pp. 2234-2237, 2009.
- [58] MONTEIRO, N., "Analysis of the intervertebral discs adjacent to interbody fusion using a multibody and finite element co-simulation", MSc Thesis, Instituto Superior Técnico, Portugal, 2009.
- [59] CHRISTOPHY, M., "A Detailed Open-Source Musculoskeletal Model of the Human Lumbar Spine", MSc Thesis, University of California, United States of America, 2010.
- [60] ABOUHOSSEIN, A., WEISSE, B., FERGUSON, S. J., "A multibody modelling approach to determine load sharing between passive elements of the lumbar spine," Computer Methods in Biomechanics and Biomedical Engineering, vol. 14, no. 6, pp. 527–37, 2011.
- [61] GALIBAROV, P., DENDORFER, S., TORHOLM, S., "On Modelling Spine Curvature Dependent on Muscular and External Forces in Multibody Dynamic System," International Society of Biomechanics, 2011.
- [62] HAN, K. S., ZANDER, T., TAYLOR, W. R., ROHLMANN, A., "An enhanced and validated generic thoraco-lumbar spine model for prediction of muscle forces", Medical Engineering & Physics, vol. 34, no. 6, pp. 709–16, 2012.
- [63] HUYNH, K. T., GIBSON, I., JAGDISH, B. N., LU, W. F., "Development and validation of a discretised multi-body spine model in LifeMOD for biodynamic behaviour simulation.," Computer Methods in Biomechanics and Biomedical Engineering, vol. 18, no. 2, pp. 175–84, 2015.
- [64] SEELEY, R., STEPHENS, T., TATE, P., "Anatomy and Physiology", 6th Ed., McGraw-Hill, 2003.
- [65] NETTER, F. H., "Atlas of Human Anatomy", 2nd Ed., Elsevier, 1997.

- [66] NAEGEL, B., "Using mathematical morphology for the anatomical labeling of vertebrae from 3D CT-scan images.," *Computerized Medical Imaging and Graphics*, vol. 31, no. 3, pp. 141–56, 2007.
- [67] BOGDUK, N., "Clinical Anatomy of the Lumbar Spine and Sacrum", 4th Ed., Elsevier, 2005.
- [68] RAJ, P., "Intervertebral Disc: Anatomy-Physiology- Pathophysiology-Treatment," *Pain Practice*, vol. 8, no. 1, pp. 18–44, 2008.
- [69] JENSEN, G. M. "Biomechanics of the Lumbar Intervertebral Disk: A Review," *Physical Therapy Journal*, pp. 765–773, 1980.
- [70] MOON, S. M., YODER, J. H., WRIGHT, A. C., SMITH, L. J., VRESILOVIC, E. J., ELLIOTT, D. M., "Evaluation of intervertebral disc cartilaginous endplate structure using magnetic resonance imaging.," *European Spine Journal*, vol. 22, no. 8, pp. 1820–8, 2013.
- [71] POSTACCHINI, F., "Management of Herniation of the Lumbar Disc," *Journal of Bone and Joint Surgery*, vol. 81-B, pp. 567–576, 1999.
- [72] HERMAN, I. P., "Physics of the Human Body", 1st Ed., Springer, 2007.
- [73] MORAMARCO, V., DEL PALOMAR, P., PAPPALETTERE, C., DOBLARÉ, M., "An accurate validation of a computational model of a human lumbosacral segment.," *J. Biomech.*, vol. 43, no. 2, pp. 334–42, Jan. 2010.
- [74] FALLER, A., SCHUENKE, M., "The Human Body - An Introduction to Structure and Function" Thieme, 2004.
- [75] KAPANDJI, A. I., "The Physiology of the Joints", 6th Ed., Churchill Livingstone, 2008.
- [76] BOOS, N., AEBI, M., "Spinal Disorders - Fundamentals of Diagnosis and Treatment", 1st Ed., Springer, 2008.
- [77] WILLS, B., MOHR, A., "Current Status of Imaging of the Intervertebral Disc," *Seminars in Spine Surgery*, vol. 19, no. 2, pp. 58–64, 2007.
- [78] AN, H., BODEN, S. D., KANG, J., SANDHU, H. S., ABDU, W., WEINSTEIN, J., "Summary statement: emerging techniques for treatment of degenerative lumbar disc disease," *Spine*, vol. 28, pp. 24–25, 2003.
- [79] ANDREULA, C. F., SIMONETTI, L., DE SANTIS, F., AGATI, R., RICCI, R., LEONARDI, M., "Minimally Invasive Oxygen-Ozone Therapy for Lumbar Disk Herniation", *American Journal of Neuroradiology*, no. 24, pp. 996–1000, 2003.
- [80] MORAIS, S., "Development of a Biomechanical Spine Model for Dynamic Analysis", MSc Thesis, University of Minho, Portugal, 2011.

- [81] CAVALCANTI, C., CORREIA, H., CASTRO, A., ALVES, J. L., "Constitutive Modelling of the Annulus Fibrosus: Numerical Implementation and Numerical Analysis," IEEE 3rd Portuguese Meeting in Bioengineering, vol. 7, pp. 3–6, 2013.
- [82] ALVES, J. L., YAMAMURA, N., ODA, T., TEODOSIU, C., "Numerical Simulation of Musculo-Skeletal Systems by V-Biomech," Computer Methods in Biomechanics and Biomedical Engineering, 2010.
- [83] SMIT, T. H., "The mechanical significance of the trabecular bone architecture in a human vertebra," Technical University of Hamburg, 1996.
- [84] CORREIA, H., CASTRO, A., CLARO, J. C. P., ALVES, J. L., "Finite Element Simulation of Daily Activities Held by the Intervertebral Disc," 5º Congresso Nacional de Biomecânica, 2013.
- [85] EHLERS, W., KARAJAN, N., MARKERT, B., "An extended biphasic model for charged hydrated tissues with application to the intervertebral disc", Biomechanics and Modeling in Mechanobiology, vol. 8, no. 3, pp. 233–51, 2009.
- [86] NOAILLY, J., PLANELL, J., LACROIX, D., "On the collagen criss-cross angles in the annuli fibrosi of lumbar spine finite element models", Biomechanics and Modeling in Mechanobiology, vol. 10, no. 2, pp. 203–19, 2011.
- [87] MATOS, J., "Development of a 3D multibody system of the human lumbar spine", MSc Thesis, University of Minho, Portugal, 2013.
- [88] YAMAMOTO, I., PANJABI, M., CRISCO, T., OXLAND, T., "Three-Dimensional Movements of the Whole Lumbar Spine and Lumbosacral Joint," 16th Annual Meeting of the International Society for the Study of Lumbar Spine, 1989.
- [89] FLORES, P., CLARO, J. C. P., LANKARANI, H. M., "Kinematics and Dynamics of Multibody Systems with imperfect joints: models and case studies", Springer, 2008.
- [90] NIKRAVESH, P. E., "Planar Multibody Dynamics: Formulation, Programming, and Applications", 1st Ed., CRC Press, 2008.
- [91] SOUSA, S., "Otimização de um modelo multicorpo da coluna lombar humana", MSc Thesis, University of Minho, Portugal, 2014. (Under submission)
- [92] LOURENÇO C., CLARO, J. C. P., "Biomechanical Experimental Data Curation: An Example for Main Lumbar Spine Ligaments Characterization for a MBS Spine Model," New Trends in Mechanism and Machine Science, vol. 24, pp. 435–443, 2014.
- [93] KELLER, T. S., COLLOCA, C. J., "Force-deformation response of the lumbar spine: a sagittal plane model of posteroanterior manipulation and mobilization", Clinical Biomechanics, vol. 17, no. 3 pp. 185–196, 2002.

- [94] GUAN, Y., YOGANANDAN, N., MOORE, J., PINTAR, F., ZHANG, J., MAIMAN, D. J., LAUD, P., "Moment-rotation responses of the human lumbosacral spinal column", *Journal of Biomechanics*, vol. 40, no. 9, pp. 1975–80, 2007.
- [95] PANJABI, M., OXLAND, T., YAMAMOTO, I., CRISCO, J., "Mechanical Behavior of the Human Lumbar and Lumbosacral Spine as shown by Three-Dimensional Load-Displacement Curves", *Journal of Bone and Joint Surgery*, vol. 76, no. 3, pp. 413-24, 1994.

APPENDIX A – Range of motion of the lumbar vertebrae

The table 1 summarizes the published data of the limits and the range of motion of the lumbar vertebrae.

Table 1 - Summary of the limits and range of motion of the lumbar spine (Adapted from [87]).

Reference	Level	Force	Localization	Translation (mm)			Rotation (degree)					
				Coronal	Sagittal	Transverse	Lateral Flexion		Flexion_Extension		Axial rotation	
							Left	Right	Flexion	Extension	Left	Right
(39)	L1-L2	-					5.00	6.00	8	5	1	1
	L2-L3	-					5.00	6.00	10	3	1	1
	L3-L4	-					5.00	6.00	12	1	1	2
	L4-L5	-					3.00	5.00	13	2	1	2
	L5-S1	-					0.00	2.00	9	5	1	0
(70)	L1-L2	-					10.97 (3.85)		14.38 (6.09)		8.05 (3.37)	
	L2-L3	-					14.60 (4.86)		16.72 (6.29)		7.89 (4.35)	
	L3-L4	-					14.32 (4.63)		17.72 (5.12)		6.91 (2.04)	
	L4-L5	-					10.57 (4.57)		16.87 (4.74)		7.55 (5.03)	
	L5-S1	-					7.91 (3.47)		14.33 (6.64)		7.22 (5.02)	
(71)	L2-L3	-			-0.6	0.7 +- 0.4			6.8 +- 2.9		3.2 +- 1.9	
	L3-L4	-			-0.9	1.0 +- 0.9			6.7 +- 2.3		2.8 +- 1.7	
(72)	L2-L3	-			3.15 (max) 0.1 (min)				6 (max) 0 (min)			
	L3-L4	-			3.10 (max) 0.31 (min)				6.68 (max) 1.25 (min)			
	L4-L5	-			2.1 (max)				5.12 (max)			

					0.78 (min)				2 (min)		
	L5-S1	-			0.57 (max)				2.37 (max)		
					0.73 (min)				1.43 (min)		
(54)	L1-L2	10 Nm	L1				5 +- 1.4		8.8 +- 2.4		
	L2-L3	10 Nm	L1				6 +- 1.2		10.8 +- 2.4		
	L3-L4	10 Nm	L1				5.2 +- 1.9		10 +- 3.8		
	L4-L5	10 Nm	L1				4.8 +- 2.9		12.8 +- 4		
	L5-S1	10 Nm	L1				4.4 +- 2.2		14.8 +- 4		
(73)	L1-L2	10 Nm	L1				5.2		10.4		
	L2-L3	10 Nm	L1				5.8		10.8		
	L3-L4	10 Nm	L1				6		12.5		
	L4-L5	10 Nm	L1				5.7		13		
	L5-S1	10 Nm	L1				3		10.2		
(74)	L1-L2	2.25 - 2.85 Nm	L1						-2.1 +- -1.6		
	L2-L3								-0.5 +- -1.8		
	L3-L4									1.2 +- 1.8	
	L4-L5									1.4 +- 2.4	
	L5-S1									1.2 +- 2.7	
	L1-L2		L2							-2.1 +- -1.4	
	L2-L3									-1.4 +- -2.4	
	L3-L4									0 +-1.7	
	L4-L5									0.2 +- 1.9	
	L5-S1									1.2 +- 1.8	
	L1-L2		L3							-0.6+- -1.4	
	L2-L3									-0.9 +- -1.2	
	L3-L4									-2 +- -2	
	L4-L5									-1.7 +- -2	
L5-S1								-1.2 +- -2.6			

	L1-L2							-0.2 +- -0.6		
	L2-L3							-07 +- -1.4		
	L3-L4							-1 +- -1.3		
	L4-L5							-2.3 +- -1.4		
	L5-S1							-1.2 +- -2.4		
	L1-L2							-0.1 +- -2.6		
	L2-L3							-90.1 +- -1.6		
	L3-L4							-0.8 +- -2.5		
	L4-L5							-1.4+- -2.3		
	L5-S1							-3 +- -2.2		
(75)	L1	Rotation Right 50°	-2.7	-10.83	-1.66	4.61	-0.76	-16.53		
	L2		-2.5	-6.25	-1.25	2.88	-0.38	-14.61		
	L3		-2.7	-2.91	-1.25	1.15	-0.19	-11.73		
	L4		-2.5	-0.83	-1.04	-0.38	0	-9.42		
	L5		-2.08	-1.66	-0.83	0	-0.57	-9.23		
	S1		-0.83	-3.75	-0.41	0.1	0	-7.11		
	L1	Rotation Right 30°	-0.41	-4.37	-0.62	3.46	0.38	-9.42		
	L2		-0.83	-2.5	-0.41	2.11	0.57	-8.65		
	L3		-1.04	-0.2	-0.2	0.76	0.57	-6.53		
	L4		-1.25	0.41	-0.1	-0.38	0.65	-4.61		
	L5		-1.04	0.3	0	-0.19	0.19	-4.23		
	S1		-0.62	-1.04	0.1	0	0	-3.26		
	L1	Rotation Left 30°	-5	7.29	-1.25	-3.07	-0.57	8.84		
	L2		-5.2	4.37	-1.04	-1.92	-0.76	7.69		
	L3		-4.58	2.91	-1.04	-0.76	-0.96	6.15		
	L4		-3.75	1.87	-0.83	0	-1.15	5		
	L5		-2.5	1.66	-0.83	-0.57	-1.15	4.23		
	S1		-1.66	2.29	0	-0.38	-0.96	3.07		

	L1	Rotation Left 50°	-6.87	17.08	-2.08	-3.84	-1.15	16.53			
	L2		-7.29	12.5	-2.29	-2.3	-1.15	14.8			
	L3		-6.25	8.95	-2.29	-1.15	-1.92	1.69			
	L4		-5	6.87	-1.87	-0.57	-1.92	10.38			
	L5		-2.91	6.25	-1.66	-1.15	-2.11	9.42			
	S1		-0.41	7.08	-0.2	-0.5	-1.73	8.46			
						Mean	Lower/Upper	Mean	Lower/Upper	Mean	Lower/Upper
(5)	L1-L2	In vitro				4.9	3.8/6.5	10.7	5/13	2.1	0.9/4.5
	L2-L3					7	4.6/9.5	108	8/13	2.6	1.2/4.6
	L3-L4					5.7	4.5/8.1	11.2	6/1	2.6	0.9/4
	L4-L5					5.7	3.2/8.2	14.5	9/20	2.2	0.8/4.7
	L5-S1					5.5	3.9/7.8	17.8	10/24	1.3	0.6/2.1
(5)	L1-L2	in vivo/active				5.5	4/10	7	1/14	1	-1/2
	L2-L3					5.5	2/10	9	2/16	1	-1/2
	L3-L4					5	3/8	10	2/18	1.5	0/4
	L4-L5					2.5	3/6	13	2/20	1.5	0/3
	L5-S1					1	1/6	14	2/27	0.5	-2/2
(5)	L1-L2	in vivo/active				7.9	14.2	13	3/23		
	L2-L3					10.4	16.9	14	10/18		
	L3-L4					12.4	21.2	13	9/17		
	L4-L5					12.4	19.8	16	8/24		
	L5-S1					9.5	17.6	14	4/24		
(5)	L1-L2	in vivo/passive						11.9	8.6/17.9		
	L2-L3							14.5	9.5/19.1		
	L3-L4							15.3	11.9/21		
	L4-L5							18.2	11.6/25.6		
	L5-S1							17	6.3/23.7		

(5)	L1-L2				6	3/8	12	9/16	2	1/3
	L2-L3				6	3/9	14	11/8	2	1/3
	L3-L4				8	5/10	15	12/18	2	1/3
	L4-L5				6	5/7	17	14/2	2	1/3
	L5-S1				3	2/3	20	18/22	5	3/6
(76)	L1				23.4 +- 2.39		33.98 +- 4.91		38.73+-4.29	FE model 10
	L2				20.08 +- 2.55		30.25 +- 3.93		34.17+-4.29	7.25
	L3				16.12 +- 1.38		24.78 +- 6.2		31.70+-4.28	4.75
	L4				9.45 +- 1.33		18.09 +- 6.83		24.25+-5.24	2.75
	L5				4.21 +- 0.63		9.69 +- 4.5		12.66+-4.06	0.87
(77)	L1-L2				6 +- 2	-5 +- 2	-8 +- 5	5 +- 2	1 +- 1	-1 +- 1
	L2-L3				6 +- 3	-5 +- 1	-10 +- 2	3 +- 2	1 +- 1	-1 +- 1
	L3-L4				5 +- 3	-5 +- 3	-12 +- 1	1 +- 1	2 +- 1	-1 +- 1
	L4-L5				2 +- 3	-3 +- 2	-13 +- 4	2 +- 1	2 +- 1	-1 +- 1
(78)	L4-L5			6.1 (right) 6.9 (left)	0.9		14.3		0.6	
	L5-S1			4.5 (right) 4.8 (left)	0		10.2		0.2	
(30)	L1-L2	Range of motion during maximum lateral bending of 25°			4.7		2		0	
	L2-L3				6.25		2.1		2.2	
	L3-L4				6.13		1.3		3.8	
	L4-L5				4.53		1.9		2.8	
	L5-S1				3.39		-1		1	
(79)	1 L1-L2	Lab A			4.45		5.75		2.22	
	2 L1-L2				5.75		7.05		2.4	
	3 L1-L2				6.62		4.37		1.4	
	4 L1-L2				5.12		5.37		2.8	

5 L1-L2				10.75	8.5	3
6 L1-L2				11.25	9	4
L3-L4				8.37	7.62	2.68
1 L1-L2	Lab B			5.37	5.25	2.09
2 L1-L2				6.62	6	2.2
3 L1-L2				6.62	4.25	1.22
4 L1-L2				5.37	5.25	1.5
5 L1-L2				14.75	8.5	3.95
6 L1-L2				1.75	12	3.31
L3-L4				9.5	8.95	2.4
1 L1-L2	Lab C			4.37	3.87	2.95
2 L1-L2				5.95	6.37	3.68
3 L1-L2				6.87	4.5	1.13
4 L1-L2				5.5	5.37	3.3
5 L1-L2				7.5	9.25	2.54
6 L1-L2				11	7.5	4.18
L3-L4				9.25	7.5	3.36
1 L1-L2	Lab D			4.55	6.18	2.81
2 L1-L2				6.37	5.75	3.68
3 L1-L2				5.75	3	3.25
4 L1-L2				5.75	5.25	3
5 L1-L2				11.75	10	2.81
6 L1-L2				14	10.5	4.81
L3-L4				9.2	6.95	3.2